



NANYANG
TECHNOLOGICAL
UNIVERSITY

Photonic Crystal Technology for Next Generation Terahertz System

Submitted by: Liang Cassey Crystania

Matriculation Number: U1620160G

Supervisor: Associate Professor Tan Eng Leong

School of Electrical & Electronic Engineering

A final year project report presented to the Nanyang Technological University
in partial fulfilment of the requirements of the degree of
Bachelor of Engineering

2020

Table of Contents

School of Electrical & Electronic Engineering.....	i
Table of Contents	ii
Abstract	i
Acknowledgements	ii
Acronyms	iii
Symbols	iv
List of Figures	1
List of Tables	4
Chapter 1 Introduction.....	5
1.1 Motivation.....	5
1.2 Objectives and Scope	6
1.3 Organisations	7
Chapter 2 Literature Review.....	8
2.1 Photonic Crystal	8
2.1.1 History of Photonic Crystal.....	8
2.1.2 Origin of Photonic Bandgap.....	9
2.1.3 Defect and Localized Mode	17
2.1.4 Temporal Coupled-Mode Theory.....	22
2.2 Topological Photonic Crystal.....	23
2.2.1 Topology and Physics.....	23
2.2.2 Preliminary Concepts.....	25
2.2.3 Integer Quantum Hall Effect.....	28
2.2.4 Topological Photonic	34
2.2.5 Valley-Hall Topological Photonic Crystal.....	37

2.3 Terahertz Communication	38
2.3.1 The Need of Terahertz	38
2.3.2 Current Advancement in Terahertz Communication.....	39
2.3.3 Integrated Terahertz System Based on Photonic Crystal Technology	42
Chapter 3 Photonic Crystal Design.....	44
3.1 Design of Photonic Crystal Lattice	44
3.1.1 Unit Cell.....	44
3.1.2 Atlas Gap	44
3.1.3 Selection of Dimension.....	45
3.2 Design of Photonic Crystal Waveguide.....	48
3.2.1 1D Linear Defect	48
3.2.2 Hollow Rectangular Waveguide and Adiabatic Tapered Feed	50
3.2.3 Simulation of Waveguide	50
3.3 Design of Photonic Crystal Transmitter	54
3.3.1 Dielectric Resonator Antenna (DRA).....	54
3.3.2 Design of Photonic Crystal with DRA for Free-Space Transmission	55
3.4 Design of Narrow Band Filter Based on Photonic Crystal	59
3.5 Bending on Photonic Crystal	64
3.6 Design of Diplexer Based on Photonic Crystal.....	66
3.7 Effect of Losses in Photonic Crystal Design	75
Chapter 4 Topological Photonic Crystal Design.....	77
4.1 Selection of Topological Photonic Crystal Unit Cell	77
4.1.1 Unit Cell.....	77
4.1.2 Atlas Gap	78
4.1.3 Selection of Dimension.....	80

4.2 Design of Topological Photonic Crystal Waveguide	81
4.2.1 Working Principle	81
4.2.2 Design of Topological Photonic Crystal Waveguide	85
4.3 Design of Resonant Tunneling Diode as Miniaturized Source.....	87
4.3.1 Working Principle	87
4.3.2 Design of Resonant Tunneling Diode.....	89
4.3.3 Integration of RTD with TPC	91
4.4 Demonstration of TPC Robustness Against Defect	92
Chapter 5 Terahertz Communication Experiment	94
5.1 Experimental Setup	94
5.2 Detail of the Experimental Equipment	95
5.2.1 Function Generator	96
5.2.2 Multiplier	96
5.2.3 Hollow Rectangular Waveguide	98
5.2.4 Mixer and Spectrum Analyzer	99
Chapter 6 Conclusions and Future Work	100
6.1 Conclusions.....	100
6.2 Recommendation in Future Work	103
Reflection on Learning Outcome Attainment.....	106
References	108
Appendix A: Derivation of Temporal Coupled Mode Theory	113
Appendix B: Berry Phase	118
Appendix C: Final Optimized Sizing	122

Abstract

The natural progression towards the next generation high-speed wireless communication system is going into the regime of Terahertz spectrum. There is a need to develop a platform that could manipulate Terahertz waves seamlessly and to provide a building block for the next generation wireless communication system that will support a fast and reliable wireless data transfer while providing a compact design for commercialization.

In this project, integrated photonic devices based on photonic crystal structure is designed systematically to enable a fast and reliable wireless data transfer operating in low Terahertz frequency spectrum (300-350 GHz). The design is done on COMSOL Multiphysics and CST Microwave Studio. The designed devices have achieved a wide bandwidth performance ($\sim 10\text{GHz}$) that will enable ultra-fast data transfer rate up to the order of Gbit/s. The topological counterpart has also been designed and is proven to be immune against reflection loss. This will consequently enable a defect-insensitive device robust against manufacturing imperfection and improve the reliability of the device. The integrated photonic devices based on photonic crystal structure will inevitably become the backbone of the future wireless communication system and will pave the way to the novel 6G communication system.

Acknowledgements

First of all, I would like to express my heartfelt gratitude to my project supervisor, Associate Professor Tan Eng Leong, for giving me the opportunity to do this project and for his guidance throughout the whole project. Professor Tan has been willing to accommodate the changes in this project and provide continual support and feedback throughout the project execution. It was a great privilege and honor to do this project under his guidance.

I would also like to express my special thanks of gratitude to the members of Center for Disruptive Photonic Technologies (CDPT). Particularly, I would like to express my gratitude to Associate Professor Ranjan Singh for providing me the opportunity to collaborate and the facilities to do the project. I would also like to express my gratitude to Mr. Kumar Abhishek for his mentorship and constructive feedback for me, despite his busy schedule in doing his final year in PhD.

Special thanks to Dr. Leek Meng Lee for his guidance on the concept of topological insulator that has provided direction for me in studying the topological photonic system.

Last but not least, my earnest gratitude goes to my parents for their unflagging love and support throughout my life. I would also like to express my gratitude for my friends who have made my learning experiences to become fulfilling. I am grateful to have received their love, care and support that strengthen me to keep on moving forward.

The completion of this project would not be made possible without their support. I am forever grateful to have this unforgettable learning opportunities.

*Cassey
May 2020*

Acronyms

1D	One Dimensional
2D	Two Dimensional
3D	Three Dimensional
5G	Fifth Generation
6G	Sixth Generation
DRA	Dielectric Resonator Antenna
DOF	Degree of Freedom
EM	Electromagnetic
FOM	Figure of Merit
GHz	Gigahertz
IQHE	Integer Quantum Hall Effect
PC	Photonic Crystal
RTD	Resonant Tunneling Diode
TE, TM	Transverse Electric, Transverse Magnetic
THz	Terahertz
TPC	Topological Photonic Crystal
VPC	Valley-Hall Photonic Crystal

Symbols

\vec{E}	Electric field intensity
\vec{H}	Magnetic field intensity
ϵ_0, ϵ_r	Free space permittivity, relative permittivity
μ_0, μ_r	Free space permeability, relative permeability
ω_n	Angular frequency for band n^{th}
t	Time
c	Speed of light
\vec{k}	Wave number vector
θ	Angle
$ \psi(t)\rangle$	Arbitrary quantum state in Dirac notation
e	Electron charge
Q	Quality factor
ϕ	Flux
σ	Conductivity
ρ	Resistivity
τ	Lifetime
\hbar	Planck constant
λ	Wavelength
$\overrightarrow{u_{n,\vec{k}}}$	Periodic constant
γ	Berry phase
$\overrightarrow{A_n}(\vec{k})$	Berry connection
$\overrightarrow{\Omega}_n(\vec{k})$	Berry curvature
C_n	Chern number
f	Frequency
r	Radius of air hole
a	Lattice constant
d	Length of triangular hole
S_{11}, S_{21}	Reflection and transmission coefficient in S-parameter

List of Figures

Figure 2. 1 (left) Structure of 1D photonic crystal, (right) corresponding band diagram ($\epsilon_r = 12$ and $\epsilon_r = 13$)[10]	13
Figure 2. 2 (left) Possible electric field distribution across the material, (right) the corresponding energy density[10]	14
Figure 2. 3 Electric field and energy density distribution for 1D PC with large dielectric contrast[10]	15
Figure 2. 4 Example of band structure highlighting the difference between radiation and guided mode.....	18
Figure 2. 5 Point defect in 2D photonic crystal slab[14]	20
Figure 2. 6 Monopole and dipole mode of cavity[10]	20
Figure 2. 7 2D PC slab with linear defect[10]	21
Figure 2. 9 (top) A cup of coffee continuously deformed to a donut[16], (bottom) sphere	23
Figure 2. 10 Divide region to compute the Chern number	27
Figure 2. 11 Diagram of experimental setup for classical Hall effect[23].....	28
Figure 2. 12 (left) Classical Hall effect resistivity curve, (right) Integer Quantum Hall effect resistivity curve	30
Figure 2. 13 State localization in the sample due to random potential[24]	32
Figure 2. 14 Chiral edge state on quantum hall effect[27]	33
Figure 2. 15 Quantum hall edge states robustness against defect.....	34
Figure 2. 16 2D Brillouin zone mapped to a torus[31]	35
Figure 2. 17 Topological phase transition at the interface between mirrors that form a waveguide[33]	36
Figure 2. 18 THz macro-scale applications[39].....	40
Figure 2. 19 THz nano-scale applications[39]	42
Figure 3. 1 Triangular lattice structure [10]	43
Figure 3. 2 Plot of normalized gap vs aspect ratio in triangular photonic crystal .44	
Figure 3. 3 (left) Band diagram plotted along the irreducible Brillouin Zone for triangular lattice with $r=72 \mu\text{m}$ and $a=240 \mu\text{m}$, (right) irreducible Brillouin Zone in triangular lattice[42]	46
Figure 3. 4 PC simulation in CST to check the existence of bandgap	46
Figure 3. 5 PC bandgap for square lattice with $r=72 \mu\text{m}$ and $a=240 \mu\text{m}$	46
Figure 3. 6 PC waveguide structure drawn in CST	47
Figure 3. 7 PC waveguide projected band diagram	48
Figure 3. 8 Electric field profile for $k=1$ at (left) $f=306 \text{ GHz}$ and (right) $f=333 \text{ GHz}$	48
Figure 3. 9 Hollow rectangular waveguide (transparent) and tapered feed structure	49
Figure 3. 10 PC waveguide S_{21} parameter	49
Figure 3. 11 E-field distribution of PC waveguide	50
Figure 3. 12 E-field plot at $f=305\text{GHz}$ outside the bandgap	51
Figure 3. 13 PC waveguide propagation loss	52
Figure 3. 14 PC waveguide S_{21} plot at multiple length	52
Figure 3. 15 PC waveguide group delay	53

Figure 3. 16 (left) PC-DRA structure drawn on CST, (right) PC-DRA parameter.....	54
Figure 3. 17 Temporal coupled mode abstraction for PC-DRA system[45]	54
Figure 3. 18 S_{11} parameter of PC-DRA with matching air hole	55
Figure 3. 19 S_{11} parameter of PC-DRA without matching air hole	55
Figure 3. 20 PC-DRA E-field contour plot.....	56
Figure 3. 21 PC-DRA E-field and H-field cone arrow plot.....	56
Figure 3. 22 PC-DRA E-field iso-lines plot.....	57
Figure 3. 23 PC filter cavity shape.....	58
Figure 3. 24 PC Filter structure designed by interfacing waveguide and cavity ...	58
Figure 3. 25 Eigenfrequency of resonant cavity at, (from left to right) $f=308.54$ GHz, $f=315.02$ GHz, $f=321.54$ GHz, $f=339.54$ GHz.....	59
Figure 3. 26 PC filter S-parameter plot.....	59
Figure 3. 27 Electric field profile at, (top) $f= 325$ GHz where field not passed and (bottom) $f= 336.3$ GHz where field are passed due to allowed resonant frequency in the cavity	60
Figure 3. 28 PC filter S_{21} plot for the theoretical and simulated value	61
Figure 3. 29 PC bending structure	63
Figure 3. 30 (left) PC bending E-field, (right) close up of E-field for bending with and without capsule-shaped defect	64
Figure 3. 31 PC bending S_{21} plot for TIR and no TIR structure	64
Figure 3. 32 Illustration of PC directional coupler[53].....	65
Figure 3. 33 Even and odd mode in parallel waveguide.....	66
Figure 3. 34 (left) Projected band diagram for PC directional coupler with one row, (right) field distribution for $k=0.9$ and $f=308.8$ GHz and $f=335.07$ GHz	67
Figure 3. 35 (left) Projected band diagram for PC directional coupler with two rows and, (right) three rows	68
Figure 3. 36 PC directional coupler (left) coupling length, (right) bandwidth	68
Figure 3. 37 PC directional coupler (left) operating frequency and (right) bandwidth plot varied with radius.....	69
Figure 3. 38 PC directional coupler operating bandwidth with varying defect width	70
Figure 3. 39 PC directional coupler projected band diagram for $r=0.23a$ and $w=0.91$	70
Figure 3. 40 PC diplexer design[53]	71
Figure 3. 41 PC diplexer and waveguide projected band diagram	72
Figure 3. 42 PC diplexer full structure.....	72
Figure 3. 43 PC diplexer E-field at $f=317.1$ GHz showing a cross transmission ..	72
Figure 3. 44 PC diplexer S-parameter.....	73
Figure 3. 45 PC waveguide S_{21} plotted at various resistivity values	74
Figure 4. 1 Valley-hall Topological Photonic Crystal unit cell [57]	77
Figure 4. 2 Combined atlas gap of VPC plotted in MATLAB	78
Figure 4. 3 Bandgap opening in topological photonic crystal when the inversion symmetry is broken.....	79
Figure 4. 4 Electric field profile plot for (left) $f=310.54$ GHz and (right) $f=340.54$ GHz when $\Delta d=0.3$	79

Figure 4. 5 Electric field profile plot for (left) f=310.54 GHz and (right) f=340.54 GHz when $\Delta d=-0.3$	80
Figure 4. 6 Band Diagram for VPC at $d_1=0.35a$ and $d_2=0.65a$	81
Figure 4. 7 VPC unit cell (left) type A, (right) type B	81
Figure 4. 8 (left) Projected Band Diagram type AB, (right) field distribution at f=339 GHz, k=0.8	82
Figure 4. 9 (left) Projected Band Diagram type BA, (right) field distribution at f=308 GHz, k=-0.75	82
Figure 4. 10 Close look at VPC interface	84
Figure 4. 11 VPC waveguide structure	85
Figure 4. 12 VPC S_{21} plot	85
Figure 4. 13 VPC electric field plot	86
Figure 4. 14 TPC propagation loss	86
Figure 4. 15 RTD internal structure [66]	88
Figure 4. 16 (left) RTD DC I-V characteristics[66], (right) band structure of electron energy[67]	88
Figure 4. 17 (left) RTD design cross section with top view, (right) RTD design side view[66]	89
Figure 4. 18 RTD Structure drawn in CST, (left) 3D View, (right) cross section with top view	90
Figure 4. 19 S_{11} parameter of RTD	90
Figure 4. 20 RTD field distribution at f=331.35 GHz, (left) 3D view, (right) cross section side view	91
Figure 4. 21 RTD VPC Structure	91
Figure 4. 22 RTD VPC S_{11} parameter	92
Figure 4. 23 RTD VPC E-field distribution	92
Figure 4. 24 VPC Bended Waveguide E-field	93
Figure 4. 25 VPC bending loss at 1.5 cm	93
Figure 5. 1 Experimental setup	94
Figure 5. 2 Photograph of the real experimental setup taken from [44]	95
Figure 5. 3 Detailed block diagram	96
Figure 5. 4 8-20 GHz VDi Synthesizer	96
Figure 5. 5 Typical configuration of WR9.0SGX	97
Figure 5. 6 WR2.8 Frequency multiplier	97
Figure 5. 7 Frequency multiplier of WR9.0SGX	98
Figure 5. 8 WR-3 Waveguide	98
Figure 5. 9 VDi SAX	99

List of Tables

Table 1 Final Optimized Sizing of PC Design	121
Table 2 Final Optimized Sizing of TPC Design	122
Table 3 Table of material property	123

Chapter 1 Introduction

1.1 Motivation

The fifth-generation (5G) communication system has opened a lot of new possibilities in technological advancement. However, it has been expected that the 5G communication system might reach its bottleneck by the year of 2030[1]. The ongoing industry 4.0 revolution that requires fast, huge and reliable data transfer cannot be continuously supported by the 5G communication system. The performance limitation of 5G and the need to facilitate the revolutionary technologies in industry 4.0 drive the need to develop the future sixth-generation (6G) communication system, which can be made possible with the development of integrated Terahertz system.

The integrated Terahertz system will enable fast and huge data transfer by providing high-frequency carrier and consequently wide bandwidth. Being located between the microwave and optical frequency spectrum, Terahertz technology was mainly developed on metallic platform or optical platform. Despite of being compact, the metallic platform—however—mainly suffer due to high loss of metal at high frequency. The propagation loss has a typical value of 10 dB/cm, which will limit the device's performance. On the other hand, optical platform has a low loss performance but it has a bulky and complex structure.

It has been found that the photonic crystal based on silicon material would make an excellent platform to support the integrated Terahertz system, owing to its minimum loss in Terahertz operating frequency, compact design, low cost and compatibility with current fabrication technology. However, there is a lack of systematic and detailed study on the subject, despite of its powerful application. Therefore, this project aims to study and design integrated photonic crystal devices that can work at high operating frequency in the range of 300-350 GHz.

One main drawback of photonic crystal is that it has significant reflection loss upon bending. This can limit the performance of the device, especially considering the defect introduced during the manufacturing phase. Topological photonic crystal—also known as photonic topological insulator—will resolve the issue of

significant reflection loss by ensuring a one-directional transmission of signal that is guaranteed by its topological nature, consequently enabling a design of device that is robust against manufacturing defect.

The topological photonic crystal is a novel application of Nobel Prize of Physics in 2016 that is applied to photonic crystal. This project also aims to study and design integrated topological photonic crystal devices that can work in the desired Terahertz operating frequency.

Lastly, a visibility study on the experimental measurement will also be presented to show a possible real application of the designed device.

1.2 Objectives and Scope

The main objective of this project is to design integrated photonic crystal devices that can work in low Terahertz operating frequency (300-350 GHz) to enable a fast and reliable data transfer. To be more specific, the objectives of this project are listed as follow:

1. To design the building block of integrated photonic crystal device, which includes important components such as waveguide, transmitter, filter and active sources.
2. To prove the robustness of topological photonic crystal as compared to the ordinary photonic crystal in terms of propagation loss and robustness against reflection loss.
3. To do a visibility study on the possible experimental scheme of communication system based on the design device.

Furthermore, the scope of this project is limited to:

1. Theoretical and simulations study of the designed device. Experimental verification is excluded due to the delay of the instalment of experimental equipment.
2. Designing the device to operate in the lower Terahertz spectrum (300-350 GHz).
3. Solving the Eigenproblem using commercial software. Numerical simulation is excluded.
4. Discussing the intuitive understanding and interpretation as well as

verification of the theory of topological photonic crystal. Formal mathematical analysis will be excluded due to the advanced pre-requisite knowledge that is needed to study the system.

1.3 Organisations

This thesis is organized as follow.

Chapter 1 contains the introduction to the project, which includes the motivation in carrying out this project, the main objectives and the scope of this project.

Chapter 2 is dedicated to extensively provide a background study on the theoretical framework in designing the device and also to provide some historical and pedagogical discussion on the previous work. This literature review is divided into three parts, each dedicated for the three-main pillar of this report, namely the photonic crystal, the topological photonic crystal and the Terahertz communication system.

Chapter 3 presents the design of photonic crystal devices. The discussion is generally structured to explain the working principle of the device, the design process, the result and the implication on the Terahertz communication system. Detailed explanation on the step-by-step design process and the rationality of selecting particular dimension size are presented throughout this whole chapter and subsequent chapters as well.

Chapter 4 presents the design of topological photonic crystal devices. This chapter is structured similarly to Chapter 3.

Chapter 5 presents the visibility study on possible experimental scheme of Terahertz communication system. The experimental equipment that has been purchased to verify the design experimentally is also presented.

Lastly, Chapter 6 concludes and gives recommendation for possible future work.

Chapter 2 Literature Review

2.1 Photonic Crystal

2.1.1 History of Photonic Crystal

The ability to manipulate electrical properties of material has become a key point in enabling the technological revolution. However, utilizing electron as the main carrier of information transmission have some few drawbacks. One such example is the significant increase in the consumed power density of miniaturized devices[2].

In the recent decades, the research has been focused more towards manipulating the optical properties of material, where the photon now acts as the primary carrier of information. This has few advantages, such as faster device's speed due to larger photon's speed, wider bandwidth in dielectric material as opposed to metallic material, and reduced power dissipation due to the less interacting photon[3].

Photonic crystal was originally found by Eli Yablonovitch[4] and John Sajeev [5] back in 1987. The name *photonic crystal* arises from the fact that the periodic structure of dielectric(*crystal*) is able to manipulate the light (*photonic*) in a certain manner. This is the optical analogue of semiconductor crystal (*periodic arrangement of atom*) that can control the *electron*. By properly designing the geometry and periodicity of the material, light with frequency in a certain range will not be allowed to propagate, creating what is commonly known as *photonic bandgap* (PBG). The photonic bandgap lies at the heart of all photonic crystal devices.

Enormous number of useful devices can be built by controlling the propagation of light. For example, this can be seen from the discovery of fiber-optic cables which revolutionized the telecommunication industry. A robust way of controlling the propagation of light can be achieved by engineering the bandgap of photonic crystal.

The discovery of photonic crystal has been pioneered by the creative work of Lord Rayleigh back in 1917[6], where he demonstrated a multilayer film that acts

as a mirror, commonly known as Bragg mirror. Bragg mirror acts as mirror only for light with certain frequency and can localize particular light mode when defect is introduced in the structure. This 1D multilayer film is the simplest photonic crystal structure.

2.1.2 Origin of Photonic Bandgap

The origin of photonic bandgap can be understood by the following explanation: the plane wave propagating through the periodic material will undergo successive reflections and refractions at each interface. The wave whose frequency are in the photonic bandgap range will be reflected constructively and transmitted destructively such that there is no forward propagation. In other words, this sum of multiple reflection and refraction is what give rise to the bandgap phenomenon in photonic crystal.

A more formal and robust way of analyzing the system is through the analysis of band structures of material which will be presented throughout the report.

2.1.2.1 Mathematical Analysis

In this section, we will derive the central equation. Central equation is the eigenvalue equation whose solutions describe the field distribution. This section aims to show that photonic bandgap is a consequence that results from the interaction between the electromagnetic wave and the periodic arrangement of material.

First, we start from the general Maxwell equation. Faraday and Ampere law state that (assuming free source region):

$$\nabla \times \vec{E} + \mu_0 \frac{\partial \vec{H}}{\partial t} = 0$$

$$\nabla \times \vec{H} - \epsilon_0 \epsilon(\vec{r}) \frac{\partial \vec{E}}{\partial t} = 0$$

We can approximate the solution to be a plane wave and write it in tensor form. This approximation is reasonable as many of the physical waves approximate a plane wave when it is far away from the source.

$$\vec{E} = \overrightarrow{E_0(\vec{r})} e^{-i\omega t}$$

$$\vec{H} = \overrightarrow{H_0(\vec{r})} e^{-i\omega t}$$

We can then insert the equation of plane wave solution into the Maxwell equation. Thereafter, we can eliminate the \vec{E} term and write the differential equation in terms of \vec{H} . We will obtain the following equation governing the H-field.

$$\nabla \times \left(\frac{1}{\epsilon(\vec{r})} \nabla \times \vec{H} \right) = \left(\frac{\omega}{c} \right)^2 \vec{H}$$

where we have defined $c = \frac{1}{\sqrt{\epsilon_0 \mu_0}}$ as the speed of light. We can further define an operator $\hat{\theta}$ as:

$$\hat{\theta} = \nabla \times \left(\frac{1}{\epsilon(\vec{r})} \nabla \times \right)$$

Re-writing the equation governing the H-field using the operator we have just defined, we will have

$$\hat{\theta} \vec{H} = \left(\frac{\omega}{c} \right)^2 \vec{H}$$

The equation above is the eigenvalue problem governing the field mode. The eigenvector \vec{H} corresponds to the field distribution of the harmonic modes whereas the eigenvalue $(\frac{\omega}{c})^2$ is proportional to the squared frequency of the mode. Note that we can also express the equation in term of the electric field. However, it is tougher to solve the eigenvalue problem using E-field. This is because the operator that appears in eigenvalue equation is not a Hermitian operator and thus would need a more complex method to solve[7].

We should simplify the Eigenvalue problem equation. First, the permittivity $\epsilon(\vec{r})$ should be expanded in terms of its Fourier coefficient. We will also work in terms of the inverse of permittivity for convenience.

$$k_r(\vec{r}) = \frac{1}{\epsilon_r(\vec{r})} = \sum \widetilde{k}_r(\vec{G}) e^{i\vec{G}\cdot\vec{r}}$$

$$\widetilde{k}_r(\vec{G}) = \frac{1}{V_{cell}} \iiint d\vec{r}^3 \epsilon(\vec{r}) e^{-i\vec{G}\cdot\vec{r}}$$

where $\widetilde{k}_r(\vec{G})$ is the Fourier coefficient, V_{cell} is the volume of a unit cell used to define the Fourier expansion coefficient and \vec{G} is the reciprocal vector defining the periodicity of the material. Note that we prefer to express the permittivity in terms of its Fourier expansion because material is periodic in nature. Furthermore, we

prefer to work with the inverse of permittivity as this follows from the pedagogical approach used in condensed matter physics that often work in reciprocal space to analyze band diagram of semiconductor crystal. The full expression of equation (6) depends on the geometry of the structure. See example in [7].

The field should be expanded according to Bloch-Floquet theorem. Bloch-Floquet theorem allows us to express the field in terms of a linear superposition of propagating plane wave times a constant that describes the periodicity of the medium. In other words, we can express the field in the following form:

$$\vec{H}_{\vec{k}}(\vec{r}) = \sum_{\vec{G}} h_{\vec{G}} e^{i(\vec{k} + \vec{G}) \cdot \vec{r}}$$

where \vec{k} is called the wave vector of the EM field propagating in the structure.

From Gauss's law for magnetism, we know that the divergence of H is equal to zero. That is to say:

$$\nabla \cdot \vec{H} = 0$$

Substituting the Bloch-Floquet function to the divergence of H will yield the following equation:

$$h_{\vec{G'}} \cdot (\vec{k} + \vec{G'}) = 0$$

where we have used $\vec{G'}$ instead of \vec{G} for indexing purpose. Due to the orthogonality condition, we can define three orthogonal unit vectors $(\hat{e}_1, \hat{e}_2, \hat{e}_3)$ as following:

$$\vec{k} + \vec{G'} = |\vec{k} + \vec{G'}| \hat{e}_3$$

$$h_{\vec{G'}} = h_{1\vec{G'}} \hat{e}_1 + h_{2\vec{G'}} \hat{e}_2 = \sum_{\lambda=1,2} h_{\lambda\vec{G'}} \hat{e}_{\lambda}$$

Substituting the orthogonal expansion to the Bloch-Floquet equation, we have:

$$\vec{H}_{\vec{k}}(\vec{r}) = \sum_{\vec{G'}} \sum_{\lambda=1,2} h_{\lambda\vec{G'}} \hat{e}_{\lambda} e^{i(\vec{k} + \vec{G'}) \cdot \vec{r}}$$

We shall now attempt to substitute the above equation to the left-hand side of the Eigenvalue problem equation. Before we proceed to substitute, we note that:

$$\nabla \times (e^{i(\vec{k} + \vec{G'}) \cdot \vec{r}} \hat{e}_{\lambda}) = i e^{i(\vec{k} + \vec{G'}) \cdot \vec{r}} (\vec{k} + \vec{G'}) \times \hat{e}_{\lambda}$$

The above equation can be proven by expressing the curl in terms of \hat{e}_{λ} and performing some mathematical manipulation. Next, we compute the curl of H:

$$\nabla \times \vec{H}_{\vec{k}}(\vec{r}) = i \sum_{\vec{G}'} \sum_{\lambda} h_{\lambda \vec{G}'} [(\vec{k} + \vec{G}') \times \hat{e}_{\lambda}] e^{i(\vec{k} + \vec{G}') \cdot \vec{r}}$$

Multiplying the above equation with $k_r(\vec{r})$ expansion, we will obtain:

$$k_r(\vec{r}) \nabla \times \vec{H}_{\vec{k}}(\vec{r}) = i \sum_{\vec{G}''} \sum_{\vec{G}'} \sum_{\lambda} h_{\lambda \vec{G}'} \widetilde{k}_r(\vec{G}'') [(\vec{k} + \vec{G}') \times \hat{e}_{\lambda}] e^{i(\vec{k} + \vec{G}') \cdot \vec{r}}$$

Let $\vec{G}'' = \vec{G} - \vec{G}'$. This step can be done because \vec{G}'' is just a dummy variable. Rewriting the above equation,

$$k_r(\vec{r}) \nabla \times \vec{H}_{\vec{k}}(\vec{r}) = i \sum_{\vec{G}} \sum_{\vec{G}'} \sum_{\lambda} h_{\lambda \vec{G}'} \widetilde{k}_r(\vec{G} - \vec{G}') [(\vec{k} + \vec{G}') \times \hat{e}_{\lambda}] e^{i(\vec{k} + \vec{G}') \cdot \vec{r}}$$

Next, we compute the curl of the above equation to obtain the LHS of Eigenvalue problem equation.

$$\begin{aligned} \nabla \times (k_r(\vec{r}) \nabla \times \vec{H}_{\vec{k}}(\vec{r})) &= - \sum_{\vec{G}} \sum_{\vec{G}'} \sum_{\lambda} h_{\lambda \vec{G}'} \widetilde{k}_r(\vec{G} - \vec{G}') [(\vec{k} + \vec{G}') \times (\vec{k} + \vec{G}') \times \hat{e}_{\lambda}] e^{i(\vec{k} + \vec{G}') \cdot \vec{r}} \\ &\quad - \sum_{\vec{G}} \sum_{\vec{G}'} \sum_{\lambda} h_{\lambda \vec{G}'} \widetilde{k}_r(\vec{G} - \vec{G}') [(\vec{k} + \vec{G}') \times (\vec{k} + \vec{G}') \times \hat{e}_{\lambda}] e^{i(\vec{k} + \vec{G}') \cdot \vec{r}} \\ &= \left(\frac{\omega}{c}\right)^2 \mu_r \sum_{\vec{G}'} \sum_{\lambda} h_{\lambda \vec{G}'} \widehat{e}_{\lambda} e^{i(\vec{k} + \vec{G}') \cdot \vec{r}} \end{aligned}$$

Further simplification will result in:

$$- \sum_{\vec{G}'} \sum_{\lambda} h_{\lambda \vec{G}'} \widetilde{k}_r(\vec{G} - \vec{G}') [(\vec{k} + \vec{G}') \times (\vec{k} + \vec{G}') \times \hat{e}_{\lambda}] = \left(\frac{\omega}{c}\right)^2 \mu_r \sum_{\lambda''} h_{\lambda'' \vec{G}} \widehat{e}_{\lambda''}$$

Note that we have slightly modified the dummy notation for convenience. We will take a dot product with $\widehat{e}_{\lambda''}$. After that, we shall use the vector identity $\vec{C} \cdot (\vec{A} \times \vec{B}) = \vec{B} \cdot (\vec{C} \times \vec{A})$ to simplify the equation. We should also note that due to orthogonality,

$$\widehat{e}_{\lambda''} \cdot \widehat{e}_{\lambda'} = \begin{cases} 1 & ; \lambda'' = \lambda' \\ 0 & ; \lambda'' \neq \lambda' \end{cases}$$

Finally, we will obtain the final central equation:

$$\sum_{\vec{G}} \sum_{\lambda} h_{\lambda \vec{G}} \widetilde{k}_r(\vec{G}' - \vec{G}) [(\vec{k} + \vec{G}') \times \widehat{e}_{\lambda}] \cdot [(\vec{k} + \vec{G}') \times \widehat{e}_{\lambda'}] = \left(\frac{\omega}{c}\right)^2 \mu_r h_{\lambda' \vec{G}'}$$

Upon solving the central equation by some numerical method (e.g: plane wave expansion method[8, 9]), we will obtain the set of eigenvalues related to the dispersion curve/band diagram (ω vs k) of the material and the corresponding eigenvectors describing the actual field distributions. The dispersion curve will be

presented in Chapter 3 and 4.

Solving the central equation manually with numerical simulation is beyond the scope of this project. Instead, we will use commercial software such as COMSOL Multiphysics to do the numerical simulation and obtain the dispersion curve. However, there is an important thing that can be concluded from this section: *photonic bandgap is a natural consequence resulted from the interaction between the propagating EM wave and the periodic material.*

We did not make any assumption other than the plane wave approximation and we start the derivation by the simple Maxwell equation describing the interaction between the wave and the medium in general. At the end, we arrive at the conclusion that some waves with particular frequency are not allowed to propagate through the periodic material, giving rise to the photonic bandgap phenomenon. By harnessing this fact, we will be able to build powerful devices that can revolutionize the technological advancement as will be demonstrated in the later chapter.

2.1.2.2 Intuitive Explanation

We have derived the formal mathematical analysis for understanding the origin of photonic bandgap in sect. 2.1.2.1. Now, the physical explanation would be presented for a more intuitive understanding. For simplicity and pedagogical purposes, we will consider the case of 1D photonic crystal. Generalization may be done for 2D photonic crystal using the same intuitive explanation.

Consider the following structure of 1D photonic crystal consisting of an alternating dielectric material with relative permittivity of $\epsilon_r = 12$ and $\epsilon_r = 13$ and its corresponding band diagram.

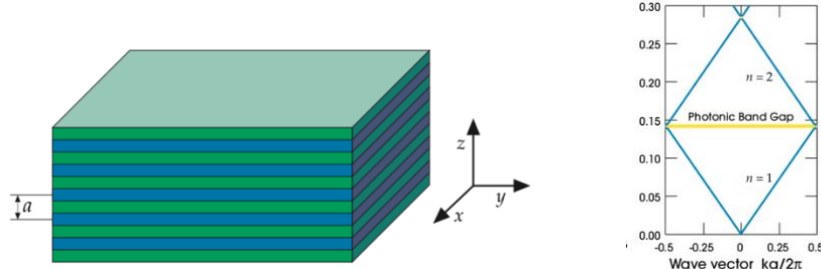


Figure 2. 1 (left) Structure of 1D photonic crystal, (right) corresponding band diagram ($\epsilon_r = 12$ and $\epsilon_r = 13$)[10]

The origin of bandgap can be understood with two important concepts: symmetry that governs the mode profiles and the Variational principle that governs the frequency of the mode. From the band diagram, we can observe that the opening of bandgap happens at the edge of band diagram where $k = \frac{\pi}{a}$. Recalling that $k = \frac{2\pi}{\lambda}$, this corresponds to a wavelength of $\lambda = 2a$.

Due to symmetry, there are two ways to distribute the field mode across the structure. First, the nodes ($\vec{E} = 0$) are centered at low ϵ_r layer as shown in the top left figure. Second, the nodes are centered at high ϵ_r as shown in the bottom left figure. Any other distribution would violate the symmetry with respect to the center of dielectric layer.

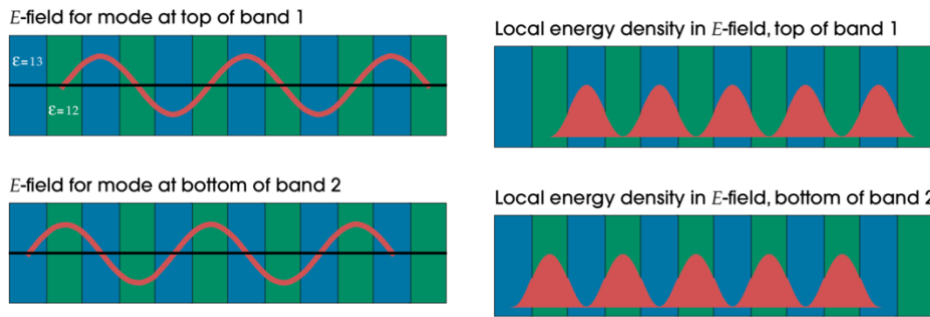


Figure 2. 2 (left) Possible electric field distribution across the material, (right) the corresponding energy density[10]

According to Variational principle, the field distribution is the one that minimize the following functional:

$$U_f(\vec{H}) = \frac{\int d^3\vec{r} |\nabla \times \vec{E}(\vec{r})|^2}{\int d^3\vec{r} \epsilon(\vec{r}) |\vec{E}(\vec{r})|^2}$$

The Variational principle comes from the field of calculus of variation that uses the variation (small change in function or functional) to find its extrema. A more intuitive explanation would be the application of Variational principle in finding the path traversed by light. Fermat's principle[11] states that the path traversed by the light is the path that minimize the time of travel. In this case, the functional is the time of travel as a function of the path traversed by light.

The same analogy can be brought to the electric field distribution in an arbitrary material. The actual electric field distribution will be the one that minimize the functional given in the above equation subjects to the orthogonality condition

$(\int \vec{E}_1 \cdot \vec{E}_2 dx = 0)$ between different harmonic mode. To minimize $U_f(\vec{H})$, the denominator should be maximized and this implies that $|\vec{E}(\vec{r})|^2$ should be large at region where the value of $\epsilon(\vec{r})$ is large.

In other words, the Variational principle states that the low-frequency mode will concentrate their energy (the energy is proportional to $|\vec{E}(\vec{r})|^2$) on high ϵ_r region to minimize the functional whereas the high-frequency mode will *tend* to concentrate their energy on low ϵ_r (not necessarily true in all cases) due to orthogonality condition. This explains the gap between different bands. The only two possible mode distributions require that their respective frequency to be low and high, giving rise to the opening of bandgap.

The heuristic approach based on Variational principle can be extended to describe the structure with large dielectric contrast. In this case, the field energy of both bands is found to be primarily concentrated in region with high ϵ_r , but with different energy concentration, as can be seen on the right figure. This is because the local energy density for 1D PC is expressed with the following equation:

$$E = \frac{1}{2} \int d\vec{r} \epsilon(\vec{r}) |\vec{E}(\vec{r})|^2$$

The energy density in low ϵ_r region is much smaller due to the significantly smaller value of $\epsilon(\vec{r})$ and vice versa. Note also that the mode at respective bands are orthogonal to each other as can be seen from the left figure where an odd field distribution corresponds to an even field distribution on the opposite band. The integral of the dot product of the field over the whole space will evaluate to zero, justifying the orthogonality. In conclusion, the gap now arises due to the difference in the location of field energy.

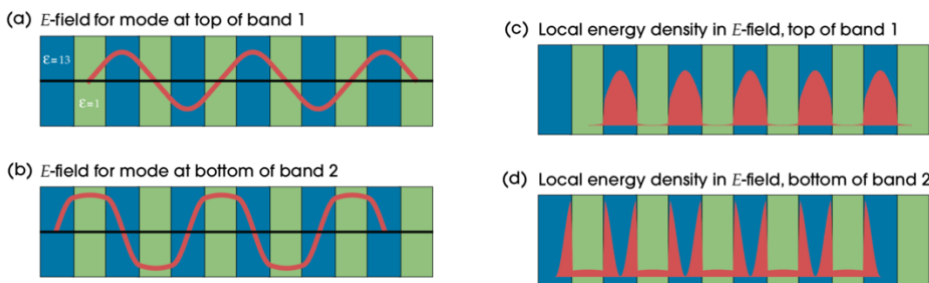


Figure 2.3 Electric field and energy density distribution for 1D PC with large dielectric contrast[10]

Normalized gap-to-midgap ratio is most commonly used to assess the performance of photonic crystal devices. It is defined as the ratio between the frequency gap with respect to the frequency at the middle of the gap and normalized to give a dimensionless quantity. This can be derived using perturbation theory and the final equation will be quoted from [10].

$$\frac{\Delta\omega}{\omega_m} = \frac{\Delta\varepsilon}{\varepsilon} \cdot \frac{\sin \frac{\pi d}{a}}{\pi}$$

$$\omega_m = \frac{n_1 + n_2}{4n_1 n_2} \cdot \frac{2\pi c}{a}$$

The equation above only holds for 1D PC with small permittivity contrast ($\Delta\varepsilon < \varepsilon$) or small thickness ($d \ll a$). However, the equations are useful in giving some intuition when designing the PC. We can observe that the bandgap will get widen when the contrast in permittivity is increased. These equations also handle the scaling properties of material as it is evaluated with respect to the mid-gap frequency.

2.1.2.3 Evanescent Mode

In the preceding sections, we have proven the existence of bandgap inside photonic crystal. Now we will argue that the light with frequency inside the photonic bandgap will decay exponentially as it impinges upon PC surface. The decaying wave is called Evanescent Mode.

To understand the origin of evanescent mode, we consider the bands near the vicinity of the gap. Let $\omega(k)$ be the dispersion relation. We would like to expand $\omega(k)$ near the gap. Without the loss of generality, we choose to expand the dispersion relation near the opening of bandgap at Brillouin zone edge (for 1D) $k_0 = \frac{\pi}{a}$ using Taylor series expansion[12]:

$$\omega(k) = \omega(k_0) + \frac{\omega'(k_0)}{1!}(k - k_0) + \frac{\omega''(k_0)}{2!}(k - k_0)^2 + \frac{\omega'''(k_0)}{3!}(k - k_0)^3 + \dots$$

Time-reversal symmetry requires that[10]:

$$\omega_n(k) = \omega_n(-k)$$

This implies that the expansion of $\omega(k)$ should not contain odd term. Thus, to the lowest order approximation,

$$\Delta\omega = \omega(k) - \omega(k_0) = \frac{\omega''(k_0)}{2!} (k - k_0)^2 = \alpha(k - k_0)^2$$

where $\alpha = \frac{\omega''(k_0)}{2!}$. Further modification will result in:

$$k = k_0 + \sqrt{\frac{\Delta\omega}{\alpha}}$$

For frequency above the gap, $\Delta\omega$ is positive and thus k is a real number. On the contrary, if the frequency is below the gap then $\Delta\omega$ is negative and k is a complex number $k = k_0 + i\kappa$. Substituting it to the expression of magnetic field, we will obtain:

$$\vec{H}_k(\vec{r}) = h(\vec{r}) e^{ik_0 \cdot \vec{r}} e^{-\kappa r}$$

The wave indeed decays exponentially inside the photonic crystal. The mid-gap frequency has the largest attenuation as $\Delta\omega$ is the largest at midgap frequency (recall that $\Delta\omega$ is the difference between frequency in band and frequency in gap). The larger the gap, the larger the attenuation. Thus, it is desirable to have a large bandgap and to operate near the mid-gap frequency.

2.1.3 Defect and Localized Mode

2.1.3.1 Off-axis Localization

There is no bandgap in off-axis propagation due to the absence of material periodicity. Instead, the light is guided by the phenomenon of index-guiding. To begin with, recall that total internal reflection (TIR) is the phenomenon describing that light coming from higher refractive index medium with incident angle greater than the critical angle will be totally reflected. The critical angle is derived from Snell's law[13] by equating the refracted angle to be equal to 180° .

$$\theta_c = \sin^{-1} \frac{n_2}{n_1}$$

where n_1 is the refractive index of incident medium and n_2 is refractive index of opposite medium at the interface. The Snell's law only works well in the approximation of classical ray optics where the wavelength is much smaller than the material structure. In Terahertz photonic crystal application, the wavelength is comparable to the material dimension. Thus, we need to generalize the application

into a broader concept, commonly known as index-guiding phenomenon.

The Snell's law is a consequence of two conservation laws resulted from symmetry, namely the conservation of frequency ω that follow from the linearity and time-invariance properties of Maxwell equations and the conservation of parallel wave vector k_{\parallel} that follow from the continuous translational symmetry along the interface of materials. The parallel wave vector refers to k_{xy} for wave travelling in material with 1D periodicity along z-axis. In our later example of 2D photonic crystal, the parallel wave vector refers to wave vector along the slab thickness. The Snell's law is derived by equating k_{\parallel} in both mediums at the interface. Thus, we can work with the conservation of k_{\parallel} to deal with problem beyond the classical ray-optics regime.

Consider a plane of dielectric material with particular thickness centered about origin. We would like to understand the dispersion relation of parallel wave vector, namely $\omega(k_{\parallel})$. The modes that are not confined in dielectric and radiated to air should resemble a free-space plane wave with frequency:

$$\omega = c|\mathbf{k}| = c\sqrt{k_{\parallel}^2 + k_{\perp}^2}$$

where k_{\perp} is the perpendicular wave vector. For a particular value of k_{\parallel} , there will be modes for every possible frequency ω because k_{\perp} can take any value in the radiation mode. This happens when $\omega > ck_{\parallel}$. Thus, there are continuous states for all frequencies above light line $\omega = ck_{\parallel}$ as illustrated in figure below. The light line is indicated with the red straight line.

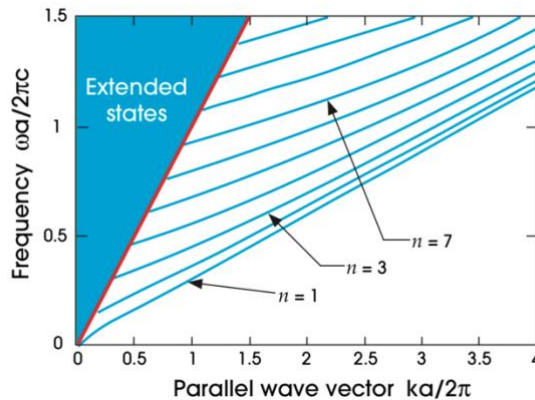


Figure 2.4 Example of band structure highlighting the difference between radiation and guided mode

For the states that lie below the light cone, k_{\perp} will be imaginary. This indicates that the wave will decay exponentially in the air region. Thus, the wave energy will be confined inside dielectric medium, resulted in guided mode of propagation. This is in analogy to Snell's law where the light line indicates the critical angle in Snell's law and the states below the light line indicates the total internal reflection phenomenon.

Furthermore, this is also a consequence of Variational theorem that says that light with low frequency will be confined inside medium with high dielectric constant. In this case, the light with low frequency relative to the light in free-space propagation is confined in the dielectric medium. We call the confined wave as index-guiding mode.

Owing to the discrete value of the allowed frequency in guided mode, we expect to see discrete states for frequency below the light line, as illustrated in figure above. As the wavelength gets smaller, k_{\parallel} gets larger and more of the guided states will be observed. This will approach the limit of Snell's law where there is a continuous angle of TIR $\theta > \theta_c$. In conclusion, the light will be guided by the phenomenon of index-guiding in parallel direction, a phenomenon similar to TIR.

2.1.3.2 On-axis Localization

Along the axis of periodic material arrangement, no light wave in bandgap frequency is allowed to propagate due to the presence of photonic bandgap. However, the evanescent mode may be terminated by the presence of defect. In other words, we can localize the light by perturbing the periodicity of material in terms of defect.

In the 2D photonic crystal slab, which will be used in the design, many options are available. One can change the radii of air-holes in particular location or remove them completely, as illustrated in the following figure. This will create a cavity in the PC slab. If the cavity is sized properly to support a mode inside the band gap, the light will be confined inside and become a defect mode.

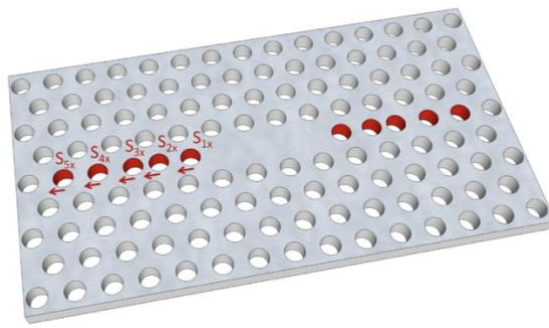


Figure 2. 5 Point defect in 2D photonic crystal slab[14]

The phenomenon of light localization by defect mode is in analogy to the impurities in semiconductor. In the latter case, the atomic impurities will create localized electron states that is inside the semiconductor bandgap. The attractive and repulsive potentials of the impurities will create a state in conduction and valence band respectively, similar to the defect state in photonic crystal. In photonic crystal, we can adjust the geometry or material of the defect to create a suitable defect mode.

The presence of defect will break the symmetry of the PC. However, some symmetries such as rotational, inversion or translational symmetry along particular axis may still be retained. The presence of the symmetry will determine the type of mode that will be supported, such as monopole or dipole, as shown in the figure below. Alternatively, the mode may also be classified as even or odd mode due to the presence of symmetry in propagation plane[15]. The even and odd mode are similar to TE and TM mode. However, they cannot be classified as TE or TM mode entirely due to the lack of translational symmetry along thickness axis.

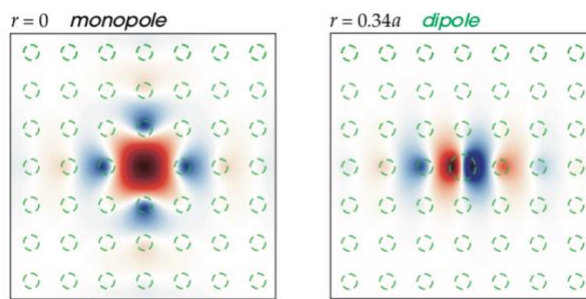


Figure 2. 6 Monopole and dipole mode of cavity[10]

The cavity mode created by the point defect is not truly localized. Instead, the

energy may leak into the surrounding medium, creating a leaky mode or what we commonly call as resonance mode. This is especially true for the practical *finite* PC slab. The decay rate of cavity mode will decrease exponentially with respect to the number of surrounding PC periods. The loss rate may be adjusted accordingly. This will enable us to design many important device application, as will be discussed in Chapter 3.

Alternatively, we may also form a linear defect to guide the light from one point to the other. The linear defect can be formed by modifying a linear row of air-holes, as can be seen in the figure below. Light that is sent along the defect line will be confined due to the presence of photonic bandgap in the surrounding region.

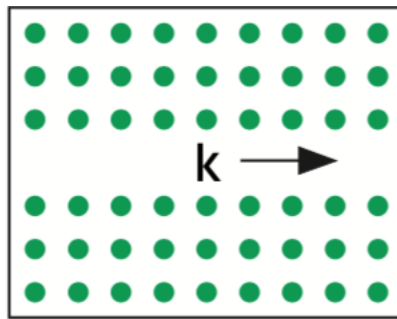


Figure 2. 7 2D PC slab with linear defect[10]

There is still a discrete translational symmetry along the propagation direction. Thus, the corresponding wave vector k is still preserved along that direction. This will result in the guided mode inside the photonic bandgap.

The key difference between point and linear defects lie in the frequency region where the light may be localized. In point defect, any frequency inside the bandgap can be localized. In linear defect, a frequency inside the bandgap alone is not enough to ensure localization. Instead, one need to check if there exists a combination of wave vector along the translational symmetry direction and the frequency that is disallowed in crystal. This approach of analysis is called projecting the band structure. More discussion will be presented in Chapter 3.

The advantage of PC waveguide is that the guiding mechanism is achieved through the confinement of photonic bandgap. This is irrespective of the material along the waveguide channel. Thus, the light may be guided primarily in air, as contrasted to conventional dielectric waveguides that can only confine light in high

dielectric medium by the phenomenon of index-guiding. This is particularly useful when we would like to reduce the interaction (*e.g.*: absorption or non-linearity) between the guided light and the material in the channel.

Lastly, it is important to note that the light cone is an important observation that must be taken into account when analyzing the defect structure. In fact, the presence of radiation modes is what makes the cavity decay to the background. When the cavity is placed near a waveguide, the energy from cavity mode may leak into the waveguide and be coupled over[15]. This will enable many powerful applications, such as the design of diplexer that will be presented in Chapter 3.

2.1.4 Temporal Coupled-Mode Theory

The temporal coupled-mode theory is a theoretical framework that is useful to analyze broad type of devices. The theory provides an abstraction and describes the systems as a combination of isolated components that are coupled in some way. This theory is powerful when designing complex device, such as filter or diplexer that will presented in Chapter 3.

The derivation of the temporal coupled-mode theory is presented in appendix A. In here, we will just quote the result that the transmission spectrum of a system composed of a waveguide-cavity-waveguide can be expressed as follow:

$$T(\omega) = \frac{\frac{1}{4Q^2}}{(\omega - \omega_0)^2 + \frac{1}{4Q^2}}$$

This equation applies well to our design of filter, bending and diplexer that will be presented in Chapter 3. From the derivation that is presented in appendix A, there are three conditions that we should have to achieve a 100% transmission for filter design: (1) symmetric structure ($\tau_1 = \tau_2$), (2) single mode propagation ($A = A(0)e^{-i\omega t}$) and (3) no additional loss mechanism that may come from radiation or absorption loss.

Photonic crystal is an excellent platform to facilitate the third condition. It has low absorption loss because silicon with sufficient resistivity($\sim 10k\Omega/\text{square}$) has small absorption loss in THz operating frequency; it has negligible in-plane radiation loss due to the presence of photonic bandgap. The radiation loss due to

finite thickness that resulted from incomplete bandgap is relatively small if we consider the operating frequency below the light cone.

The derivation of temporal coupled-mode theory also implies that to reduce the reflection loss in the photonic crystal device, one needs to increase the thickness of the slabs. However, there is a trade-off between reducing the effect of reflection loss and pulling down undesired higher order mode as the thickness is increased. Thus, one needs to optimize the thickness according to the design requirement.

2.2 Topological Photonic Crystal

2.2.1 Topology and Physics

Topology is a branch of mathematics that study the properties of a geometric object that are conserved under continuous deformations such as stretching. Two objects are said to be topologically equivalent if they can be deformed into one and another without being cut. For instance, a donut and a cup of coffee are topologically equivalent but a donut and a sphere are topologically not equivalent as there is no way of deforming them from one into another without needing to cut the object.

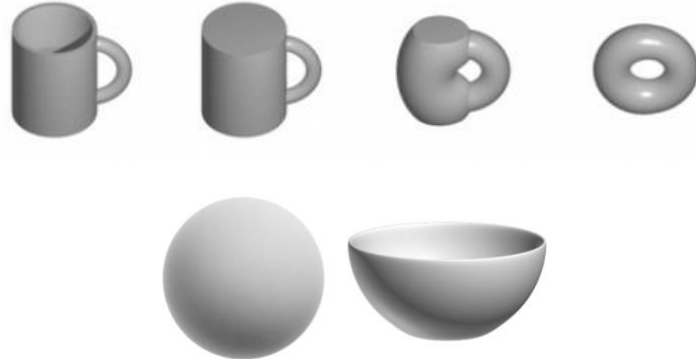


Figure 2. 8 (top) A cup of coffee continuously deformed to a donut[16], (bottom) sphere

Topology provides a tool to analyze the geometric structure. For example, in order to differentiate different object geometrically, one can count the number of hole (genus) that the object possesses. Mathematically, it can be formalized by analyzing the Euler characteristics[17] that provide a framework to describe the object's topology regardless of the structure. The Euler characteristics is a

topological invariant number that will be preserved upon continuous deformation. When the topological invariant number changes under deformation, the object is said to undergo *topological phase transition*.

The branch of topology is important as some of geometric problems does not depend on the exact shape of an object but rather on the general characteristics of the object. It was first studied in the early 1760s. Leonard Euler, as one of the first mathematician who study the topology, demonstrated the hidden concept of topology through his famous problem of The Seven Bridges of Könisberg[18]. Since then, the study of topology had to stay in the realm of mathematics until it found its application in physics through the unexpected discovery of Quantum Hall Effect (QHE) by Von Klitzing[19], who was later awarded for Nobel Prize in Physics (1985). Ever since then, the study of topology in physics has proliferated in many sub-field, including solid-state physics (topological insulators), quantum mechanics (particle physics), optics (topological photonic insulator) and many other more.

All of the fields mentioned previously have one particular thing in common: *each system have a topological invariant number that is discrete and unchanged with small perturbation to the system*, leading to greater stability in the system's properties. This is because the topological invariant number is a global property that belong to the system, as opposed to local property that is determined by individual points.

The appearances of topology in physics can actually be dated far back before the discovery of QHE. In the early 18th century, Gauss's Law and Ampère's law were formulated and they are topological in nature[20]. Each law involves a closed surface or line integral that is preserved under continuous deformation of the surface or curve. In other words, we could say that the integrals representing electric and magnetic fluxes are topologically invariant. Mathematically, we express the electric and magnetic fluxes as below:

$$\phi_E = \oint \vec{E} \cdot d\vec{A} = 4\pi e$$

$$\phi_B = \oint \vec{B} \cdot d\vec{A} = 4\pi g$$

where ϕ is the electric or magnetic flux, E and B are the electric and magnetic

field respectively, A is the surface, e is the electric charge and g is a constant representing the hypothetical magnetic charge. Dirac had proven that the charge e and g must be quantized, implying that the fluxes are also quantized.

2.2.2 Preliminary Concepts

In this section, we will discuss about the important preliminary concepts that are crucial in analyzing the topological material, including the topological photonic system. This includes the discussion on the geometrical (Berry phase and Berry curvature) and topological properties (Chern number) of an eigenstate in momentum space (Brillouin zone).

2.2.2.1 Berry Phase

The concept about Berry Phase lies at the heart of all topological materials. The Berry phase is the geometrical phase that is obtained by making a closed path evolution of an eigenstate. In our case, the eigenstate would be our Bloch state tracing a closed path along the Brillouin zone.

An arbitrary quantum state will acquire a phase after traversing one period of closed path and can be expressed as following (see appendix B):

$$|\psi(T)\rangle = |\psi(0)\rangle e^{-i\gamma_D} e^{i\gamma_G}$$

$$\gamma_D = \frac{1}{\hbar} \int_0^T dt \langle \psi(t) | H | \psi(t) \rangle$$

$$\gamma_G = \int_0^T dt i \langle \phi(t) | \frac{d}{dt} | \phi(t) \rangle$$

where γ_D is the dynamical phase obtained due to the evolution in time and γ_G is the geometrical phase that is obtained due to the geometrical properties of the eigenstate in Hilbert space. This geometrical phase is often overlooked in general literature because the phase is often regarded as a term that only shifts the state by some factor. However, this geometrical phase has been proven to have a significant consequence and is what gives rise to the topological nature of an object.

In fact, the geometrical phase is what gives rise to the precession of a Foucault pendulum[21]. From this simpler example, we can understand that there is a physical manifestation that can be observed from this abstract concept of

geometrical phase. In our case, the physical manifestation would be observed through the topological behaviour of the material (see Chapter 2.2.3 for example).

The physical interpretation of the band diagram is captured partly in the dispersion relation of $\omega_{n,k}(k)$ and partly in the Berry phase that indicates how the eigenstates $u_{n,\vec{k}}(\vec{r})$ change with respect to k . The Berry phase that is acquired over a closed-loop evolution is defined as follow:

$$\gamma = \oint \vec{A}_n(\vec{k}) \cdot d\vec{k}$$

$$\vec{A}_n(\vec{k}) = i \langle u_{n,\vec{k}} | \nabla_{\vec{k}} | u_{n,\vec{k}} \rangle$$

$$\psi_{n,\vec{k}}(\vec{r}) = e^{i\vec{k} \cdot \vec{r}} u_{n,\vec{k}}(\vec{r})$$

where $\vec{A}_n(\vec{k})$ is called the Berry connection as defined above.

2.2.2.2 Berry curvature

The Berry connection defined earlier is not gauge invariant. In fact, if we impose a phase shift $|u_{n,\vec{k}}(\vec{r})\rangle \rightarrow e^{i\chi(\vec{k})}|u_{n,\vec{k}}(\vec{r})\rangle$, the Berry connection will transform as:

$$\vec{A}'_n(\vec{k}) = \vec{A}_n(\vec{k}) - \nabla_{\vec{k}}\chi(\vec{k})$$

Therefore, we define a new parameter called Berry curvature[22] to make a gauge-invariant parameter:

$$\vec{\Omega}_n(\vec{k}) = \nabla_{\vec{k}} \times \vec{A}_n(\vec{k})$$

The Berry curvature become gauge invariant because the curl of a gradient is always zero ($\nabla_{\vec{k}} \times \nabla_{\vec{k}}\chi(\vec{k}) = 0$).

2.2.2.3 Chern Number

Chern number is the parameter that quantifies the topology of the system:

$$C_n = \frac{1}{2\pi} \iint_S d^2k \Omega_n(k_x, k_y)$$

where the integration is carried over the Brillouin zone. If the Berry curvature is continuous across the Brillouin zone, the Chern number will be zero by Stokes theorem[22]. A non-zero Chern number would imply that the Berry curvature can't be defined continuously across the Brillouin zone.

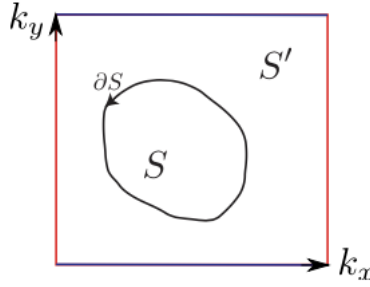


Figure 2.9 Divide region to compute the Chern number

Another important observation is that the Chern number will always be evaluated to an integer. This can be proven with the following explanation. Suppose that we divide the integration domain (k_x, k_y) into two regions, namely S and S' (as shown in the figure above) and suppose we select the Berry connection to be $\vec{A}_n(\vec{k})$ and $\vec{A}'_n(\vec{k})$ respectively.

$$C_n = \frac{1}{2\pi} \iint_S d^2k \Omega_n(k_x, k_y) + \frac{1}{2\pi} \iint_{S'} d^2k \Omega_n(k_x, k_y)$$

Stokes theorem states that:

$$\iint_S (\nabla \times \vec{F}) \cdot \vec{ds} = \oint_C \vec{F} \cdot \vec{dr}$$

Applying to the above equation and recalling the definition for the Berry curvature Ω_n results in:

$$\begin{aligned} C_n &= \frac{1}{2\pi} \oint_{\partial S} \vec{A}_n(\vec{k}) \cdot d\vec{k} - \frac{1}{2\pi} \oint_{\partial S} \vec{A}'_n(\vec{k}) \cdot d\vec{k} \\ C_n &= \frac{1}{2\pi} (\gamma - \gamma') \end{aligned}$$

where we have set $\partial S' = -\partial S$ due to the common contour that they shared. This is possible because the Brillouin zone is shaped as a torus that has a closed surface, thus the two surfaces share a common contour.

Because the Berry phases are computed across the same contour, γ and γ' must be of multiple integer of 2π (geometrical properties computed across the same contour). Therefore, this implies that the Chern number must be an integer.

In conclusion, we have justified that the Chern number, which can only take an integer value, is a suitable candidate for the topological invariant number defining the topology of our photonic system.

2.2.3 Integer Quantum Hall Effect

Before the year of 1980, different states of matter—ranging from gas, crystalline solid, superconductor and magnet—are classified according to the spontaneous symmetry breaking the structure exhibits[23]. For example, typical solid has extra translational degree of freedom along the three orthogonal bases due to symmetry breaking, resulting in the increase of the heat capacity.

However, the discovery of Quantum Hall State had proven the existence of matter's state that does not depend on the geometry or the spontaneous symmetry breaking occurring in the system. Instead, it depends only on the topology of the matter.

The first apparent topological phenomenon was observed in the Integer Quantum Hall Effect (IQHE) phenomenon. Thus, IQHE is discussed briefly for pedagogical and historical view, and also to give an analogy to our topological photonic system. To begin with, we should start with the classical Hall effect and proceed to compare it to the IQHE. The setup of classical Hall effect is shown in the following figure.

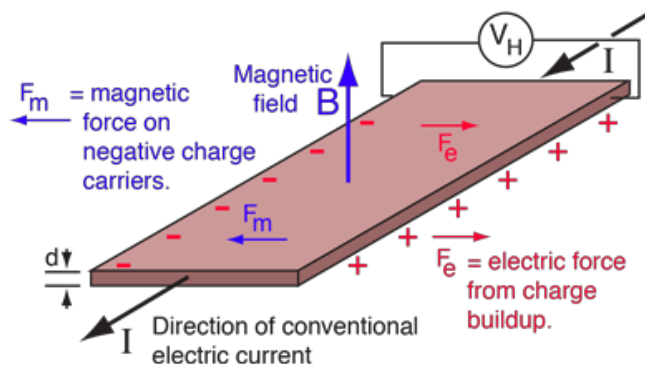


Figure 2. 10 Diagram of experimental setup for classical Hall effect[24]

The classical Hall effect was discovered by Edwin Hall (1879). The setup was to inject electric current on a piece of metal along the longitudinal direction and to turn on magnetic field perpendicular to the metal piece. As the consequence of the charged particles motion in magnetic field, the hall voltage will be built along the transverse direction.

The phenomenon described earlier can be understood by the following explanation. The electron moving in the influence of magnetic field will be

subjected to Lorentz force defined as follow:

$$\vec{F} = q\vec{E} + q\vec{v} \times \vec{B}$$

The first term refers to the electric force that will give rise to the motion along the injected current flow. The second term refers to the magnetic force that occurs in the direction perpendicular to the electron's velocity and the magnetic field. This magnetic force will deflect electron to one end of the metal and produce the hall current that will be probed.

We can assume the electron follow the Drude model (free electron model). The conductivity and resistivity can be derived as following[25]:

$$\sigma = \begin{pmatrix} \sigma_{xx} & \sigma_{xy} \\ -\sigma_{xy} & \sigma_{xx} \end{pmatrix} = \frac{\sigma_{DC}}{1 + \omega_B^2 \tau^2} \begin{pmatrix} 1 & -\omega_B \tau \\ \omega_B \tau & 1 \end{pmatrix}; \sigma_{DC} = \frac{ne^2 \tau}{m}, \omega_B = \frac{eB}{m}$$

$$\rho = \sigma^{-1} = \begin{pmatrix} \rho_{xx} & \rho_{xy} \\ -\rho_{xy} & \rho_{xx} \end{pmatrix} = \frac{1}{\sigma_{DC}} \begin{pmatrix} 1 & \omega_B \tau \\ -\omega_B \tau & 1 \end{pmatrix}$$

where σ is the conductivity and τ is the mean scattering time. Note that the conductivity is not isotropic anymore due to the presence of magnetic field. Thus, the conductivity is a tensor instead of a scalar. We can find the resistivity by taking the inverse of the conductivity. Simplifying the expression further, we can obtain the following relation:

$$\rho_{xx} = \frac{m}{ne^2 \tau}; \rho_{xy} = \frac{B}{ne}$$

The first unique observation that we can observe is that the off-diagonal term ρ_{xy} is independent of the scattering time. *This implies that the quantity captures something fundamental about the material, irrespective of the disorder presence.* This explanation hints something about the robustness of topological material against disorder present.

From the classical point of view, we can predict the resistivity curve to look like the left curve in the following figure.

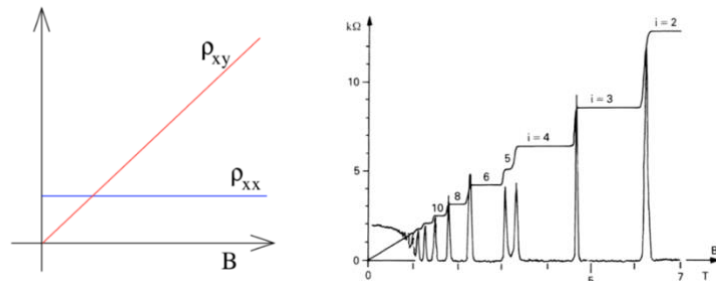


Figure 2. 11 (left) Classical Hall effect resistivity curve, (right) Integer Quantum Hall effect resistivity curve

However, in 1980, von Klitzing performed the Hall effect experiment in quantum regime by confining the electron to move in 2D system. This is done by making the metal bar to be very thin. The experimental result showed a very peculiar result as shown in the right curve. The spiking curve plots the value of ρ_{xx} while the other curve plots the value of ρ_{xy} . The hall resistivity ρ_{xy} sits on plateau for some range of B before stepping to the next plateau. The ρ_{xy} value in these plateau takes the value of:

$$\rho_{xy} = \frac{2\pi\hbar}{e^2} \frac{1}{v}; v \in \mathbb{Z}$$

where v is measured to be integer with highly accurate value, up to the order of 10^9 . The plateau in the curve above is observed despite the presence of the disorder such as dirt. Meanwhile, the ρ_{xx} vanishes when ρ_{xy} sits on plateau. The spike appears only when ρ_{xy} jumps to the next level.

At first glance, $\rho_{xx} = 0$ would make the material appears to be an insulator. However, strange observation is found in the material properties. Using the conductivity tensor definition, we would obtain the following relation:

$$\sigma_{xx} = \frac{\rho_{xx}}{\rho_{xx}^2 + \rho_{xy}^2}$$

If $\rho_{xy} = 0$, we will obtain the usual conductivity and resistivity relation given as $\sigma_{xx} = \rho_{xx}^{-1}$. On the other hand, if $\rho_{xy} \neq 0$, σ_{xx} will be equal to zero when $\rho_{xx} = 0$ that will make the material to become a perfect conductor and insulator at the same time. This sounds paradoxical at a glance, but nature proves that it is possible to have a material behaving like a perfect conductor and insulator concurrently, leading to plethora of application in topological material. One of the most famous example would be graphene[26]. It turns out that this paradoxical nature eventually means that the material is insulating in the bulk but conducting at the edge.

Furthermore, it is to be noted that the applied electric field is in the longitudinal direction whereas the current is flowing in the perpendicular transverse direction. This implies that there is no work in accelerating the charge ($W = \vec{E} \cdot \vec{J}$) and steady

current will flow without any heat dissipation.

The framework that we have considered so far doesn't make any reference to quantum mechanics; *we are working entirely in classical framework with macroscopic object (piece of metal as a whole, as contrasted to single particle), yet the quantity behaves discretely.* This emerging discrete quantity have something to do with the topological properties of the material.

Before discussing the topological aspect of the system, let us try to understand it from the physical perspective. The emergence of plateau can be explained by the filling of Landau levels. Landau levels are energy levels that can be filled by the electron in the presence of magnetic field, expressed with the following relation:

$$E_n = \hbar\omega_B \left(n + \frac{1}{2} \right); n \in \mathbb{N}$$

The landau levels are discrete and has a huge difference between levels and thus requires a big change in energy supplied—or equivalently the magnetic field applied—to allow new conducting electron to fill in the energy state. This energy levels look very different from the energy of free particle in the absence magnetic field. The n^{th} level of Landau energy will only be filled when we supply the following value of magnetic field:

$$B = \frac{n\Phi_0}{v}; \Phi_0 = \frac{2\pi\hbar}{e}$$

This explains why there is a plateau observed in experiment. However, there is a further physical reasoning beyond the filling of Landau levels: *disorder must exist in order for us to observe the plateau.* This might sound odd at the first sight, but the explanation is discussed as follow. First, the presence of disorder will degenerate the energy eigenstates of the Landau level. This comes from the quantum perturbation theory that states that any perturbation that does not preserve symmetry will break degeneracies.

Second, many of the electron states are turned from extended to localized states. Extended state is the state of electron that is spread throughout the whole system space whereas the localized state is the state that is restricted in some region of space. To put it simply, we can think that the effect of disorder is to impose a random potential along the sample. This random potential will have various peaks and troughs denoting the local maximum and minimum potential that will trap the

electron. The illustration is shown in the following figure.

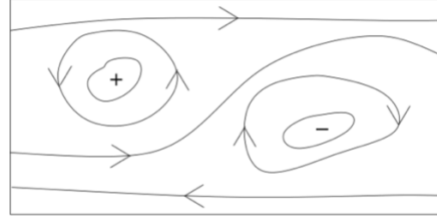


Figure 2. 12 State localization in the sample due to random potential[25]

As we increase the energy, the electron fills in the localized state of degenerated Landau energy level. Thus, there is no increase in conductivity since the newly filled localized states do not conduct current. This leads to the constant conductivity observed over the wide range of magnetic field applied. Note that the disorder presence should be small enough so that the degenerated energy level gap is much smaller than the Landau level gap.

The physical reasoning of the quantization of hall conductivity presented above can be explained and formalized using topology. It has been derived in [25] that the hall conductivity can be expressed as:

$$\sigma_{xy} = -\frac{e^2}{\hbar} C; C = \frac{1}{2\pi} \iint d^2\theta \mathcal{F}_{xy}$$

where C is the first Chern number. The Chern number can be integrated over the spatial torus hall system considered in the reference given[25]. The spatial torus hall system can be thought of as a rectangular 2D metal hall system that are folded to become a torus, similar to the Brillouin zone discussed earlier. The \mathcal{F}_{xy} is the Berry curvature, or often called as the field strength, defined as:

$$\mathcal{F}_{xy} = -i \left[\frac{\partial}{\partial \theta_y} \left\langle \psi_0 \middle| \frac{\partial \psi_0}{\partial \theta_x} \right\rangle - \frac{\partial}{\partial \theta_x} \left\langle \psi_0 \middle| \frac{\partial \psi_0}{\partial \theta_y} \right\rangle \right]$$

where ψ_0 is the ground state of the system and θ_x and θ_y are the spatial torus coordinates.

To summarize, the quantization of hall conductivity comes as a result of the quantization of Chern number. The regime of torus used in the integration of Berry curvature plays an important role in the topology. In analogue, this “spatial torus” is our Brillouin zone of topological photonic crystal. The light’s momentum lies in

the Brillouin zone and we can define a Berry connection over the Brillouin zone that can be associated with a Chern number defining the structure's topology. In this case, the topology arises because the way the phase of the state winds as we move across the Brillouin zone.

Alternatively, the dissipation-less current flow may be understood from the classical microscopic states of the electron. According to Lenz's law[27], the magnetic field applied will cause electron to move in such a way that it will produce a current that will oppose the change of magnetic flux. Looking from the top view, a magnetic field that is pointing towards reader will cause the electron to move in a counter clock-wise direction. Inside the bulk, the neighboring electron current will cancel each other, leaving no net current. On the edge, there is a resulting net current as illustrated in figure below.

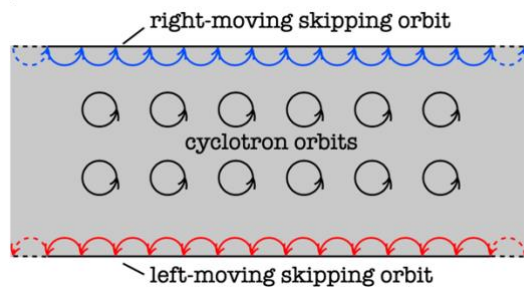


Figure 2. 13 Chiral edge state on quantum hall effect[28]

This gives a robust unidirectional current travelling along the edge (*Chiral*) that result in the robustness against back reflection due to defect or impurity. In a normal conductor, the resistivity that gives rise to heat dissipation is caused by the collision and random scattering between the electron and the impurity. In IQHE, the back reflection is eliminated and the electron will make a round-about turn if there is any defect, as depicted in the figure below. Thus, there is no heat dissipation from the current flow.

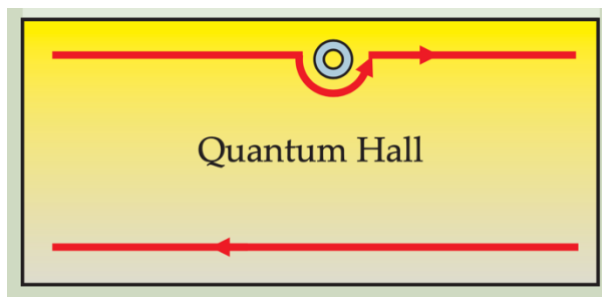


Figure 2. 14 Quantum hall edge states robustness against defect

The present of the edge states can be linked back to topology through the bulk-boundary correspondence principle[29] that state that the number of gapless edge mode along an interface is equal to the difference in the topological invariant number. In this case, the metal bar is a topologically non-trivial insulator whereas the air is perceived as a topologically trivial insulator. Thus, by bulk-boundary correspondence, there exists gapless edge states across the interface. This gapless edge state is robust and will be seen similarly in the design of topological photonic crystal.

Lastly, it is to be stated that the unidirectional nature of electron movement is not captured in the preceding explanation (topological origin from Landau level). Instead, it needs to be analyzed rigorously with the Chern-Simons theory as explained in [25]. The classical explanation above is presented to give an intuitive understanding about the phenomenon.

2.2.4 Topological Photonic

The field of topological photonic has been rapidly growing over the last decade. The field explores the concept of topological phase of matter from solid-state electronic system and extends it to the optical context. It was found that the topology, as a quantity that describe the global behavior of the band diagram, has appeared to be a new DOF of the photonic system. This is analogous to the frequency, wave vector, phase or polarization of the wave that were previously used as the DOF to describe the photonic system.

The discovery of the new DOF opens up many possibilities and revolutionary applications, one of which includes the topological photonic crystal waveguide that ensure a unidirectional transmission of light without back reflection, even around a large imperfection. This is analogous to the dissipation-less current flowing around the edge of quantum hall effect. More on it will be discussed in Chapter 4.

Many of the concept from topological insulator was brought forward to the topological photonic. Graphene is a one of the most popular example of topological insulator. In 2005, Haldane and Raghu[30] proposed a theoretical prediction on the photonic counterpart of the quantum hall effect that is assessed in the system of

photonic crystal. In 2009, Wang[31] *et al.* confirmed the theoretical prediction by providing the design and experimental observation of topology in photonic crystal.

In Chapter 2.2.1, we introduced a topological invariant number of an object defined as the number of holes that the object has. This topological invariant number is computed in the real space where one needs to count the number of holes. In the topological insulator and quantum hall effect, the topological invariant number is described with the Chern number that is computed across the electron's band diagram in momentum space. Similarly, the topological invariant number in topological photonic system is described with its Chern number that is computed across the 2D dispersion band. In particular, the sum of Chern numbers of all dispersion below the band gap determine the topology.

The 2D Brillouin zone (domain of k_x and k_y) can be mapped to a torus due to its periodic boundary condition. This torus plays an important role in determining the topology of the photonic system. To have a more intuitive understanding, we refer to the Gauss-Bonnet theorem that states that the total Gaussian curvatures (\mathcal{K}) over a closed surface in 2D is an integer, characterized by the topological invariant genus (g).

$$\frac{1}{2\pi} \iint \mathcal{K} dA = 2(1 - g)$$

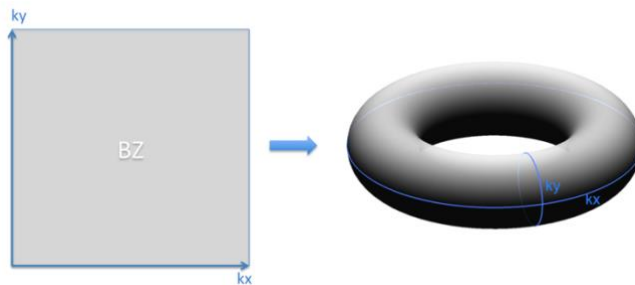


Figure 2. 15 2D Brillouin zone mapped to a torus[32]

Similarly, the Berry curvature defined in the earlier chapter can be integrated over this torus surface of mapped 2D Brillouin zone to give the Chern number. An efficient method to calculate the Chern number has been proposed in [33]. This topological invariant number will not change upon continuous small perturbation, leading to robust unidirectional wave transfer.

An interesting phenomenon takes place when—again—two objects with

different topological invariant number are placed side to side. As shown in the figure below, the ordinary waveguide is composed of two mirrors whose Chern number is equal to zero. Their band diagram can be connected without closing the frequency gap. In contrast, when the mirrors have different Chern number, the frequency gap must be closed and re-opened in order to enable the topological phase transition. This gapless state will enable a robust edge states that is present at all frequencies inside the frequency gap of the bulk mirrors. Generally, the number of gapless edge mode is equal to the difference in the topological invariants of the bulk across the interface, as stated by the bulk-boundary correspondence.

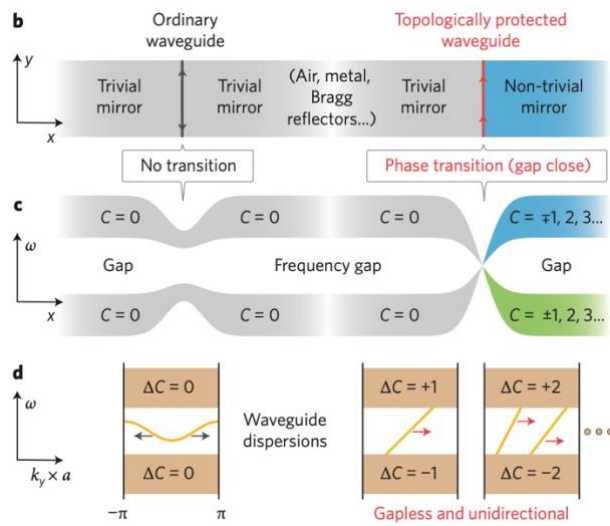


Figure 2.16 Topological phase transition at the interface between mirrors that form a waveguide[34]

The uni-directionality of wave propagation can also be observed from the group velocities of the modes inside the bandgap. The topological waveguide has a positive group velocity (slope of the states) that implies that all the wave can only propagate forward. This will be observed in the design of topological photonic crystal waveguide in Chapter 4.

Furthermore, the symmetry also plays a central part in determining the topology of the photonic system. In fact, the topological photonic system can be classified by the symmetry-protected topological phase that the system possesses, as has been proposed in [35].

2.2.5 Valley-Hall Topological Photonic Crystal

Valley-hall topological photonic crystal (VPC) is the photonic analogue of the quantum valley-hall effect. The term *valley* itself refers to the local minima in the band structure. A new emerging field, called *Valleytronic*, exploits the presence of valley in electronic band structure to obtain a robust transmission of information. This is in analogy to the Spintronic that exploits the spin degree of freedom of electron.

It has been shown by the previous work and will be verified in Chapter 4 that the VPC possesses a topological behavior and supports a uni-directional transmission of light along the interface between two such VPC. This is due to the conservation of valley DOF that will protect the transmission of light from any back scattering. In other words, the two edge states that propagates in opposite direction will be locked to different valley DOF that is conserved as long as the time-reversal symmetry is preserved. The presence of a defect would not be able to back scatter the light because no inter-valley scattering is allowed.

The VPC can be emulated in a hexagonal PC lattice with broken inversion symmetry, that will be designed in Chapter 4. To investigate the topological aspect of the structure, effective Hamiltonian must be analytically derived and be compared to the Hamiltonian on 2D topological material as has been derived in [36] and [37]. In here, we will just quote the result derived in the earlier work.

The VPC possesses a Dirac point in its band diagram because it has a C_6 symmetry like what graphene has. It has been widely known that the graphene has a Dirac cone in its band diagram. The Dirac point is the point where the conduction and valence band meet.

In order to see the topological nature, one must break the inversion symmetry. The breaking of inversion symmetry will reduce the C_6 symmetry to become a C_3 symmetry that will lift the degeneracy of Dirac point. This is because the quantum perturbation theory states that symmetry breaking will lead to the degeneracy lifted up. Once the Dirac point disappear, bandgap will be opened to give an insulating behavior in the bulk.

Furthermore, a non-zero berry curvature has been computed to be localized around the valley that indicates the presence of topological nature. The Berry

curvature and the Chern number that quantifies the topological invariant number of VPC can be expressed by the following equation:

$$C_{K,K'} = \pm \frac{1}{2} sgn(\Delta_P)$$

where Δ_P is the perturbation constant and its value depends on the orientation of the unit cell. sgn is the sign function defined as follow:

$$sgn(\Delta_P) = \begin{cases} 1; \Delta_P > 0 \\ 0; \Delta_P = 0 \\ -1; \Delta_P < 0 \end{cases}$$

In conclusion, the Chern number can only take integer value of $\frac{1}{2}$ and $-\frac{1}{2}$ (0 is a trivial solution) and the value depends on the orientation of unit cell. Furthermore, the Chern number does not change sign when the spatial inversion symmetry is present in the system.

By interfacing the unit cell with opposite value of Chern number, we can have $\Delta C_{K,K'} = \pm 1$ that will give us a topologically protected edge mode by the bulk-boundary correspondence. To summarize, we have a bandgap in the bulk due to the broken inversion symmetry and a robust uni-directional transfer along the interface due to the bulk-boundary correspondence. This will give us a design of waveguide that is robust against back reflection.

The broken inversion symmetry will be seen in our design of Valley-hall topological photonic crystal.

2.3 Terahertz Communication

2.3.1 The Need of Terahertz

Information transmission and processing has become increasingly crucial in this new era of digital world. The growth and development of these technological systems has been accompanied with the increasing need of high data rates.

According to Edholm's law, the wireless data rates had increased at the rate of twice per 18 months in the last four decades. In fact, the current most advanced 5G communication system has reached a data rate up to 10 Gbit/s[38]. It will eventually evolve to reaching the capacity of wired data transfer (100 Gbit/s for Ethernet cable).

Shannon-Hartley theorem states that the channel capacity C , which is the

theoretical upper limit on the data rate that can be transmitted with reasonably low error rate, is related to the bandwidth B and the signal-to-noise ratio (S/N) according to the following relation:

$$C = B \log_2 \left(1 + \frac{S}{N} \right)$$

The equation above implies that in order to increase the data rate (channel capacity), one needs to increase the bandwidth or the signal-to-noise ratio. By increasing the bandwidth, the data rate will be increased linearly, as opposed to the latter case that will only increase the data rate through logarithmic relation. Thus, the former alternative is preferred to increase the data rate. Note also that the bandwidth will usually increase as the carrier frequency is increased due to the constant Q-factor of a device that is preserved even though the carrier frequency changes.

$$Q = \frac{\text{carrier frequency}}{\text{bandwidth}}$$

However, the allocation of carrier frequency and bandwidth in RF spectrum (20 kHz-300 GHz) will become more and more difficult as most of them has been occupied for certain applications[39]. The current bandwidth allocated for 5G communication system was comprised of only less than 10 GHz of bandwidth, a number that is definitely less than enough to support the current technological advancement. Moving to infrared (10-100 THz) spectrum is not a viable option as the data rates are limited to hundreds of Mbit/s owing to incoherent receivers, high ambient light noise, high diffuse reflection loss, and limited power due to eye-safety limits.

The need to look for a higher frequency spectrum propels the development of Terahertz technology. Terahertz technology are envisioned to become the backbone of the next generation 6G communication system. As the fundamental platform of the new wireless communication system, THz technology will enable abundant number of promising applications, including the industry 4.0 revolution that requires high data rates and increasingly interconnected devices.

2.3.2 Current Advancement in Terahertz Communication

THz spectrum, as the frequency spectrum between the microwave and infrared

bands, was not so popular back in the early stage owing to the lack of atmospheric transmission window and lack of THz transmitter and receiver. Nevertheless, the major progress in the last decade has opened up a new path towards practical THz system.

The application of Terahertz communication system can be divided into mainly two categories, namely macro and nano-scale application. The applications include outdoor and indoor application that operates in the speed of Gbit/s to Tbit/s.

Macro-scale application includes those applications whose transmission distance ranges from 1m to 1 km. This includes small cell network where a multiple low-powered antennas (nodes) are installed at the designated location to provide access for wireless communication. The antenna needs to have high directivity to offset the loss incurred in free-space transmission.

Another application that include Tbit/s data rate is the wireless data center that is powered by Terahertz platform. The THz platform, which has wide bandwidth, will handle the high traffic and extend the server extensively, forming a robust THz links. This THz link can be backed with the current system to provide failover mechanism and increase user experience.

Many other applications can still be harnessed in macro-scale application. Most of which includes a point-to-point communication such as THz kiosk downloading that can support instant transfer of huge amount of data, vehicular communication that will advance the autonomous vehicle application, and THz backhaul link as shown in figure below. This point-to-point communication may also be extended for security and medical imaging application as well as space communication.

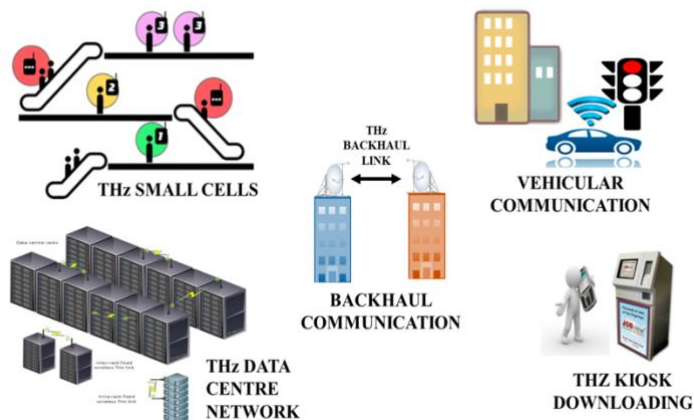


Figure 2. 17 THz macro-scale applications[40]

On the other hand, nano-scale application includes those applications with dimension size up to the order of few centimeters. The nano-THz devices may perform task such as data storage, sensing, actuation or even computation. The nano-devices can even exchange complex information to achieve certain task in a centralized or distributed manner.

The advantage of the nano-scale application is that it can have larger bandwidth and consequently higher data rate that will enable Tbit/s link. This is due to their small size and shorter communication range that reduce the effect of path loss on bandwidth.

Propagation loss is a major challenge in Terahertz communication system that hinders the far-field application of THz communication. In fact, the THz gap was named due to the lack of atmospheric transmission window in THz frequency spectrum and was the reason why THz spectrum was least explored in the early stage of development. However, in the nano-scale application where the maximum distance between transmitter and receiver is only in the order of few cm or less, the propagation loss can almost be neglected, disregarding the near-field diffraction effect.

One particular example of nano-scale application is the on-chip wireless communication network that will be the main focus of this project. The small communication range of on-chip wireless communication network will enable a higher bandwidth and high-density integration due to low area overhead. Thus, we do not need to concern about the path loss in our design at later stage.

Other possible application may be targeted for biomedical application, such as nano-sensor that can detect early disease by utilizing molecular communication, nano-scallop that can swim in biomedical fluid, bio-robot that can be powered by the muscles, on-board drug delivery device, or even plant communication for monitoring purposes.

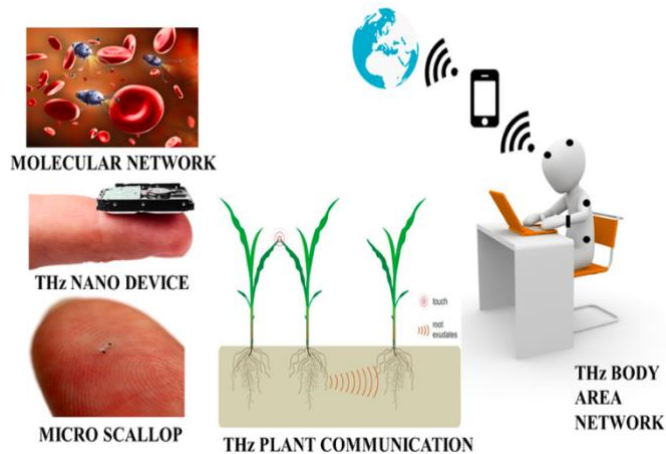


Figure 2. 18 THz nano-scale applications[40]

2.3.3 Integrated Terahertz System Based on Photonic Crystal Technology

As mentioned earlier, THz spectrum has a unique capability that will enable a very fast point-to-point communication. To make it possible, efficiency and compactness of the THz devices are very crucial in determining the success of large-scale integration. Some THz platform rely on microwave devices that utilizes many metallic components. This makes the system becomes less efficient due to the high metallic loss at high frequency. On the other hand, some THz platform was developed based on optical devices that are bulky and complex.

Both the microwave and optical platform for THz system are not capable to support efficient and integrated THz system for commercialization. In the last decade, researchers had found a new suitable platform to develop the THz system that is based on silicon Photonic Crystal devices. The PC has a minimum loss due to the negligible absorption of silicon in THz operating frequency, that makes it stands out as compared to metallic platform. The PC is also a self-supporting device and do not require substrate, consequently enabling a compact design that is preferred as compared to optical devices. Furthermore, the PC fabrication process is very compatible with the current fabrication facilities and will support commercialization. Its suitability to be mass-produced will decrease the overall production cost.

The important building block of the THz circuits based on PC will be presented

in Chapter 3 and 4 (for the topological counterpart). One of the most important building block is the PC waveguide that can transmit signal from one point to the other. Bending can also be designed to route the signal path efficiently.

Diplexer is another important building block that is used for frequency division multiplexing (FDM). FDM is used to divide the total bandwidth into several non-overlapping frequency bands. For example, this can be seen in radio where multiple signals with different frequency are transmitted to the same channel (air) at the same time, but without overlapping. FDM is useful to separate different carriers over the same channel. It can modulate the signal directly inside the PC slabs platform that will improve the functionality and compactness of the design as compared to the system where the modulation is done by the source. This feature is very crucial to reap the full benefits of vast THz spectral band.

In addition, active component is also very crucial and it supports a myriad of functionalities, including THz signal generation, THz signal detection, frequency mixing and external modulation. The active component can be built based on compact epitaxial semiconductors. This active component can be directly integrated with the PC slab. One specific example of the active component is the RTD that will be designed in Chapter 4.

Furthermore, antenna is also very crucial to couple the wave from the waveguide to the free space. The design of antenna will enable intra-chip communication where different chip blocks communicate with each other on the same platform. This will improve the modularity and scalability of the design.

Chapter 3 Photonic Crystal Design

3.1 Design of Photonic Crystal Lattice

3.1.1 Unit Cell

Triangular lattice has been selected and the unit cell is highlighted in red box. This is because the triangular lattice has a wider bandgap as compared to the alternative of square lattice. This will give us a wider bandwidth and better field confinement as has been discussed in sect. 2.1.2.3.

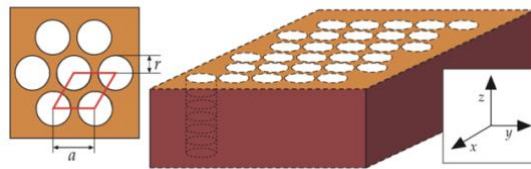


Figure 3. 1 Triangular lattice structure [10]

We have selected the 2D PC slab as our basic structure, instead of opting for the 3D PC structure. The 2D PC will have incomplete bandgap due to the presence of light cone that has radiation mode. However, 2D PC is still preferred because it is more amenable to the current fabrication technology while still offering similar performance as what the 3D PC can do.

3.1.2 Atlas Gap

Atlas gap is the plot of bandgap frequency vs particular dimension of the structure. In here, we choose the aspect ratio r/a as the particular dimension, where r is the radius of the air hole and a is the lattice constant. The atlas gap is plotted in COMSOL and shown in figure below.

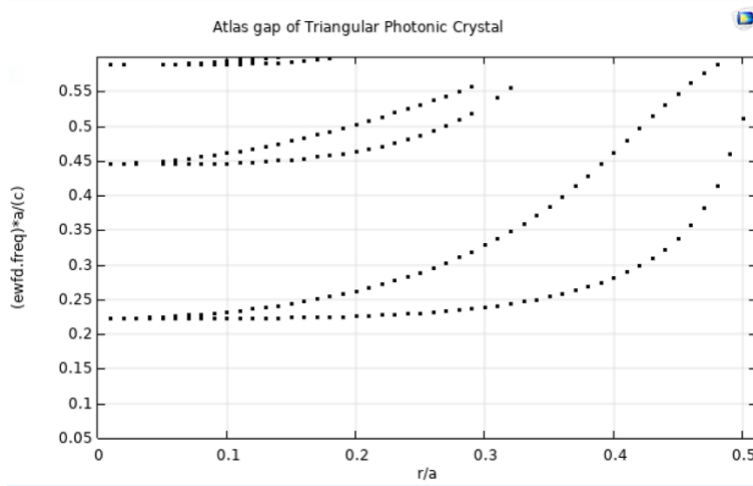


Figure 3. 2 Plot of normalized gap vs aspect ratio in triangular photonic crystal

The y-axis plotted the normalized bandgap frequency $a\Delta f/c$, where c is the speed of light. To design the photonic crystal application in the later stage, we shall consult the atlas gap to locate the bandgap frequency. To account for the finite thickness of PC slab[41], we use an effective relative permittivity of $\epsilon_r = 9$. The actual relative permittivity value is $\epsilon_r = 11.9$.

3.1.3 Selection of Dimension

The lattice constant and aspect ratio are selected to be 240 μm and 0.3 respectively. This sizing will give rise to bandgap frequency in range of 300-400 GHz, which includes our desired operating frequency (300-350 GHz). Furthermore, it is also suitable with the current fabrication process as the aspect ratio is neither too small nor too large for the foundry to fabricate.

The 1D approximation will compute the mid-gap frequency to be around 400 GHz, which gives us the rough idea of where the mid-gap will be located around. Although the value deviates from the 3D practical simulation, this approximation gives a good starting value to design the structure. 3D simulation shall be done in CST to refine this approximation.

The thickness is chosen to be 200 μm . The thickness should not be too small as there will be delocalization in the z-direction due to weak perturbation. At the same

time, the thickness should not be too large because the higher order mode will be sustained inside the dielectric with low energy cost according to Variational principle. Some higher order mode will be pulled down and the bandgap size will be reduced. The optimal thickness has been found to be around half the effective wavelength in medium. The effective wavelength and the wavelength in free space can be computed with the following equation:

$$\lambda_{EFF} = \frac{\lambda_0}{n}; \lambda_0 = c \times f; n = \sqrt{\epsilon_r}$$

Using $f = 300$ GHz and $\epsilon_r = 9$, we find that $\lambda_0 \approx 1$ mm and $\lambda_{EFF} \approx 333$ μ m. Half of the effective wavelength would be 166.5 μ m, close to the selected thickness. Because the fabrication process has been optimized for wafer substrate with thickness 200 μ m, we will use it as our structure's thickness in simulation.

Note that the thickness is not so critical in determining the bandgap. In fact, it is usually selected to optimize other parameters, as long as it has provided sufficient confinement. For instance, it may be chosen accordingly to accommodate longer decay times in resonant cavity that will be presented in the later section. This may be achieved by using slightly larger thickness. In this case, we choose the slab thickness according to the thickness that has been optimized in the current fabrication technology.

The band diagram for the triangular photonic crystal with dimension mentioned above is plotted along the irreducible Brillouin Zone (BZ) as shown in figure below. At K, we have a bandgap from 297.9-409.4 GHz, which is in our desired operating frequency.

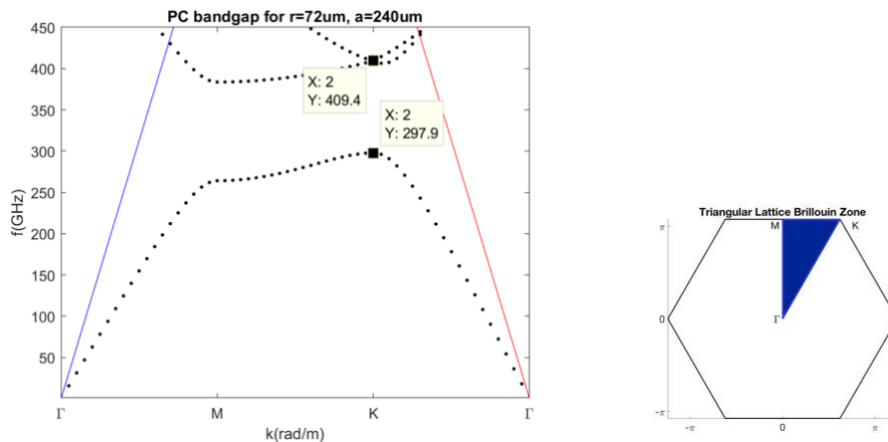


Figure 3. 3 (left) Band diagram plotted along the irreducible Brillouin Zone for triangular lattice with $r=72 \mu\text{m}$ and $a=240 \mu\text{m}$, (right) irreducible Brillouin Zone in triangular lattice[42]

The structure has been simulated in CST to verify the presence of the bandgap. The simulation result is shown in the following figure. The simulation indicates the existence of bandgap in frequency range 300GHz-390GHz, which tallies with the simulation in COMSOL.

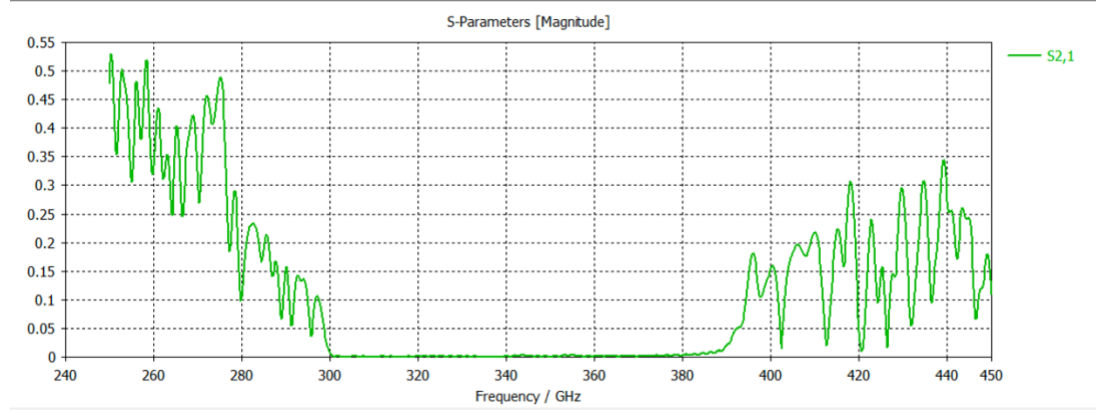


Figure 3. 4 PC simulation in CST to check the existence of bandgap

As a comparison, the band diagram for PC square lattice has also been simulated and presented in the figure below. We can observe that the bandgap size of square lattice is only 20.2GHz, significantly smaller than the triangular lattice.

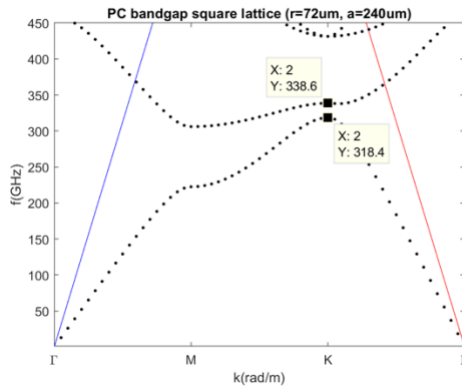


Figure 3. 5 PC bandgap for square lattice with $r=72 \mu\text{m}$ and $a=240 \mu\text{m}$

3.2 Design of Photonic Crystal Waveguide

3.2.1 1D Linear Defect

In order to design a waveguide, we should create a linear defect to guide the light from one point to the other point. As discussed in Chapter 2, one way of creating the linear defect is to remove a row of rod. We choose to remove a row of rod instead of removing multiple rows because it will result in a single mode propagation. Single mode propagation is desired in information transmission for less dispersion.

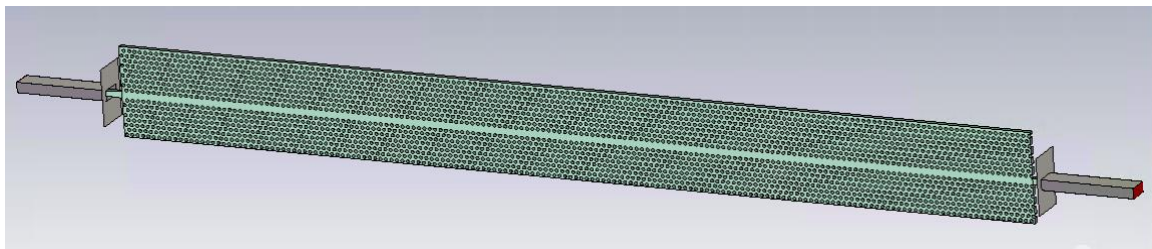


Figure 3. 6 PC waveguide structure drawn in CST

The reason for removing a single row can also be understood by the following discussion. The lowest order mode happens when half of the wavelength spans the width of the defect channel. In other words, the width of the defect channel should be approximately half of our operating wavelength, which is equal to 166.5 μm . This is roughly obtained by removing a single row (diameter of a hole is 144 μm).

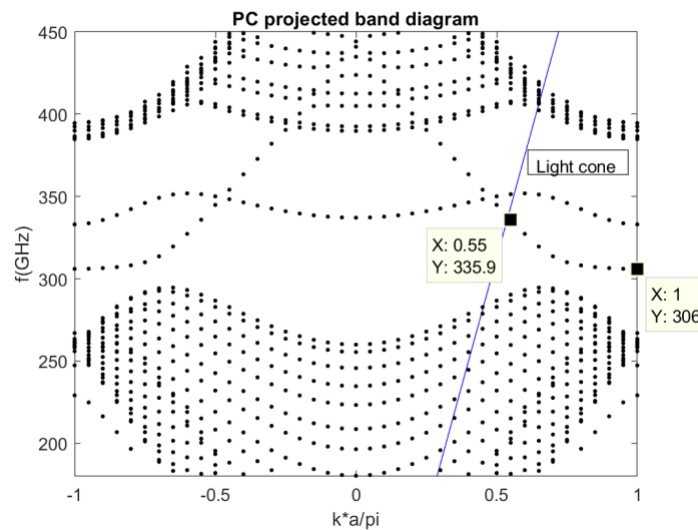


Figure 3. 7 PC waveguide projected band diagram

Figure above shows the projected band diagram of the PC waveguide that is simulated in COMSOL and plotted in MATLAB. By creating a defect along the x-axis, we are now left with two preserved symmetry. One corresponds to the continuous translational symmetry along the x-axis where we have a conserved quantity k_x , the other corresponds to the conserved quantity along z-axis (using 2D PC approximation) where we restrict ourselves for in-plane propagation ($k_z = 0$).

The projected band diagram plots the frequency against the conserved quantity k_x . This is to be differentiated with the band diagram that plots the value of $|\mathbf{k}|$ as its x-axis due to symmetry in x and y direction. We can observe that by creating a linear defect, a guided mode appears inside the bandgap, represented by the two lines inside the original bandgap frequency. The two different lines correspond to different band of guided mode. This can be validated by plotting the electric field distribution for these two distinct lines. For example, we can observe the mode at $k=1$ where we have $f=306$ GHz and $f=333$ GHz as the eigenfrequency solution. Both figures show a guided mode inside the defect line that correspond to different field distribution.

Figure 3. 8 Electric field profile for $k=1$ at (left) $f=306$ GHz and (right) $f=333$ GHz

From the projected band diagram and light cone plot, it can be deduced that the bandwidth ranges from 306 GHz to 336 GHz. Note that the waveguide's bandwidth simulated in this section is different with the bandgap simulated in the previous section. This is because the presence of a guided mode does not solely rely on the existence of bandgap. Instead, there must be a combination of (k_x, ω) that is disallowed in the PC, as has been discussed in Chapter 2.1.3.

3.2.2 Hollow Rectangular Waveguide and Adiabatic Tapered Feed

To feed in the EM wave into the photonic crystal waveguide, we can use a hollow rectangular waveguide and a tapered feed. The rectangular waveguide will receive the input signal from the wave generator and couple it to the tapered feed. The rectangular waveguide that we use is WR-3 waveguide, which is practically capable to transmit microwave signal in the range of 180-345 GHz[43]. The tapered feed will then guide the wave into the photonic crystal waveguide adiabatically due to the tapered structure. The term adiabatic refers to the gradual change in refractive index from air to silicon. This will increase the coupling efficiency by impedance matching as contrasted to rectangular feed that has abrupt termination between silicon and air[44].

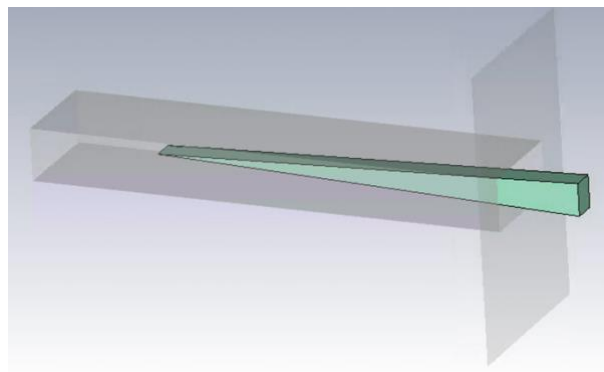


Figure 3. 9 Hollow rectangular waveguide (transparent) and tapered feed structure

3.2.3 Simulation of Waveguide

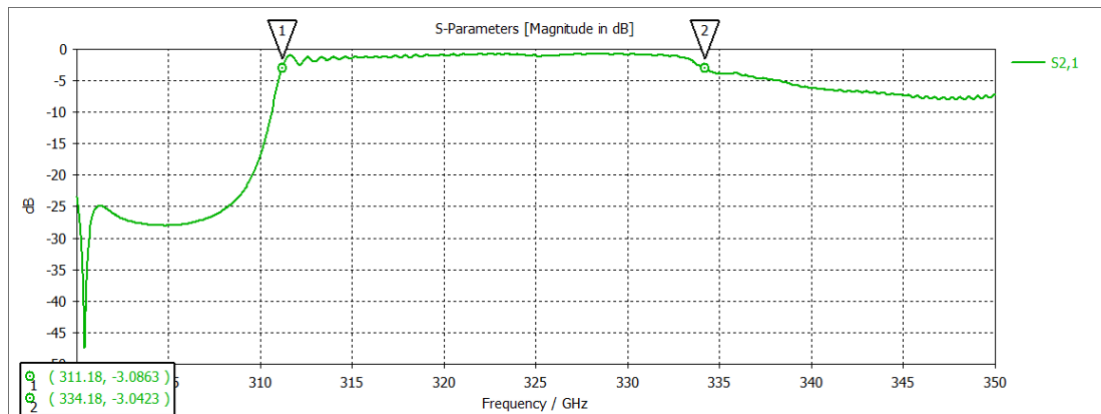


Figure 3. 10 PC waveguide S₂₁ parameter

Figure above shows the transmission coefficient of PC waveguide. The designed photonic crystal waveguide has a bandwidth of 23 GHz. These values are close to the result simulated in COMSOL. Discrepancy may be present due to 2D approximation of 3D structure that we used in COMSOL simulation.

The transmission started to drop at $f=334$ GHz because the higher order mode is present (shown in the projected band diagram and field distribution plot). This higher order mode will couple to the fundamental mode that will result in propagation loss due to the interaction between different modes. Furthermore, the fundamental mode now lies above the light line. Thus, the leak of wave will happen by means of radiation.

The small oscillation in S_{21} plot resulted from the fact that the input signal to the waveguide is a Gaussian-modulated sinusoidal pulse. Because the system is a linear time-invariant system, the output response will follow the input excitation that has oscillatory nature.

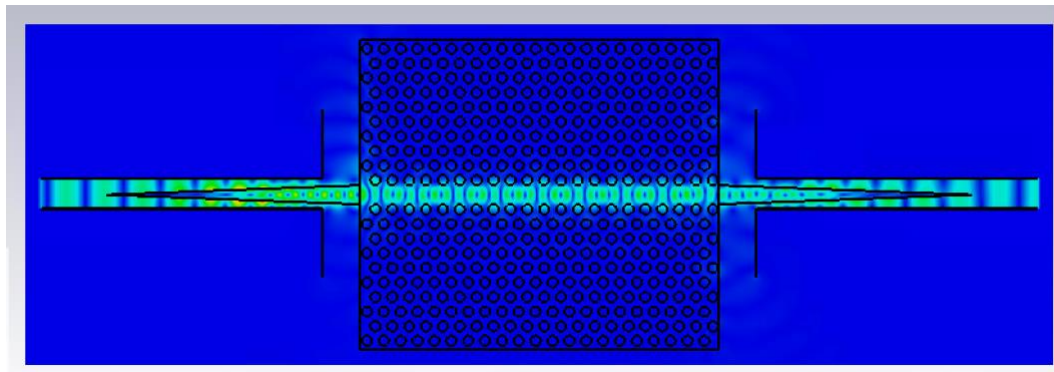


Figure 3. 11 E-field distribution of PC waveguide

The figure above shows the electric field distribution of the guided wave. The waveguide has been sized to have a shorter length for better field visualization. We can see that there is a clear TE-like mode guided along the defect channel. The width of the waveguide is designed in a way that it is enough for the evanescent wave to decay inside the PC before it is coupled to the free-space.

As a comparison, the electric field at $f=305$ GHz has been simulated. It shows that the field will be spread out to photonic crystal's periodic structure when it has frequency outside the bandgap.

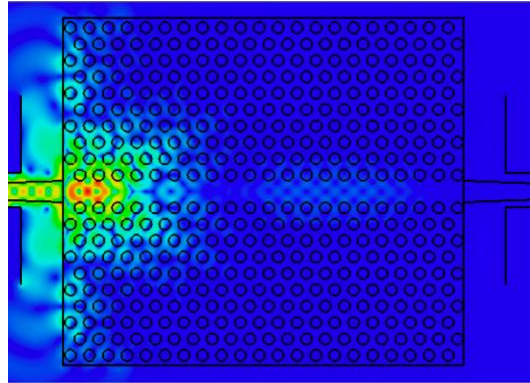


Figure 3. 12 E-field plot at $f=305\text{GHz}$ outside the bandgap

Meanwhile, the length of the waveguide can be tailored according to the requirement. In plotting the S_{21} parameter, the length of the waveguide has been chosen to be 4 cm. This length is sufficient to show the radiation loss that takes place due to finite thickness.

Propagation loss has been computed to better quantify the performance of PC waveguide. The propagation loss measures the loss per distance travelled and is expressed in dB/cm. To simulate the propagation loss, several waveguides with different length must be simulated. The S_{21} parameter will be plotted, indicating the transmittance. The loss will then be computed as follow:

$$L = 2 \times (\alpha - S_{21})$$

where α is the calibrated transmission obtained by placing the hollow rectangular waveguide face-to-face. Both α and S_{21} are expressed in dB. There is a factor of two in the equation because the simulated result is measured in voltage whereas the loss should be calculated in terms of power. Because power is proportional to the square of voltage, the square relation becomes a multiplication with factor of two when converted to dB.

The loss at particular frequency should be measured against the length of the waveguide. After that, linear regression should be employed to perform statistical analysis of the data. The slope of the fitting curve is the propagation loss whereas the intersection to y-axis is the coupling loss[45].

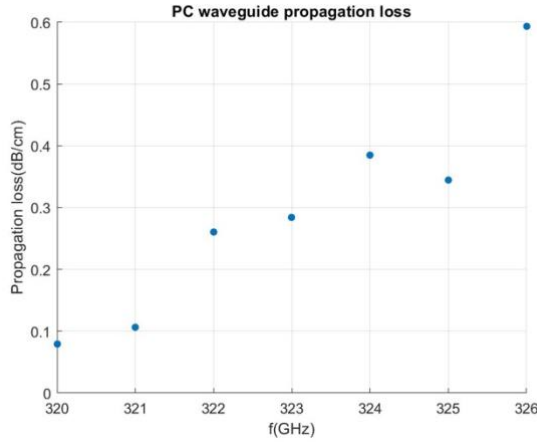


Figure 3. 13 PC waveguide propagation loss

Figure above shows the propagation loss in PC waveguide simulated at length 2 cm, 2.5 cm, 3 cm, 3.5 cm, 4 cm and 4.5 cm. The propagation loss is plotted in frequency range of $f=320\text{-}326$ GHz that has relatively stable output response. The minimum propagation loss happens at 320 GHz with value of 0.08 dB/cm, whereas the mean propagation loss averaged over the frequency range turns out to be 0.29 dB/cm. This value is two orders lower than the typical metallic waveguide loss at THz frequency (~ 10 dB/cm)[45]. The coupling loss has been computed to be 1.4 dB.

To give better visualization, the S_{21} parameter for multiple length that has relatively stable plot has been illustrated in the same graph for comparison. It can be seen that as the length increases, the S_{21} will drop slightly.

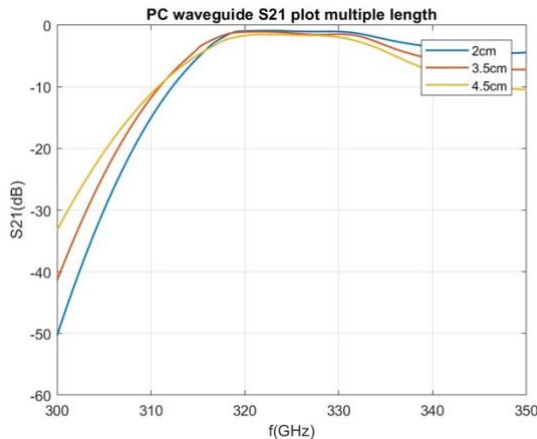


Figure 3. 14 PC waveguide S_{21} plot at multiple length

The group delay, which is defined as the time delay between the envelope of various sinusoidal signal, have been simulated in CST as shown in the figure below. The group delay measures the dispersion of the transmitted wave. We can observe that the group delay is strongly dispersive near the cutoff frequency (~ 310 GHz) where the propagating mode starts to build up. The group delay then becomes relatively flat at higher frequency.

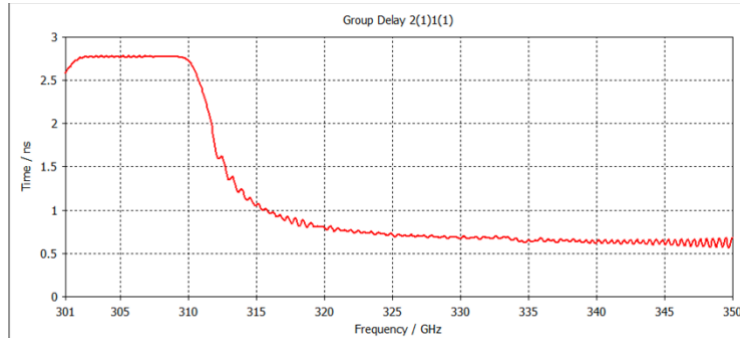


Figure 3. 15 PC waveguide group delay

The dispersion will limit the transmission bandwidth and thus needs to be minimized whenever possible. A good way to observe the dispersion effect on the communication system is to experimentally characterize the maximum data rate for different carrier frequencies.

3.3 Design of Photonic Crystal Transmitter

3.3.1 Dielectric Resonator Antenna (DRA)

We use DRA to couple the guided mode into free-space propagation mode[46]. This free-space transmission will enable inter-chip communication for photonic integrated circuit application. Moreover, DRA is chosen due to several reasons. First, it is designed based on silicon material that has a lower loss as compared to the metal-based resonant antenna. Second, it is suitable with foundry facilities as compared with the other metal-based antenna, such as metallic horn antenna that has large bandwidth but raises issue in fabrication complexity. Third, it is compact as compared with the non-resonant tapered dielectric rod antenna that has broad bandwidth and high gain but are

not compact[47]. Furthermore, the DRA has end-fire radiation, which is desired for our directed wave transmission.

DRA has dimensions in the order of $\frac{\lambda}{\sqrt{\epsilon_r}} = 333 \mu m$ [48], which classify it as a low-profile antenna. The ϵ_r value must be large enough to provide necessary field confinement in order to achieve resonance for strong field radiation (from Variational principle). In our case, the dielectric constant of silicon is sufficient to create a resonant cavity for radiation purposes.

The DRA may support different type of mode, such as Transverse Electric mode (TE), Transverse Magnetic mode (TM), or Hybrid Electromagnetic mode (HEM)[49]. In order to design the DRA, we need to first determine the desired mode and initial antenna sizing. After that, we need to solve the transcendental equation given in [50]. However, this approach is complicated and time consuming. Instead, we shall use the initial value given in [46] and optimize it accordingly.

The DRA has a limitation in terms of gain due to its small electrical size and diffraction issue. To mitigate this problem, we shall design the DRA in higher order mode. The dimension should be sized up to facilitate the higher-order mode. According to [46], we shall design the DRA to have the size of around $2.5\lambda_0$, where λ_0 is the free-space transmission wave. Eventually, this size turns out to be suitable with our photonic crystal design as it has compatible dimension for simple fabrication process. The thickness of DRA should be chosen to be the same as our photonic crystal thickness.

3.3.2 Design of Photonic Crystal with DRA for Free-Space Transmission

The figure below shows the structure of photonic crystal integrated with DRA (PC-DRA). The DRA is placed at the end to achieve end-fire radiation pattern. Air ring is designed to encircle the DRA in order to provide sharp reflection boundary due to the contrast in dielectric constant, thus creating a resonant cavity for the field to be confined. The optimized dimension can be found in the summary table presented in Appendix C.

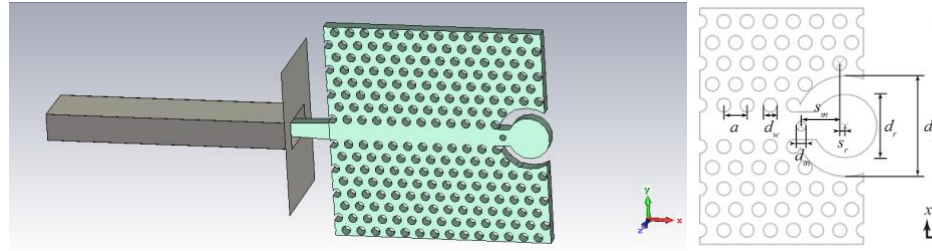


Figure 3. 16 (left) PC-DRA structure drawn on CST, (right) PC-DRA parameter

A matching air-hole is placed in between the waveguide and DRA. This is done to reduce the reflectivity by matching the coupling. The mechanism of the air-hole matching can be understood with the following explanation: on resonance condition, the wave decaying from DRA to the waveguide will interfere destructively with the wave reflected from the air-hole directly.

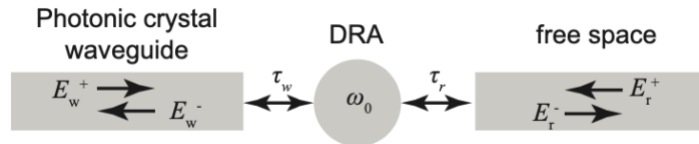


Figure 3. 17 Temporal coupled mode abstraction for PC-DRA system[46]

Alternatively, we can also examine the necessity of matching air-hole through the framework of temporal coupled-mode theory that is discussed in Chapter 2.1.4 and appendix A. The temporal coupled-mode theory states that the transmission is maximized when the decay rate from resonant cavity to the waveguides are equal. In here, we have the PC waveguide, the free-space radiation that can be considered as another waveguide and DRA as resonant cavity. In other words, the decay rate from DRA to PC waveguide must be equal to the decay rate from DRA to the free-space through radiation.

Without the matching air-hole, the decay rate from DRA to the PC waveguide will be much larger as compared to the free-space radiation. This is due to the strong coupling between PC waveguide and DRA, arising from the direct connection between these two. The presence of an air-hole will reduce the coupling between PC waveguide and DRA to satisfy the condition of equal decay rate for maximum transmission.

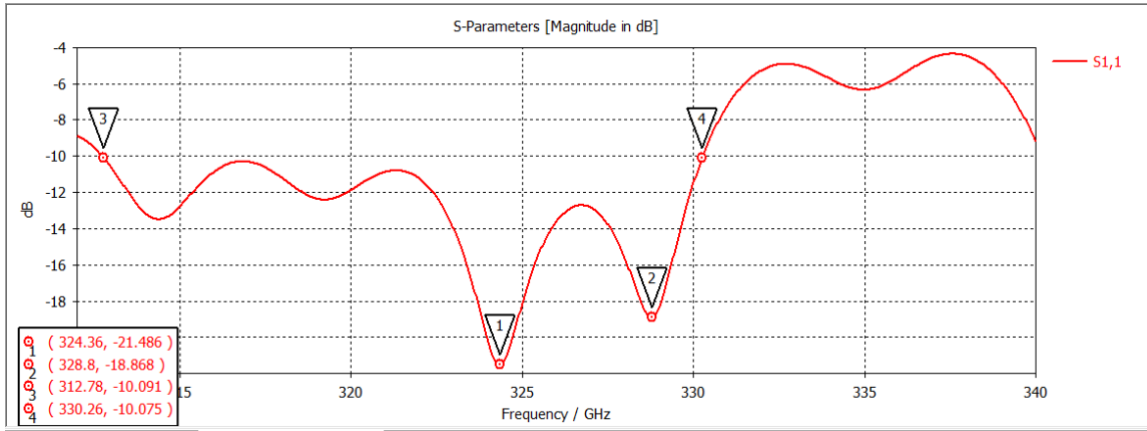
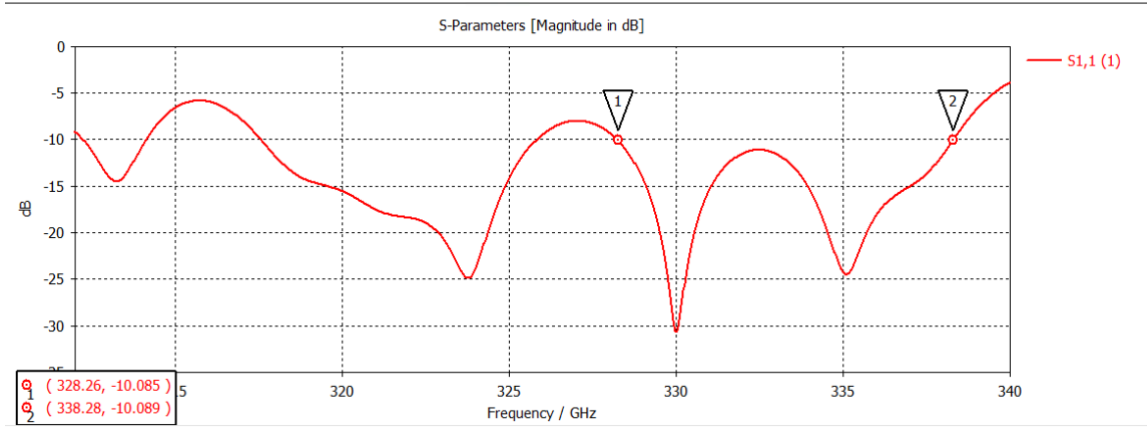
Figure 3. 18 S_{11} parameter of PC-DRA with matching air hole

Figure above shows the reflection coefficient (S_{11}) of the PC-DRA structure. The impedance bandwidth spans from 312.78 GHz (mark 3) to 330.26 GHz (mark 4), giving a total bandwidth of 17.48 GHz (Fractional BW=5.43%) corresponding to the reflection coefficient below -10 dB. As a comparison, the S_{11} parameter without the matching air hole is shown in figure below. It can be seen that the bandwidth is now reduced to approximately 10 GHz due to unmatched impedance between the waveguide and DRA at other frequency.

Figure 3. 19 S_{11} parameter of PC-DRA without matching air hole

The main resonance happens at 324.36 GHz (mark 1). Another weak resonance happens at 328.8 GHz (mark 2). This resonance is weak due to the mismatch in the impedance between the waveguide and DRA when interfaced. This causes a back reflection and will leak the wave into propagation modes inside defect line. Above 331

GHz, the reflection is high due to the absence of resonance mode inside the DRA.

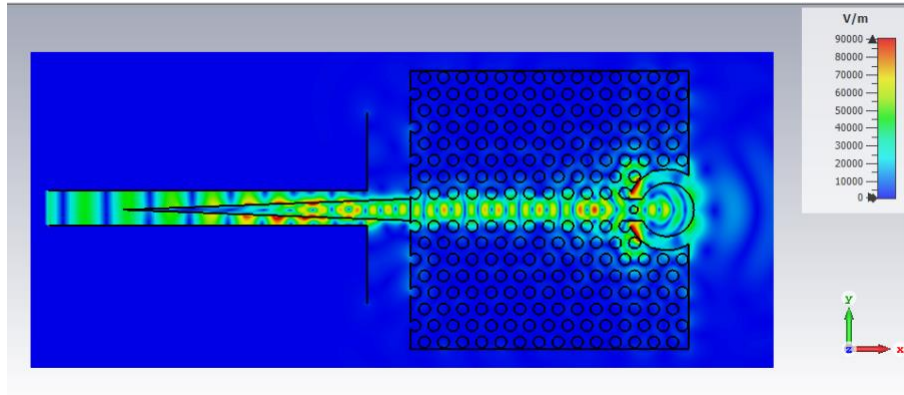


Figure 3. 20 PC-DRA E-field contour plot

Figure above shows the electric field plot of PC-DRA structure. The plot shows the distribution of Electric field on x-y cross section plane. We can observe few things from here. First, the fundamental TE mode from the horn is coupled to the tapered feed and guided to the PC waveguide. The wave is then coupled to the DRA where it is converted to higher order mode in DRA, as can be seen more clearly in the figure below.

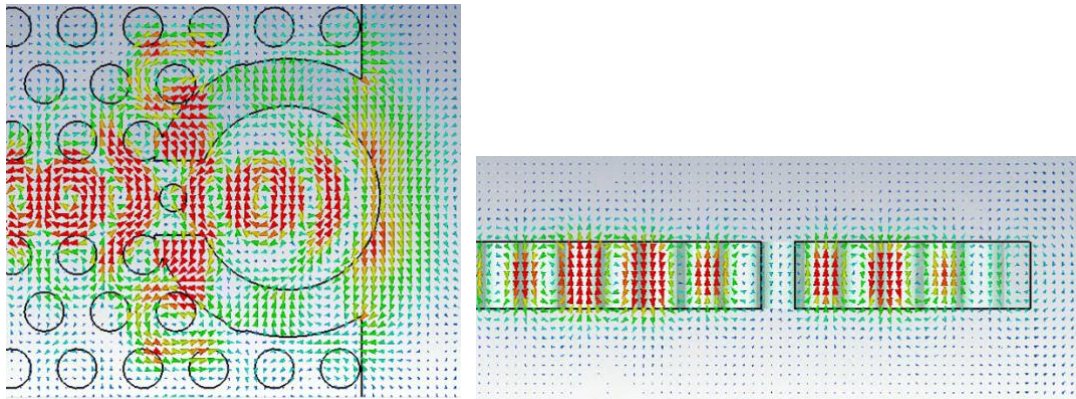


Figure 3. 21 PC-DRA E-field and H-field cone arrow plot

The field is confined inside DRA and radiating to free-space as can be seen clearly on the iso-lines plot where the near-field radiation exhibits directivity. Note that we are only interested in the near-field—as opposed to far-field—because the design is intended for on-chip application. The distance between different component are expected to be very near (in the order of few mm). The plot is shown in the vicinity of 1 mm.

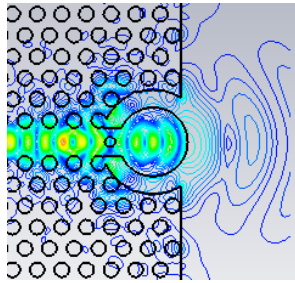


Figure 3. 22 PC-DRA E-field iso-lines plot

3.4 Design of Narrow Band Filter Based on Photonic Crystal

The narrow band filter can be designed by interfacing two waveguides with a cavity in between. The cavity is used to confine the light within a narrow frequency range and can be realized by creating a point defect. Meanwhile, the waveguide is designed to couple the incident and resonant field in the cavity as well as to drive the radiation emitted by the resonant cavity to the output.

The working principle of the filter is explained as follow. The resonant frequency wave will be coupled from the input waveguide to the cavity. The electromagnetic energy is then stored temporarily inside the cavity. After a certain lifetime period, it will be released through radiation in all direction. Since the frequency is inside the photonic bandgap range, it will be channeled along the waveguide. The waveguide will capture the outgoing power from the radiation cavity and guide the light along the defect line. Thus, it is important to design the resonant frequency of the cavity inside the photonic bandgap.

The filter behaves like a *narrow band* filter due to the fact that bandwidth (frequency) and lifetime (time) are inversely related according to Fourier inverse. The lifetime of the light inside the cavity shall be large so that it can be trapped inside the cavity to create a resonant mode, consequently making the bandwidth of resonant mode to be small. Alternatively, we can also understand this by noting that only the resonant mode will be supported inside the cavity. Thus, other frequencies outside this narrow resonant frequency bandwidth will not be coupled to the cavity and will not be passed

to the other end of the waveguide.

One way to design the cavity can be achieved by removing neighboring air-holes as shown in the figure below[51]. In here, we remove four air-holes corresponding to two adjacent holes along the waveguide channel and two air-holes on the neighboring rows of waveguide channel. With the aforementioned structure, the width and height of the cavity are 587 μm and 687 μm respectively that is close to our desired operating wavelength of 800-1000 μm (300-350 GHz). This is to make the resonant frequency inside our photonic bandgap (dimension must be in the same order as the operating wavelength). Thus, the explanation justifies why such a structure design is suitable for our application.

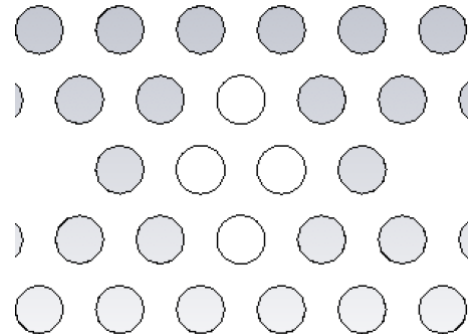


Figure 3. 23 PC filter cavity shape

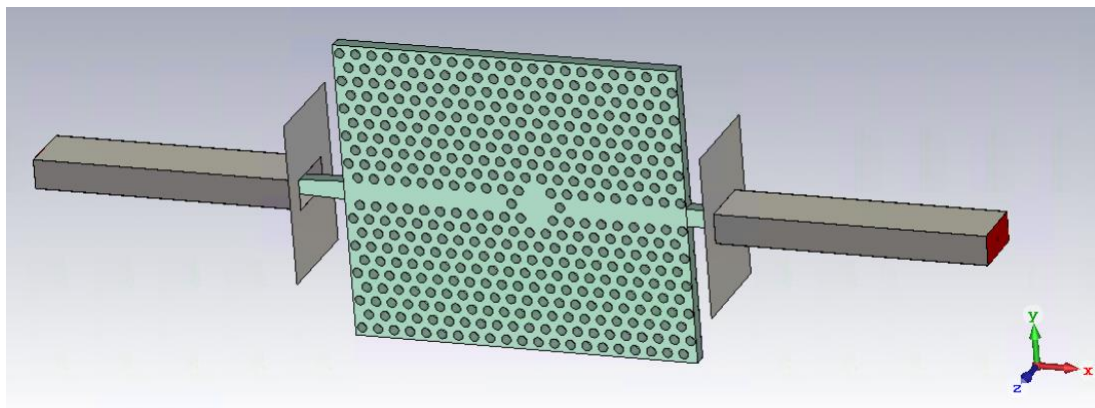


Figure 3. 24 PC Filter structure designed by interfacing waveguide and cavity

The resonant frequency and the supported mode profile inside the cavity can be obtained by COMSOL simulation. Several Eigenfrequency corresponding to different

modes are shown in figure below.

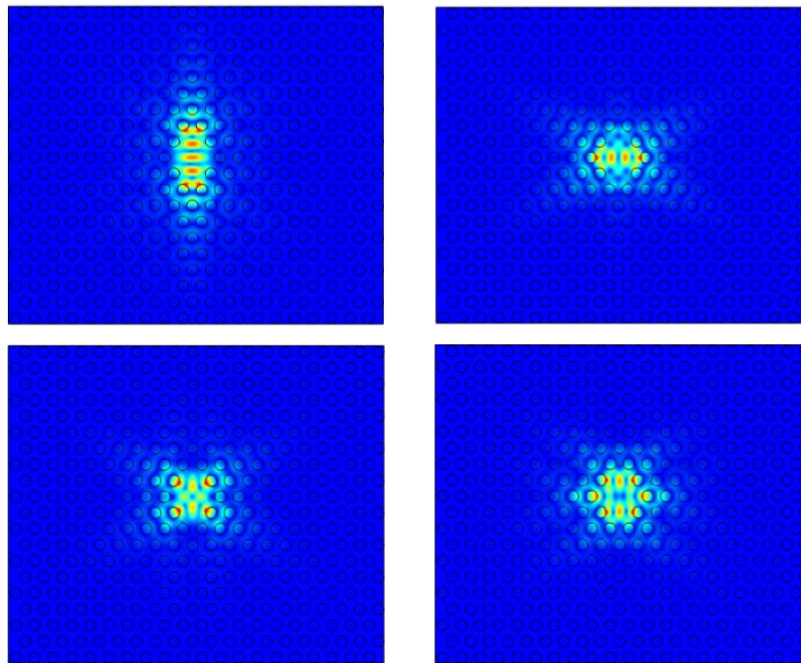


Figure 3. 25 Eigenfrequency of resonant cavity at, (from left to right) $f=308.54$ GHz, $f=315.02$ GHz, $f=321.54$ GHz, $f=339.54$ GHz

The structure was also simulated in CST. The figures below show the plot of S-parameter (S_{11} and S_{22}) and also the electric field distribution.

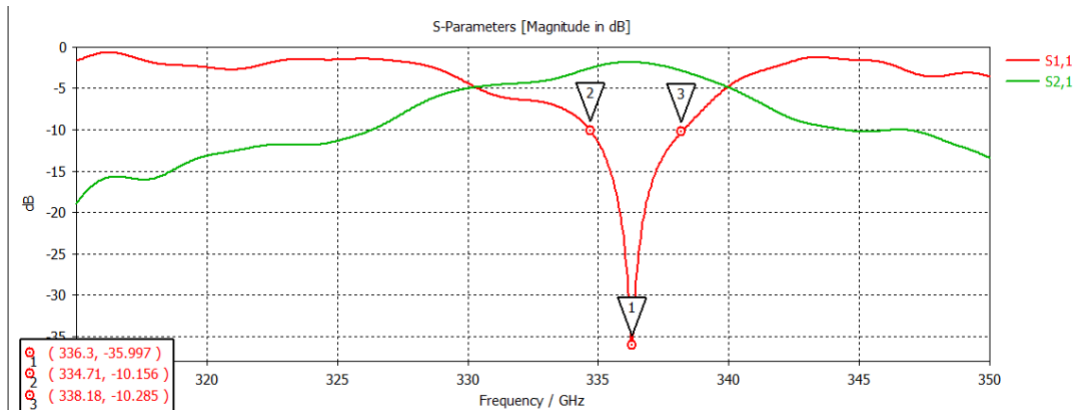


Figure 3. 26 PC filter S-parameter plot

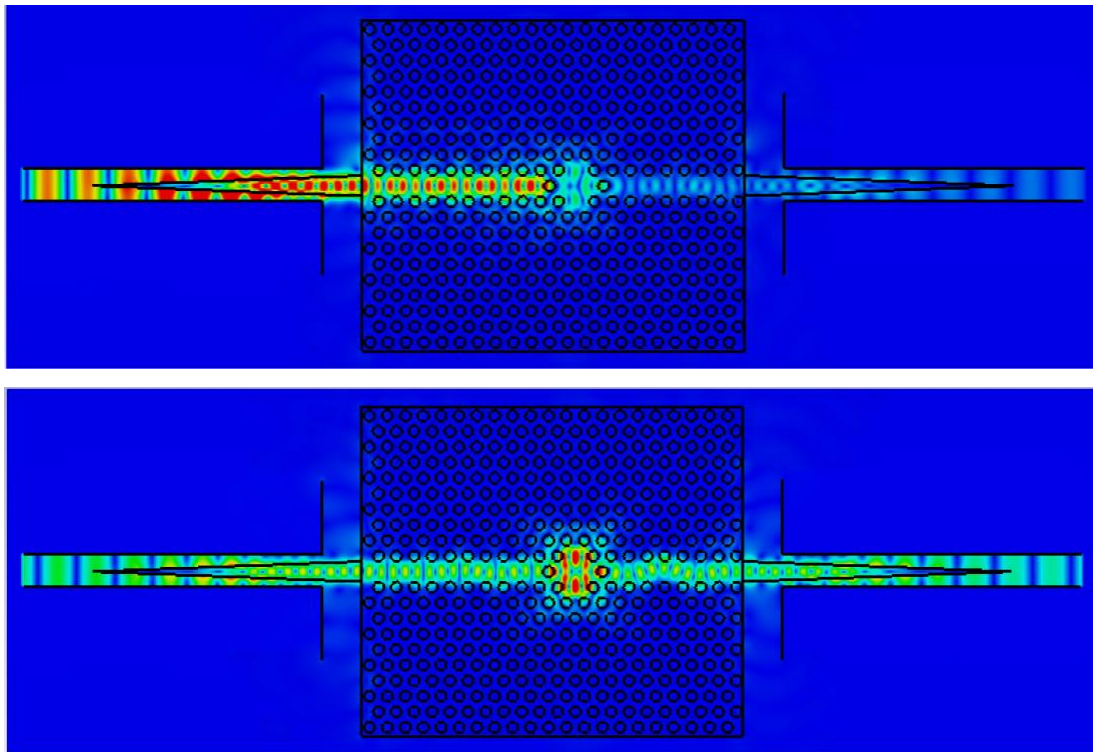


Figure 3. 27 Electric field profile at, (top) $f= 325$ GHz where field not passed and (bottom) $f= 336.3$ GHz where field are passed due to allowed resonant frequency in the cavity

We can observe a deep trough in S_{11} plot occurring at $f=336.3$ GHz. This corresponds to the resonant frequency of $f=339.54$ GHz simulated in COMSOL. The slight difference might be due to the 2D approximation of the structure. This correspondence can also be verified by observing the field plot. We can see a similar field profile inside the resonant cavity for $f=339.54$ GHz plotted in COMSOL and $f=336.3$ GHz plotted in CST.

The deep trough in S_{11} parameter would result in peak value of S_{21} parameter (ignoring absorption loss) as observed. The filter behaves as narrow band filter where it only passes a narrow range of frequency centered around the resonant frequency.

Q-factor is an important figure-of-merit (FOM) that is usually used to assess the performance of filter. The Q-factor of the filter is defined to be the ratio between the resonant frequency center with respect to the bandwidth. It is calculated based on the S_{11} plot and result in the following value:

$$Q = \frac{f_0}{\Delta f} = \frac{336.3\text{GHz}}{3.47\text{GHz}} = 96.92$$

The desired value of Q-factor depends on the application. High Q-factor means there is a peak resonance frequency and it will give a better stability. For instance, it is suitable for the application of local oscillator[52]. In some other cases, low Q-factor is desirable to give a wide bandwidth, sacrificing the device's stability.

We can also verify the temporal coupled-mode theory that we derived in appendix A. The theoretical transmission predicted by the temporal coupled-mode theory (substituting the numeric value to the equation in Chapter 2.1.4) and the simulated transmission have been superimposed in the same graph as shown in the figure below. It can be observed that the peak of the two plots coincide with each other. Thus, we can infer that the temporal coupled-mode theory is a good theoretical prediction in the case when different basic structures (waveguide and cavity) are coupled.

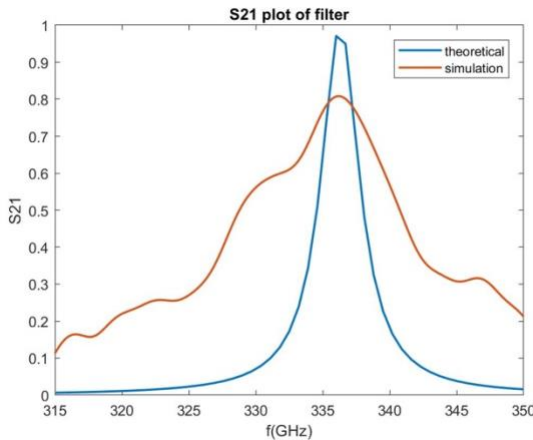


Figure 3. 28 PC filter S₂₁ plot for the theoretical and simulated value

Note that we do not observe field transmission at other resonant frequencies displayed earlier even though some are inside the bandgap range ($f=315.02$ GHz and $f=321.54$ GHz). This is because the filter design depends not only on the resonant frequency but also on two other important properties, namely the Q-factor and the mode symmetry (field distribution inside the cavity).

The field at $f=308.54$ GHz is not coupled because it is outside the waveguide's operating frequency range. Meanwhile, the field at $f=315.02$ GHz and $f=321.54$ GHz

are not coupled due to the mode symmetry. The radiation pattern at $f=315.02$ GHz shows an omnidirectional pattern whereas the radiation pattern at $f=321.54$ GHz shows a directionality in off-axis direction (60° deviation with respect to axis along the line defect). This will result in less coupling between the waveguide and resonant cavity. On the other hand, the field profile at $f=336.3$ GHz shows a strong radiation along the defect line where the field extends up to two neighboring air holes. This will result in strong coupling between the waveguide and resonant cavity and thus allowing the field transmission.

Several observations can be made further regarding the design. First, the shape of cavity determines the field pattern and the mode symmetry. Another example of cavity shape can be found in [53] for comparison. The field pattern and the mode symmetry determine if the field can be properly coupled to the waveguide to enable a field transmission. Second, the operating frequency can be changed by adjusting the dimension of cavity, for instance by changing the number of air-hole inside the cavity. This will consequently tune the Q-factor of the cavity. Alternatively, the bandgap range may be re-designed to facilitate the coupling.

The design of narrow resonant filter is very crucial in communication application. This is because the filter forms the basic building block of other devices. For example, resonant filter can be used to build a frequency multiplexer that will select the wave with particular frequency only.

3.5 Bending on Photonic Crystal

Bending is an important building block in photonic integrated circuit design as many devices would most likely includes a bend. For example, the diplexer designed in the next section will include a design of bending.

There are two loss mechanisms that happen in PC bending: reflection loss and radiation loss. Sharper bend would result in increased loss. However, the radiation loss is much lower as compared to the ordinary optical fiber. This is because the presence of bandgap in PC will prohibit radiation loss in 2D surface. Only reflection loss plays a significant role in determining the bending loss, as long as we are operating below

the light cone. This reflection loss will be reduced in the design of topological photonic crystal presented in Chapter 4.

The bending design can be formalized with temporal coupled-mode theory by considering the bending to be a cavity and the other two sides as a separate waveguide. To obtain a high transmission, the bending must be symmetric so that the decay rate from the cavity to the two waveguides are the same. However, this is not quantitatively accurate as the bending cavity is a strongly coupled devices whereas the temporal coupled-mode theory was derived with the assumption of weak coupling. In this section, we would not analyze the structure theoretically. Instead, we would just simulate a bending structure and evaluate the transmission.

A simple 60° bend is crafted in the waveguide as shown in the following figure. The capsule-shaped defect is inserted to achieve a broad band operation. The capsule-shaped defects consist of two linked air holes. The improvement in the operating bandwidth is achieved because the defect provides a smooth total internal reflection.

The S_{21} plot of the bending with and without capsule-shaped defect has been superimposed in the same graph. It can be seen that the bending with capsule-shaped defect has a bandwidth of 12 GHz whereas the bending without capsule-shaped defect has its bandwidth decreased to 7 GHz. We infer that the PC bending may be designed carefully to have a low bending loss, but it is very sensitive to the shape of bending and might be degraded due to the imperfection in fabrication process.

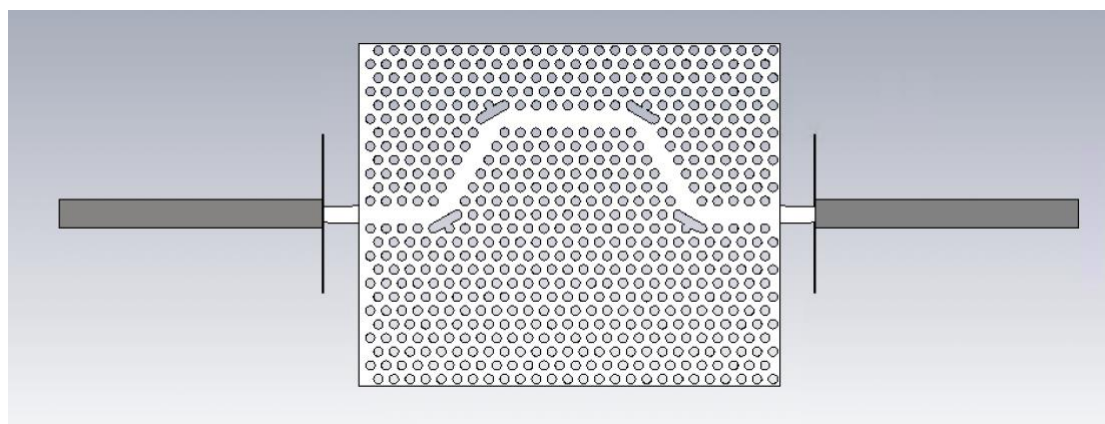


Figure 3. 29 PC bending structure

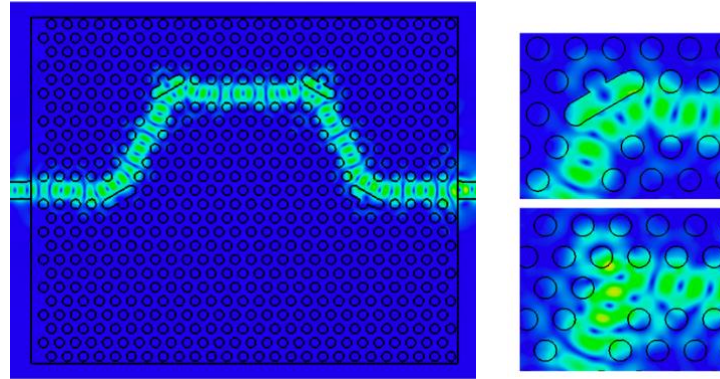


Figure 3. 30 (left) PC bending E-field, (right) close up of E-field for bending with and without capsule-shaped defect

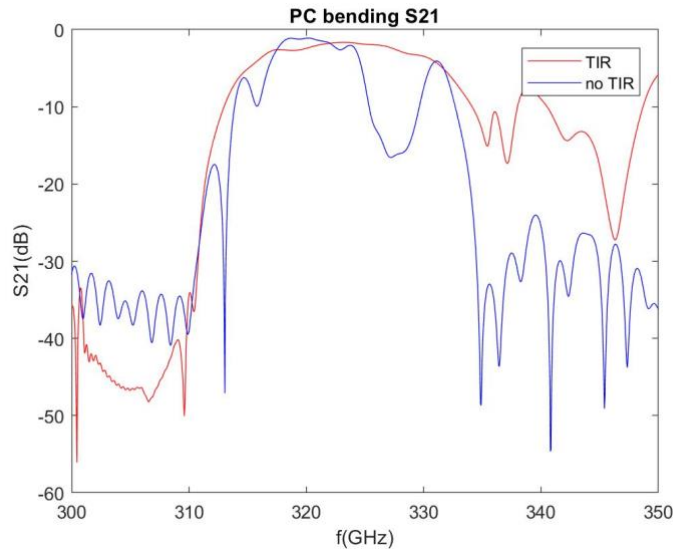


Figure 3. 31 PC bending S_{21} plot for TIR and no TIR structure

3.6 Design of Diplexer Based on Photonic Crystal

Diplexer is a passive device that performs frequency multiplexing. It selects signal with frequency in certain range and filters out the signal whose frequency is outside the range, similar to the narrow band filter designed in preceding section. Diplexer is widely used in communication application, particularly in communication channel where it enables two different devices to share common communication channel. The diplexer is built upon the basic building block of waveguide, filter and bending. The

design of diplexer is meant to show the approach in designing a more compact device by using the building block developed earlier.

Compact diplexer has been designed following the structure suggested in [54]. The diplexer is a broadband device that is composed of PC directional coupler and a cavity. The directional coupler has a flatter frequency dependence as compared to the resonant cavity and thus is used construct the broadband diplexer. To date, the directional coupler that is designed to operate in Terahertz regime has a typical length of 10 cm[55]. Some researcher has designed a miniaturized directional coupler in the order of λ [56] but has operating bandwidth of only 0.25%. In the following discussion, we will see that the directional coupler based on PC is able to achieve broader bandwidth while maintaining its compact size.

The PC directional coupler is composed of two parallel waveguides and is shown in the following figure. The working principle of a directional coupler is explained as follow. The electromagnetic energy will leak from one waveguide to the other and be coupled over. When the two waveguides are brought close to each other, they become coupled and the wave propagation forms a *supermode* where the field energy is alternating between the two waveguides as can be seen in the illustration below. The coupling length is defined to be the distance required to couple the electromagnetic energy to the adjacent waveguide.

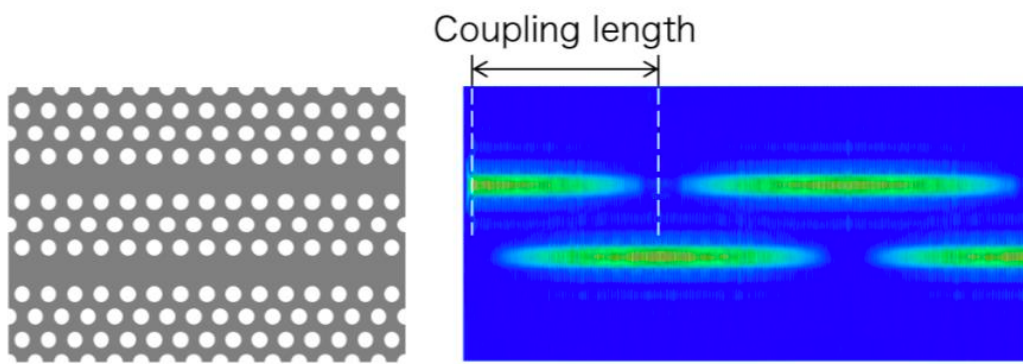


Figure 3.32 Illustration of PC directional coupler[54]

The mode in waveguide can be categorized into even and odd mode where the field will have an in-phase and anti-phase field distribution respectively as illustrated

in the following figure.

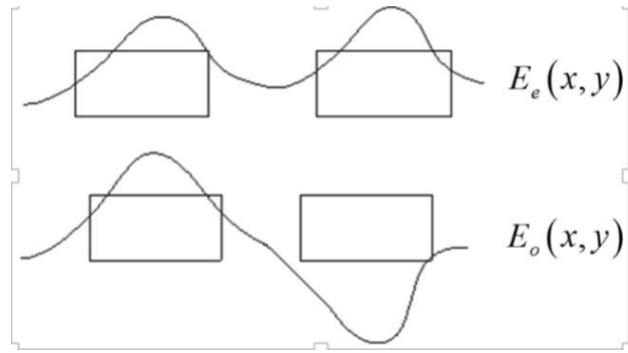


Figure 3.33 Even and odd mode in parallel waveguide

Any wave propagating along the two parallel waveguides can be decomposed into a superposition of these fundamental even and odd modes. The fundamental mode can be expressed as a sinusoidal function with phase of $\theta = kx - \omega t$. These fundamental modes have the same frequency but different wavenumber k . Owing to the difference in wavenumber, the phase difference between the even and odd modes will be shifted gradually as the wave propagate. If $\Delta\theta = \pi$, the wave will be transmitted to the neighboring waveguide.

As a simple illustration, we can imagine the even and odd mode as a simple sinusoidal wave shown in the figure above. Initially, by superposition principle, the wave is entirely confined in the left waveguide. When the odd mode has travelled with an extra phase of π with respect to the even mode, the odd mode wave will be inverted and now the wave has been transferred to the waveguide on the right side. When the phase difference is zero (or its equivalent, i.e: 2π , 4π , and so on), the wave will return on the left waveguide.

The phase difference between the even and odd mode can expressed as $\Delta\theta = (k_e - k_o)x = \Delta k \cdot x$ where k_e and k_o are the even and odd wavenumber and x are the distance travelled by the wave. Full energy transfer is achieved when $\Delta\theta = \pi$. Thus, we can obtain the expression of couple length as below:

$$l = \frac{\pi}{\Delta k}$$

The alternating wave in directional coupler is a phenomenon of spatial beat

between the even and odd modes that is caused by the difference in wavenumber. If there is no difference in wavenumber, the coupling length will be infinite, corresponding to no coupling condition. In conclusion, the wavenumber difference is crucial for the mode to couple between the two waveguides. The directional coupler behaves as a diplexer due to its frequency-dependent coupling length.

To tune the coupling length, we shall adjust the distance between the parallel waveguides. This can be done in three ways. First, we can adjust the number of air-holes rows in between the waveguides. Second, we can adjust the radii of air-holes that is between the waveguides. Third, we can change the spacing between the middle air-holes with the top and bottom air-holes.

The projected band diagram for different number of air-holes rows between the waveguides has been simulated in COMSOL and visualized in MATLAB. The results are shown in the following figure. The purple line indicates the light line. The red and green line corresponds to the odd and even mode of the wave propagation.

The field distribution has been plotted for $k=0.9$ at frequency $f=308.8$ GHz and $f=335.07$ GHz. It is observed that the lower line ($f=308.8$ GHz) corresponds to an even mode whereas the upper line ($f=335.07$ GHz) corresponds to an odd mode.

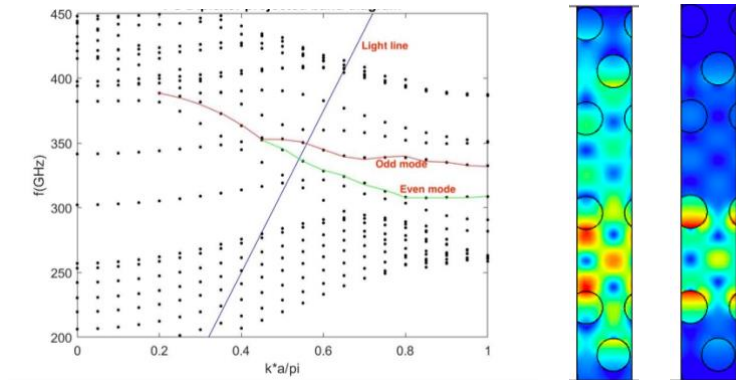


Figure 3. 34 (left) Projected band diagram for PC directional coupler with one row, (right) field distribution for $k=0.9$ and $f=308.8$ GHz and $f=335.07$ GHz

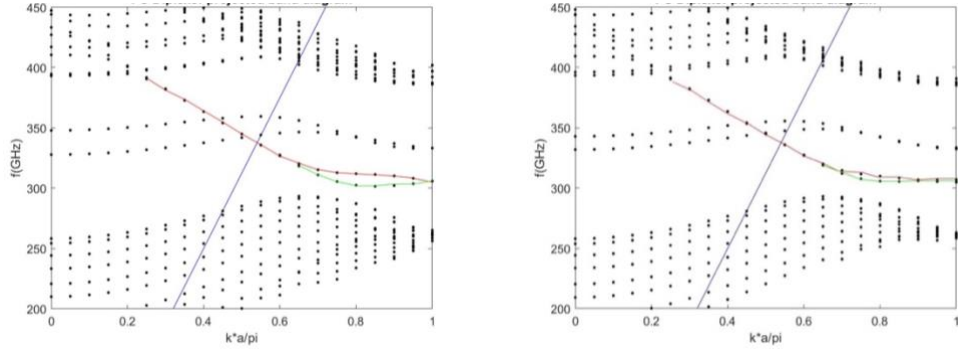


Figure 3.35 (left) Projected band diagram for PC directional coupler with two rows and, (right) three rows

From the result displayed above, it can be seen that the optimal coupling is achieved when there are two air-holes rows between the waveguides. The coupler with one row has a strong coupling strength as can be seen from the large Δk between the even and odd modes, corresponding to small coupling length. However, there is a lack of simultaneous existence of the even and odd modes at a particular frequency, resulting in unsatisfied coupling condition. Thus, there is no coupling in coupler with one row.

On the contrary, the coupling strength in coupler with three rows is decreased as can be seen from the small Δk at particular frequency, resulting in a small bandwidth. The result shows that as the distance between the waveguides increases, the coupling strength decreases. To justify further, the coupling length and bandwidth of the coupler has been simulated for different number of spacing rows and are summarized in the figure below.

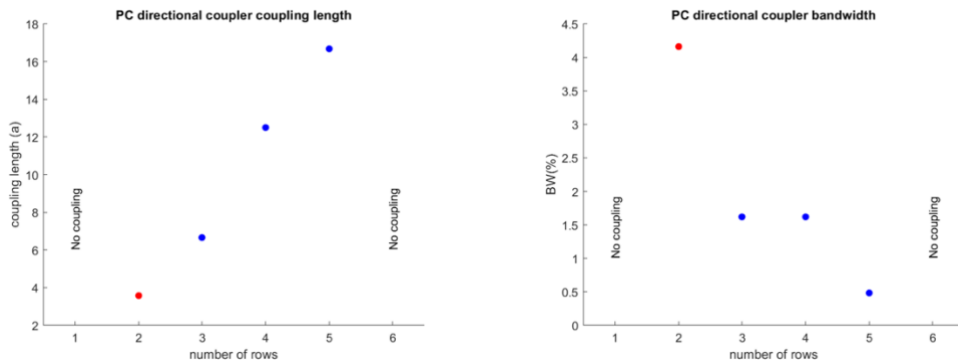


Figure 3.36 PC directional coupler (left) coupling length, (right) bandwidth

The coupler with two rows satisfies the coupling condition and has an optimal performance in terms of coupling length and bandwidth. The coupler with two rows has coupling length of 3.57a and BW of 3.26%. Thus, the coupler with two rows has been selected in our design.

Additionally, the coupling strength may be adjusted by changing the radius of the holes in the spacing rows. The figure below shows the operating frequency and the bandwidth varied with the radius of air holes.

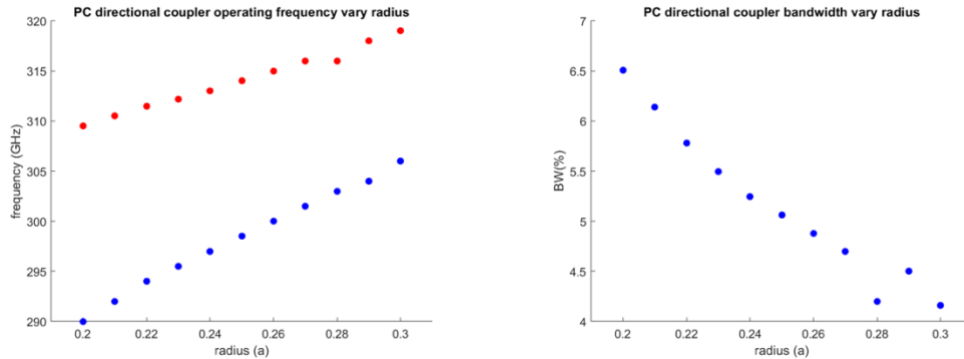


Figure 3. 37 PC directional coupler (left) operating frequency and (right) bandwidth plot varied with radius

It can be seen that $r=0.2a$ achieves the maximum bandwidth. However, the operating frequency is shifted more from the desired operating frequency ($f \sim 320$ GHz). Thus, after several times of fine-tuning all the parameters in an iterative manner and after verifying it in CST for a more practical simulation, we obtain that the optimal radius to be 0.23a.

Lastly, to match the operating frequency of the waveguide and coupler, the distance between the waveguide and coupler needs to be adjusted. When we decrease the width of a waveguide, the defect states will be pulled upward until it is completely inside the second band and there are no defect states anymore, indicating that the defect channel has disappeared. Thus, we should decrease the width between the coupler and waveguide until we achieve our desired range of operating frequency.

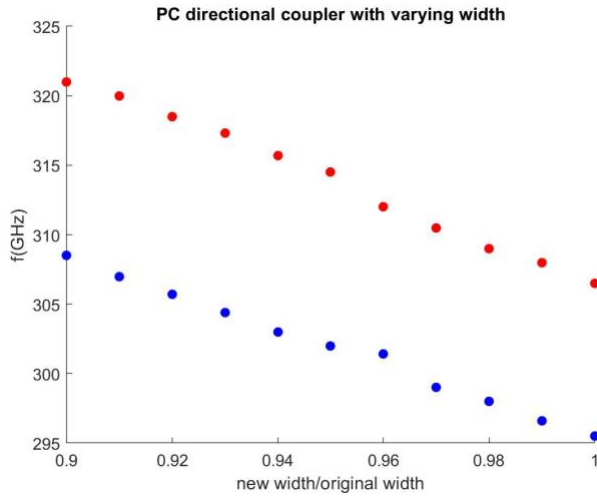
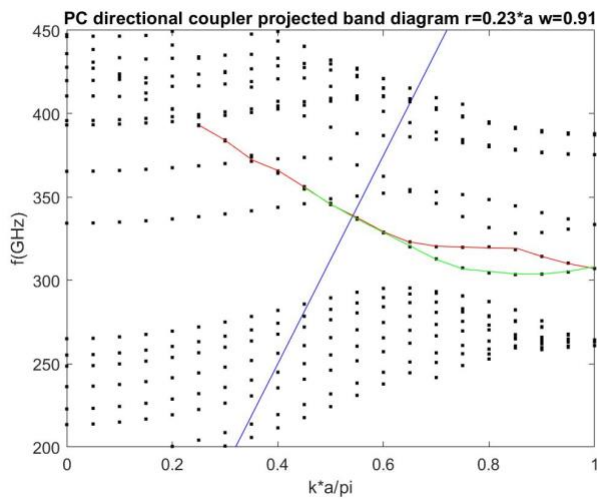


Figure 3.38 PC directional coupler operating bandwidth with varying defect width

We select the new width to be 0.91 of the original width because the operating frequency (307-320 GHz) overlaps with the operating frequency of the PC waveguide (306-335.9 GHz). The projected band diagram for the selected dimension is shown in figure below. It can be observed that the Δk between the even and odd modes are relatively constant and has a value of approximately 0.2. Constant Δk will give us a constant coupling length, that will consequently result in broadband operation. The coupling length is equal to $\frac{\pi}{\frac{0.2\pi}{a}} = 5a$.

Figure 3.39 PC directional coupler projected band diagram for $r=0.23a$ and $w=0.91$

Finally, we are ready to design the full diplexer. The structure of the diplexer is shown in figure below. The yellow air-holes are the coupler air-holes whose radius is modified to be $0.23a$. We select the coupler length to be $4a$, which is close to the calculated coupler length ($5a$). This can be obtained by modifying four consecutive air-holes along the defect axis. This coupler length is selected such that it is long enough to couple the waveguide from port 1 to port 3, but short enough to prevent it from returning back to port 2.

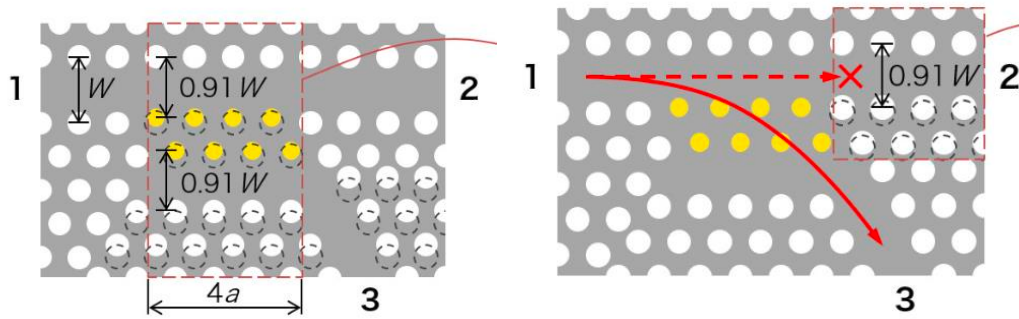


Figure 3. 40 PC diplexer design[54]

First, the wave will be guided through a defect channel with the original width of $W=271 \mu\text{m}$. This defect channel will have a transmission in frequency range of 306-336 GHz. After that, it will pass through the two-rows directional coupler with width of $0.91W$ and $r=0.23a$. This coupler will deflect wave in the frequency range of 307-320 GHz to port 3. Thereafter, another waveguide with width $0.91W$ will pass the wave to port 2. The width of waveguide to port 2 is reduced from W to $0.91W$ in order to improve the isolation.

The improvement on isolation can be explained with the following plot. The green line shows the even and off modes of the directional coupler whereas the blue and red cross shows the projected band diagram for waveguide with width W and $0.91W$. It can be seen that the waveguide with width W has its defect states inside the directional coupler bandwidth. Thus, the cross mode to port 3 can be coupled over to port 2, deteriorating the isolation. On the other hand, the waveguide with width of $0.91W$ has its defect state outside the directional coupler bandwidth and will consequently improve the isolation because no cross mode can be coupled forward to port 2.

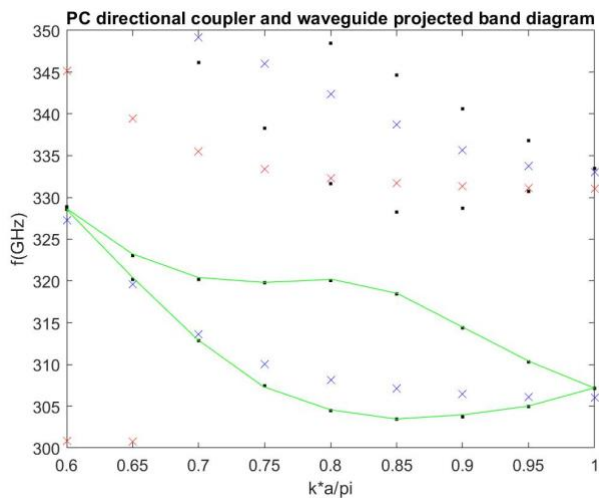


Figure 3. 41 PC diplexer and waveguide projected band diagram

The structure and the field simulation of the diplexer is shown in the following figure.

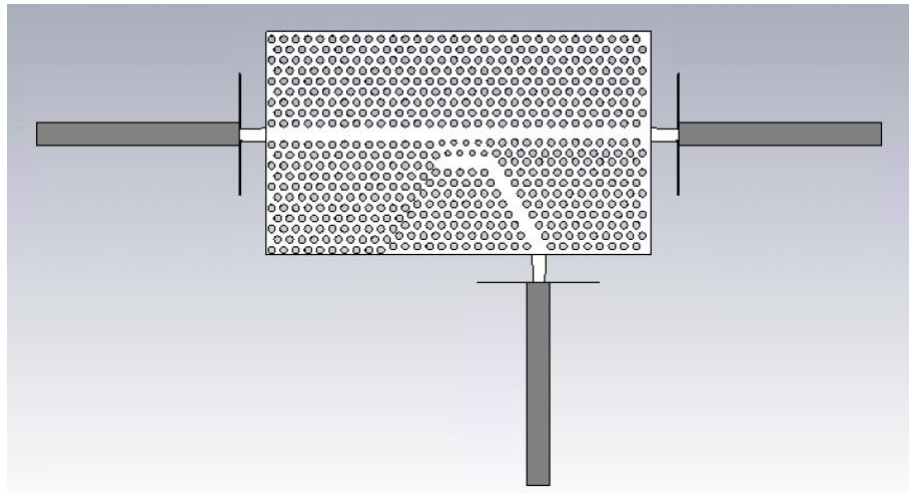


Figure 3. 42 PC diplexer full structure

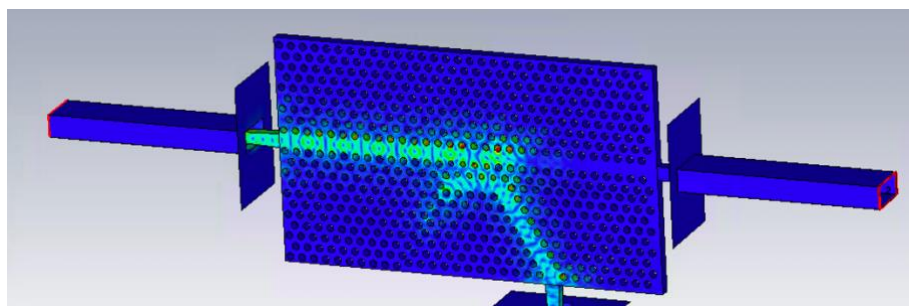


Figure 3. 43 PC diplexer E-field at $f=317.1$ GHz showing a cross transmission

Figure below shows the S-parameter plot of the designed diplexer. It can be seen that the diplexer has a transmission from port 1 to port 3 in frequency range 315.4-321.3 GHz, giving a bandwidth of 1.8%. Note that the bandwidth is different with the bandwidth calculated earlier. This is because we previously computed the bandwidth according to the cross-band frequency range. However, not all modes will be supported in the diplexer and thus will give a different bandwidth value. Furthermore, the cross port has a -40 dB isolation which is excellent in isolating the cross mode.

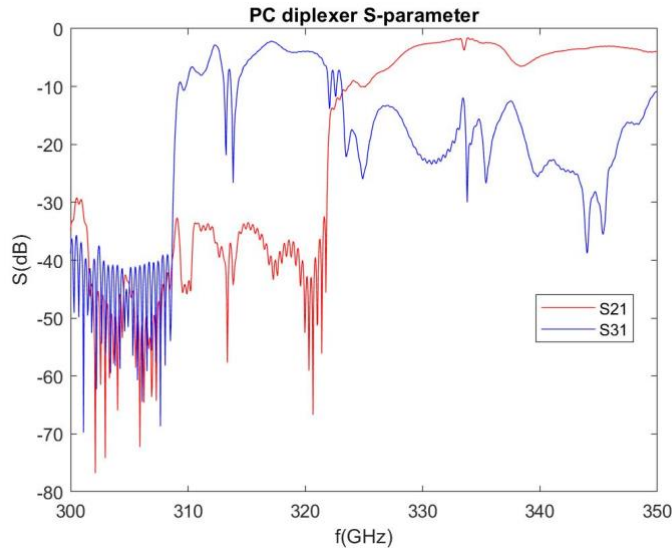


Figure 3. 44 PC diplexer S-parameter

3.7 Effect of Losses in Photonic Crystal Design

The main loss mechanism in PC design is caused by the absorption of free carriers that can be controlled by the doping density and it is quantified by the resistivity. The S₂₁ parameter for various resistivity value has been plotted on the same graph and is shown in the following figure.

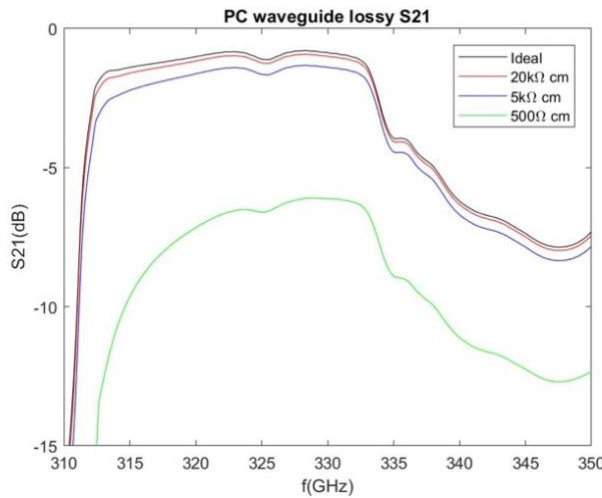


Figure 3.45 PC waveguide S₂₁ plotted at various resistivity values

Larger resistivity will result in lower absorption loss. The absorption loss mechanism can be explained by the phenomenon of phonon resonance where the atom at crystal lattice will vibrate when it absorbs the incident wave and dissipate it as heat or re-emit it at random direction. The wave will be absorbed when the frequency of the wave matches the resonance frequency of the atom. Larger resistivity will decrease the vibration of the atom because it is hard to move around material with large resistivity. Thus, the absorption loss will be reduced.

Furthermore, the absorption loss can be neglected when the resistivity is above $20 \text{ k}\Omega \cdot \text{cm}$. This can be easily acquired with the current fabrication technology. Thus, we do not need to be concerned with the absorption loss and this justifies why our simulation was done using ideal Silicon material with infinite resistivity.

Chapter 4 Topological Photonic Crystal Design

4.1 Selection of Topological Photonic Crystal Unit Cell

4.1.1 Unit Cell

Valley-hall topological photonic crystal has been selected as the structure of our design. The valley-hall TPC is a suitable choice because the interface between two such TPC supports the edge mode that are robust against scattering. The design is also able to work at the desired Terahertz frequency range. Furthermore, it is suitable with the current fabrication technology.

The Valley-hall TPC possesses a time-reversal symmetry and does not need magnetic field or temporal modulation to observe its topological nature. Other type of topological photonic crystal, such as the gyrotropic photonic crystal emulating the integer quantum hall effect would require external magnetic field to break the time reversal symmetry and to observe the topological nature[57]. This will give an advantage to the Valley-hall TPC as it will reduce the complexity of the design.

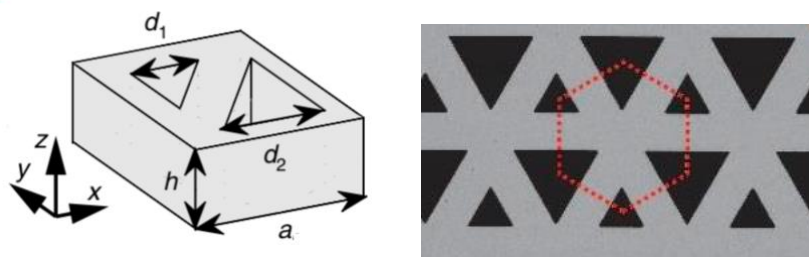


Figure 4. 1 Valley-hall Topological Photonic Crystal unit cell [58]

The unit cell is comprised of an equilateral triangular shaped hole with side length d_1 and another inverted hole with side length d_2 . The h is the thickness of the TPC substrate and a is the periodicity.

4.1.2 Atlas Gap

The atlas gap is obtained by plotting the Eigenfrequency at the edge of the Brillouin zone. The atlas gap has been simulated in COMSOL by keeping one of the length constant and varying the other. One length is fixed at $0.65a$ and the other is varied from $0.2a$ to $0.65a$. The reason for fixing one length at $0.65a$ is because this length value gives rise to the frequency gap in our desired range. As the constant length is increased, the mid-gap frequency is also increased.

The plot can be seen in following figure where the x-axis corresponds to the normalized length difference ($\frac{d_2-d_1}{a}$) and the y-axis corresponds to the normalized frequency.

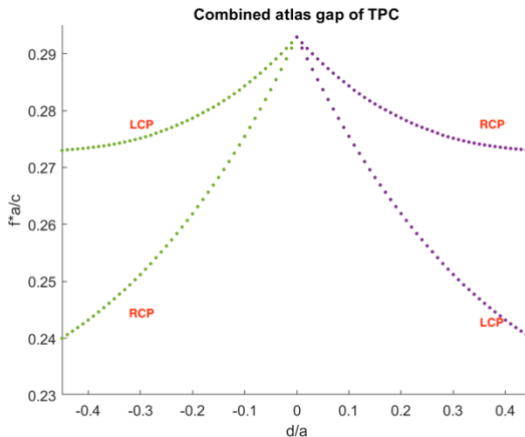


Figure 4. 2 Combined atlas gap of VPC plotted in MATLAB

It can be observed that the gap closes at $\Delta d=0$ when the unit cell possesses an inversion symmetry. Once this symmetry is broken, the gap starts to open up, as explained in Chapter 2.2.5. Furthermore, the graph is symmetrical with respect to $\Delta d=0$ due to the symmetry.

This opening of the bandgap can be understood by the breaking of inversion symmetry. We understand that the Valley-hall TPC possesses a C_6 symmetry just like graphene, that leads to the degenerated Dirac point. The Dirac point is the point where the first order band (valence) and second order band (conduction) overlap. It is said to be degenerated because a single mode (ω, k) has two different “observable”, one is

in the valence band and one is in the conduction band. Upon breaking the inversion symmetry, this degeneracy will be lifted. Thus, the Dirac point will disappear and band gap will be opened. The opening of bandgap is verified in simulation as shown in the following figure.

The black dot and red cross refer the band diagram for unit cell of $(d_1, d_2) = (0.5a, 0.5a)$ and $(d_1, d_2) = (0.4a, 0.6a)$ respectively. It can be observed that once the inversion symmetry is broken, the conduction band will be lifted up and the Dirac point will disappear.

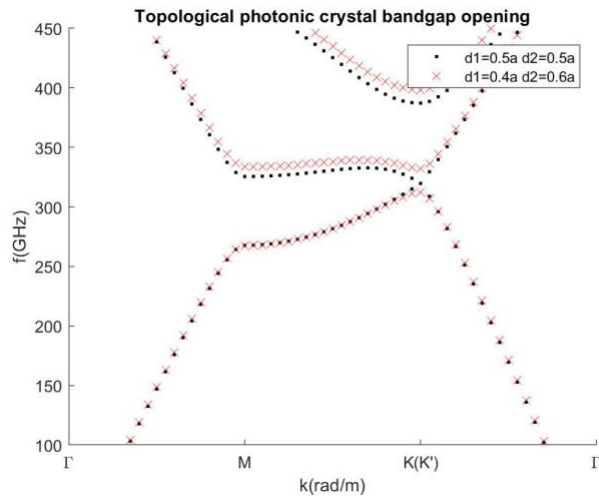


Figure 4. 3 Bandgap opening in topological photonic crystal when the inversion symmetry is broken

At the same time, we can also observe the field profile at particular frequency. For instance, the figure below shows the electric field profile when $\Delta d=0.3$ at $f=310.54\text{GHz}$ and $f=340.54\text{GHz}$. The arrow indicates the direction of the electric field.

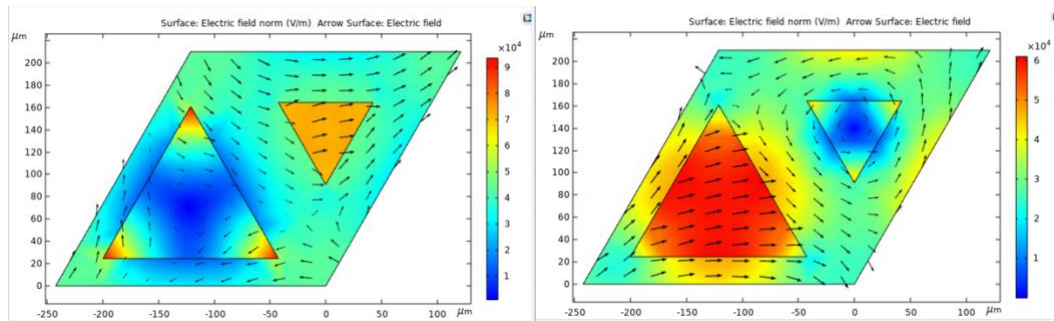


Figure 4. 4 Electric field profile plot for (left) $f=310.54\text{ GHz}$ and (right) $f=340.54\text{ GHz}$ when $\Delta d=0.3$

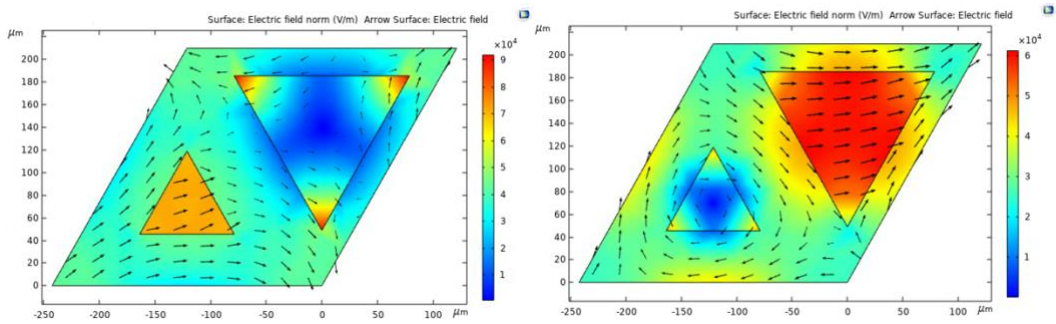


Figure 4.5 Electric field profile plot for (left) $f=310.54$ GHz and (right) $f=340.54$ GHz when $\Delta d=-0.3$

It can be seen that the frequency $f=310.54$ GHz corresponds to the Left Circular Polarization (LCP) and the frequency $f=340.54$ GHz corresponds to the Right Circular Polarization (RCP) when $\Delta d=0.3$. The polarization can be determined by looking at the direction of the electric field seen from the positive z-axis (towards the reader). If the electric field is circulating in counter-clockwise direction then it is LCP and vice versa.

Several other field profiles have been plotted and similar observation is found. The field profile on the frequency across the gap (valence and conduction band) corresponds to opposite polarization. Furthermore, the simulation also showed that the polarization states is flipped when Δd crosses zero. RCP belongs to the valence band whereas LCP belongs to the conduction band on the left side ($\Delta d<0$); RCP belongs to the conduction band whereas LCP belongs to the valence band on the right side ($\Delta d>0$). This observation verifies the Chirality in wave propagation that will be discussed in the upcoming section.

4.1.3 Selection of Dimension

After varying the dimensions, the length has been selected to be $d_1=0.35a$ and $d_2=0.65a$ where $a=242.5$ μm . The reason being is because these selected dimensions give a frequency gap in our desired range as shown in the figure below. At K, the band gap ranges from $f=310$ GHz to $f=340$ GHz. Furthermore, the height of the substrate has been chosen to be 190 μm as the process to manufacture the TPC is optimized in this particular height.

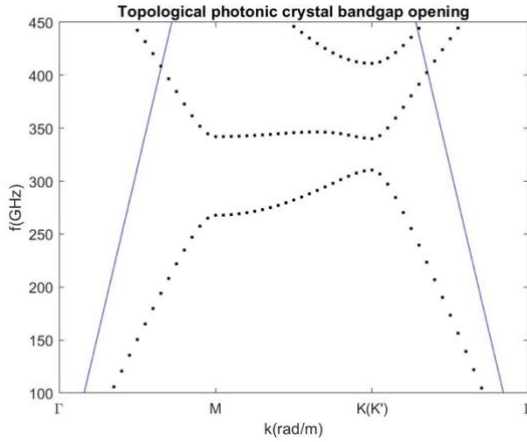


Figure 4. 6 Band Diagram for VPC at $d_1=0.35a$ and $d_2=0.65a$

There are several observations that we should note. First, increasing the lattice constant a while keeping the rest as constant would shift the bandgap to lower operating frequency and will reduce the bandgap size as the gap-to-midgap ratio is preserved by scaling. Second, the larger the Δd , the wider the bandgap will be.

4.2 Design of Topological Photonic Crystal Waveguide

4.2.1 Working Principle

Topological photonic crystal waveguide can be designed by interfacing two valley-hall photonic crystal (VPC) with opposite Δd value to form an edge (domain wall). The two unit cells are shown in the figure below.

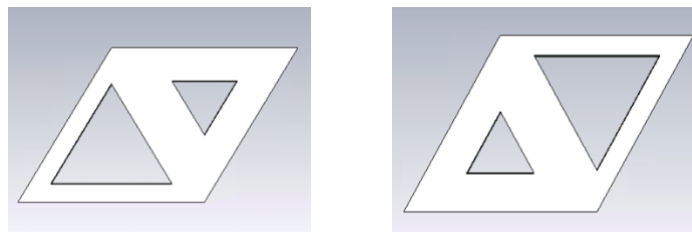


Figure 4. 7 VPC unit cell (left) type A, (right) type B

The non-zero Berry curvature has been found to be localized at K and K' valleys but with opposite sign[59]. The total berry curvature over any single band would then be summed up to zero, which is guaranteed by the time-reversal symmetry.

Further integration of the Berry curvature would result in valley-Chern number of value $C_K = 1/2$ and $C_{K'} = -1/2$ on the valence band and $C_K = -1/2$ and $C_{K'} = 1/2$ on the conduction band[60]. This would give a difference in valley-Chern numbers between the VPC domain at the Dirac points (K or K') to be $C_\Delta = \pm 1$. The bulk-boundary correspondence states that the number of edge modes is equal to the difference in Chern-number at the boundary[61]. Thus, there must exist a pair of edge mode appearing at the domain wall within a band gap. These edge modes are the valley-polarized topological kink states that are locked to either K valley that propagates forward or K' valley that propagates backward, resulting in unidirectional transfer.

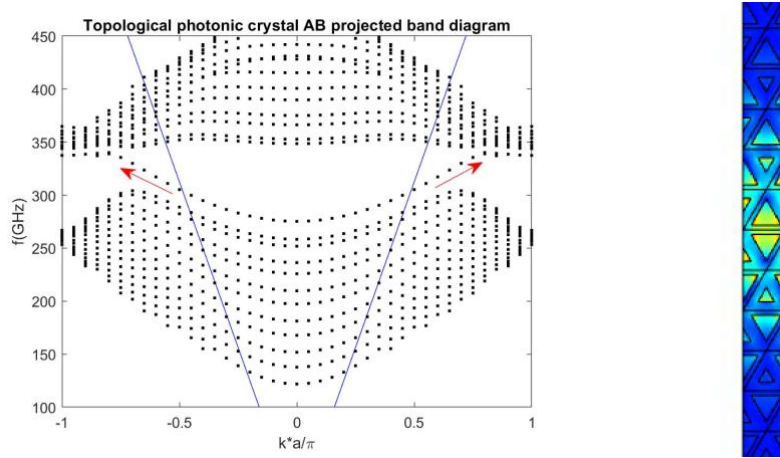


Figure 4. 8 (left) Projected Band Diagram type AB, (right) field distribution at $f=339$ GHz, $k=0.8$

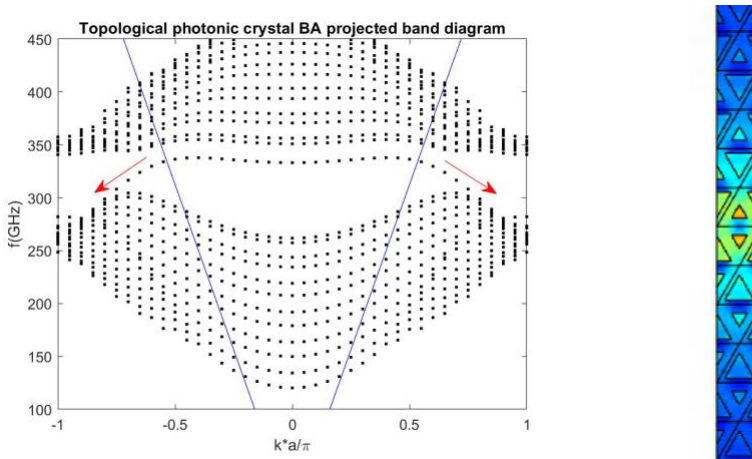


Figure 4. 9 (left) Projected Band Diagram type BA, (right) field distribution at $f=308$ GHz, $k=-0.75$

The projected band diagram has been simulated in COMSOL and plotted in the

figure above. Two type of structure has been simulated: type AB refers to waveguide formed by stacking unit cell type A on top of unit cell type B and type BA refers to waveguide formed by stacking unit cell type B on top of unit cell type A. Due to the symmetry, the edge modes should be opposite to each other, as can be seen by the opposite arrow direction in the projected band diagram.

The electric field profile has been plotted as well. It can be observed that the wave is indeed guided along the interface between different VPC type. Furthermore, the simulation shows that the VPC waveguide possess a bandwidth of 25 GHz from 305 GHz to 330 GHz.

There are some few observations to be made. First, there exists the edge mode inside the bandgap which is indicated by the curved dotted line. The bandgap occurs in our desired operating frequency. In this case, the bandgap occurs in the range of 280 GHz-340 GHz.

Second, there is a unidirectional wave propagation as indicated by the slope of the curve. We know that the group velocity of the wave can be expressed with the following expression[62]:

$$v_g = \frac{1}{\hbar} \frac{\partial E}{\partial k}$$

where \hbar is the planck constant. The group velocity is linearly proportional to the slope of the curve in band diagram (ω_n vs k , E is proportional to ω_n). For discussion, we will just consider the type AB. Similar argument can be applied for type BA.

In type AB, we can observe that the slope is positive for $k>0$, implying that all the wave are propagating forward. On the other hand, the slope is negative for $k<0$, implying that all the wave are propagating backward. This validates the uni-directional propagation of the wave that eliminates the loss due to back reflection.

Once we send in the wave, the state will be locked to either of these k (*valley-locking*) and it will eliminate all the backpropagation wave. In other words, when we send a wave from the left to right port, the wave will travel unidirectionally from left to right, corresponding to the positive group velocity at $k>0$. If we send the wave from the right to left, the wave will travel unidirectionally from right to left, corresponding

to the negative group velocity at $k<0$. Once we send the wave in one direction, it will be locked at a single propagation direction and will not allow any back propagation coming from possibly reflected wave.

Third, the edge mode is a single mode. This can be observed from the fact that there is only a single line inside the bandgap, as contrasted to the projected band diagram of photonic crystal that has multiple defect lines inside the bandgap as can be seen in fig. 3.7. This single mode property is desired for our communication application as it will eliminate unnecessary interference between different modes. This allows us to control the mode propagation inside the waveguide as well. Furthermore, it provides advantages similar to single-mode optical fibre, such as increased bandwidth capacity, fast transmission speed and etc[63].

Fourth, the dispersion happens almost linearly as has been explained using 2D massive Dirac Hamiltonian Model in [64]. Intuitively, this can also be observed from the edge states that has almost constant slope, with some negligible higher order term involved due to valley curve. This linear dispersion is beneficial for communication application. The reason being is linear dispersion will allow wave with different frequency to travel at the same group velocity. This will produce a less distorted pulse shape and thus smaller signal delay. This in turn will enable a larger bandwidth.

Alternatively, the uni-directional transfer of wave can also be understood by the polarization observed in the atlas gap. We note that in the same band, an opposite value of Δd would result in opposite polarization of wave (LCP and RCP). Let's take a closer look at the interface along which the wave is guided.

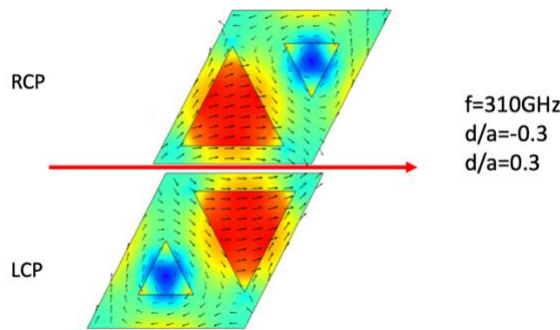


Figure 4. 10 Close look at VPC interface

The two stacked unit cells have an opposite value of Δd . These two unit cells have an opposite polarization of LCP and RCP at the same band, as has been observed from the field plot of atlas gap. Let's consider the case when the propagation of wave is locked at K valley where the bottom unit cell has an LCP and the top unit cell has an RCP as illustrated. This different polarization will result in uni-directional propagating wave as can be seen from the arrow direction along the interface.

4.2.2 Design of Topological Photonic Crystal Waveguide

The topological photonic crystal waveguide has been designed in CST and the structure is shown in the figure below. The TPC waveguide has a bandwidth of approximately 9.55 GHz.

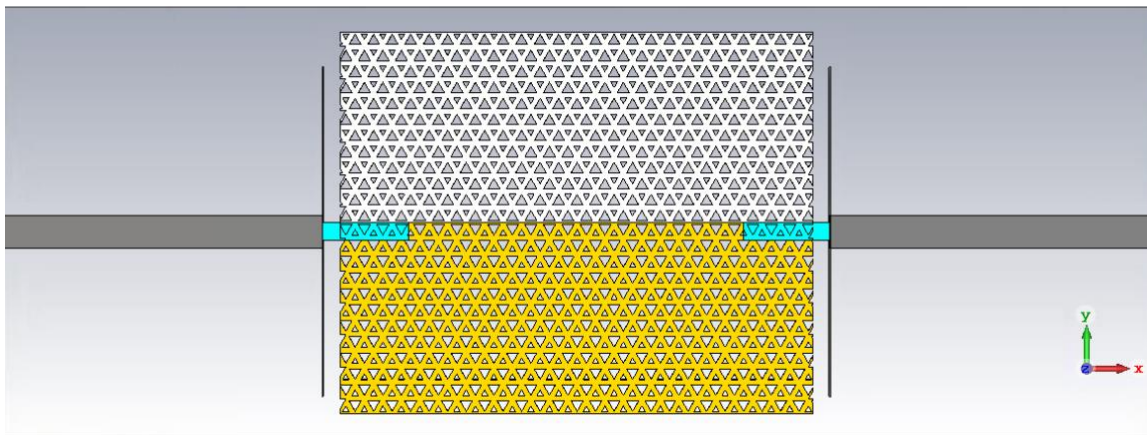


Figure 4. 11 VPC waveguide structure

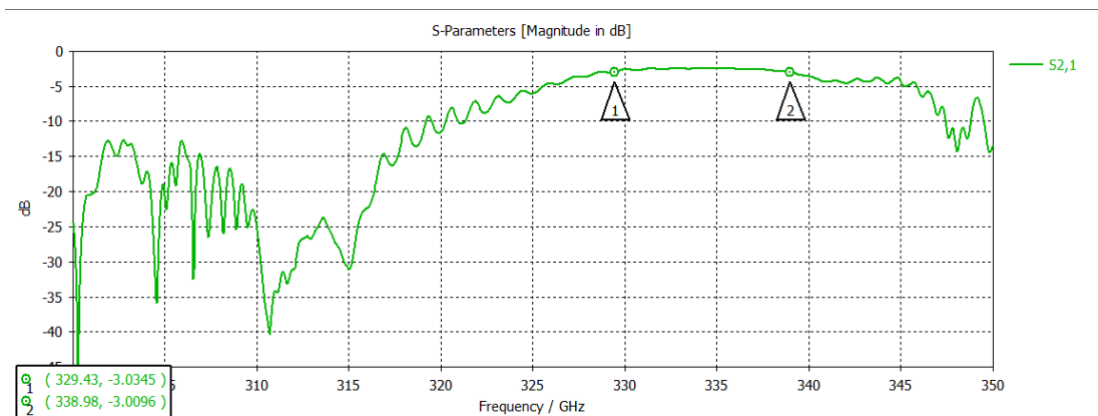


Figure 4. 12 VPC S₂₁ plot

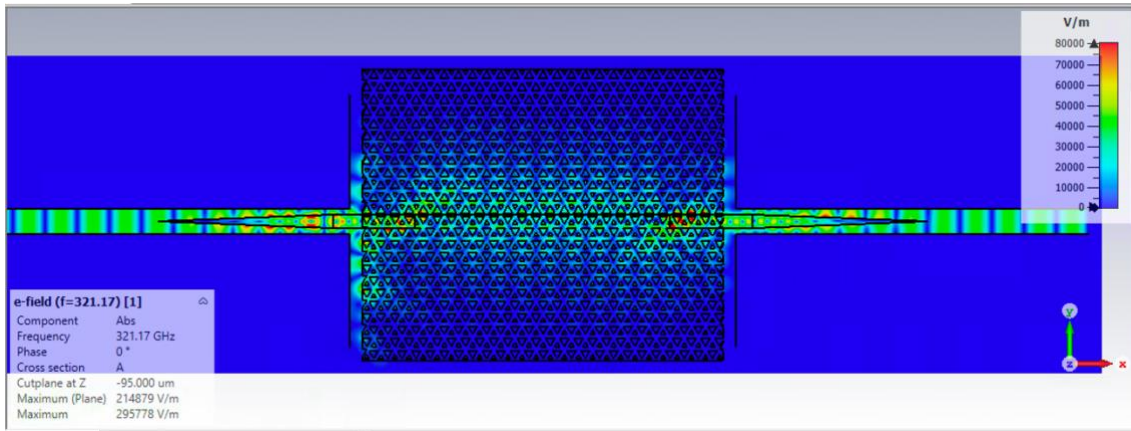


Figure 4. 13 VPC electric field plot

From the electric field plot above, we can observe the wave being guided from the input to the output port along the domain wall. The evanescent wave is extended upward and downward the unit cell due to the photonic bandgap present. It can be observed that the wave is not allowed to propagate inside the bulk (*insulator*) but only allowed to propagate along the interface. This is in analogy to the topological insulator that is insulating in the bulk but conducting at the edge. The topological photonic crystal is sometimes called as the Photonic Topological Insulator due to the analogy between the topological photonic crystal and topological insulator.

The propagation loss has been computed at different length and plotted in the graph below. The average propagation loss is computed to be 0.05 dB/cm over the stable simulated operating frequency from 330-340 GHz range. Meanwhile, the coupling loss is computed to be 5.55 dB.

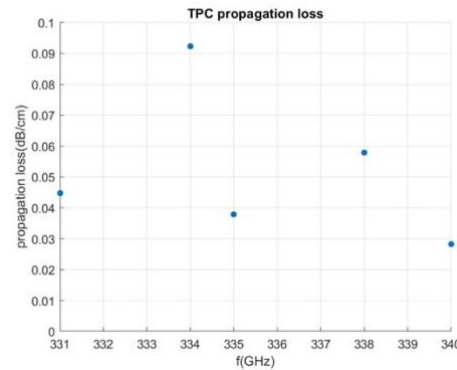


Figure 4. 14 TPC propagation loss

4.3 Design of Resonant Tunneling Diode as Miniaturized Source

4.3.1 Working Principle

In order to design a compact integrated Terahertz chip, miniaturized source and detector must be designed. One possible way is to utilize metallic deep-subwavelength structure to aid the integration. However, there is a significant difference in physical scale between the metallic deep-subwavelength and dielectric waveguide platform. For example, a typical metallic deep-subwavelength structure has dimension in the order of $0.1 \mu\text{m}$ [65], which is much smaller than the width of the waveguide channel. Furthermore, there is often a mismatch between the mode distribution of metallic deep-subwavelength structure and dielectric waveguide platform. Thus, coupling between the source, waveguide and detector might not be efficient. The severe Ohmic loss may also suppress the benefits of the structure.

One particular instance of deep metallic sub-wavelength structure is the Resonant Tunneling Diode (RTD). RTD is an active device that has the advantages of having compact structure, low power-consumption, and can act as both sources and detectors in THz regime at room temperature[66]. The typical dimension of RTD must be smaller than $2 \mu\text{m}$ for operation in THz regime. To bridge the physical dimension, RTD should be designed on a substrate with compatible dimension, forming an RTD chip. Furthermore, efficient mode converter shall be designed as well to match the difference in the field mode distribution.

The structure of an RTD is shown in the following figure. The figure shows a typical layer structure of RTD fabricated on Indium Phosphide (InP) substrate. The resonant tunneling layer of RTD is composed of Indium Gallium Arsenide (InGaAs) sandwiched with the double barrier structure of Indium Aluminum Arsenide (InAlAs). InGaAs acts as a quantum well region whereas InAlAs acts as a potential barrier region. Two heavily doped n+ GaAs layer will be layered at the terminals (InAlAs outer side). The electron density of the electrode can be made extremely large such that we can

treat it as metallic electrode.

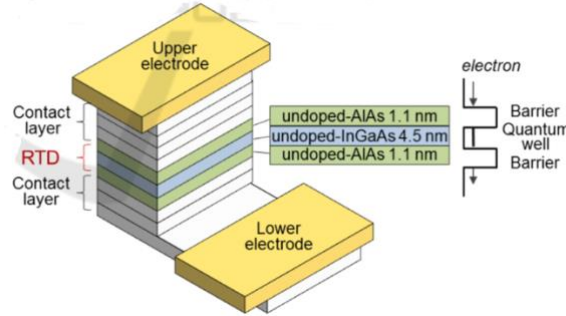


Figure 4. 15 RTD internal structure [67]

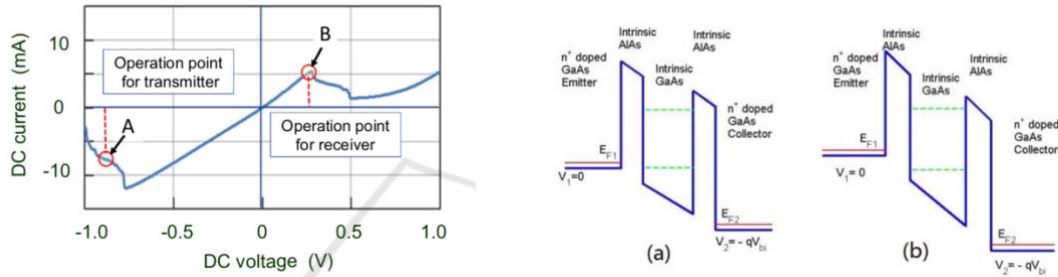


Figure 4. 16 (left) RTD DC I-V characteristics[67], (right) band structure of electron energy[68]

We can design the upper and lower contact layers to be asymmetric to alter the DC I-V characteristics. The negative resistance operating region is suitable for a transmitter or source operation. This is similar to Bipolar Junction Transistor (BJT) amplifier or cross-coupled structure that has negative impedance to produce energy and amplified the signal. Meanwhile, the positive resistance region can be used for receiver or detector operation.

Figure above shows the band structure of electron energy. The green dotted line illustrates the resonant energy of the quantum well which is the allowed electron energy level. E_F refers to the fermi energy level of the electron in the respective semiconductor layer.

The negative resistance of RTD originates from the quantum nature of electron where the electron states are discrete in quantum well. Only electrons with resonant energies of quantum well may tunnel through the barriers. In the negative resistance region, when the bias is increased slightly, the resonant energy level drop below the

fermi level. Electrons in emitter can no longer tunnel through the quantum well, leading to significant drop of current in I-V characteristics. This gives rise to the negative resistance of RTD.

4.3.2 Design of Resonant Tunneling Diode

The design of RTD adopts the structure in [67]. The structure is shown in the following figure.

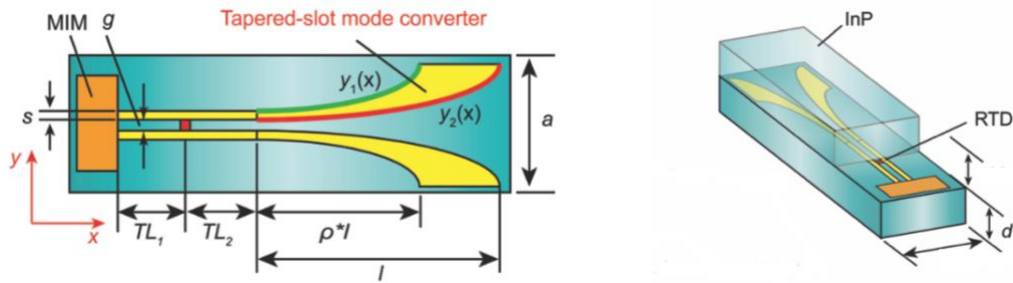


Figure 4. 17 (left) RTD design cross section with top view, (right) RTD design side view[67]

The RTD is integrated on a substrate with tapered slot mode converter. The substrate is made from InP with permittivity of 12.6. The substrate is designed to be as thick as the topological photonic crystal (TPC) structure ($d=0.5*190\ \mu\text{m}=95\ \mu\text{m}$) for better integration. The thickness allows confinement of light and provides mechanical stability as well. The width of the substrate is designed equal to the width of a unit cell of TPC ($a= 242.5\ \mu\text{m}$). The length of the RTD is designed to be long enough to support the tapered slot mode converter.

The tapered slot mode converter is designed to bridge the physical dimension difference between RTD and TPC and to provide an adiabatic-impedance matching for better power transmission efficiency and broadband characteristic. The tapered slot has exponential curve profile defined as follow:

$$y_1(x) = \left(\frac{a - g - 2s + 2}{2}\right)^{\frac{x}{\rho l}} + s$$

$$y_2(x) = \left(\frac{a - g + 2}{2}\right)^{\frac{x}{\rho l}}$$

where $y_1(x)$ and $y_2(x)$ are the outer and inner curve, a is the substrate width, g is

the dimension of the gap in straight slot, s is the thickness of the straight slot and ρ is the coefficient that determine the curvature.

There are several parameters that can be tuned to optimize the structure: l , ρ , TL_1 , TL_2 and g . Increasing l can increase the coupling efficiency and propagation loss at the same time. The propagation loss comes from the Ohmic loss and radiation loss caused by leakage into substrate when the velocity of wave is greater in metal than the group velocity in substrate[69]. On the other hand, decreasing the taper length may cause increase in reflection loss due to impedance mismatch. Thus, there is an optimal value of the taper length. Similar observation can be observed for ρ as well.

The Metal-Insulator-Metal (MIM) acts as a mirror to reflect back the reflected wave from RTD. The RTD has optimal position between MIM and the exponential slot. It has been found that the optimal position occurs when $TL_2=0$.

The structure has been simulated in CST. Note that as the RTD possesses a quantum nature, thus it cannot be simulated directly in CST. Instead, the RTD will be modelled as a discrete source port or discrete detector port. The structure and simulation result are shown in the following figure.

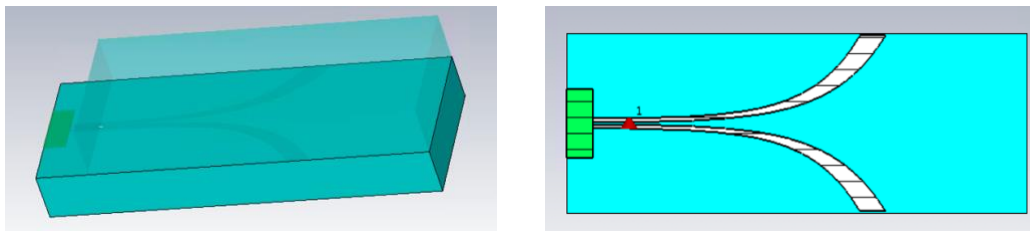


Figure 4. 18 RTD Structure drawn in CST, (left) 3D View, (right) cross section with top view

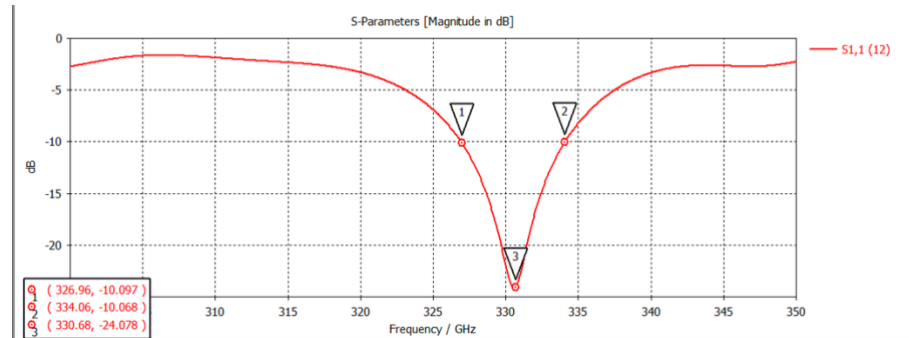


Figure 4. 19 S_{11} parameter of RTD

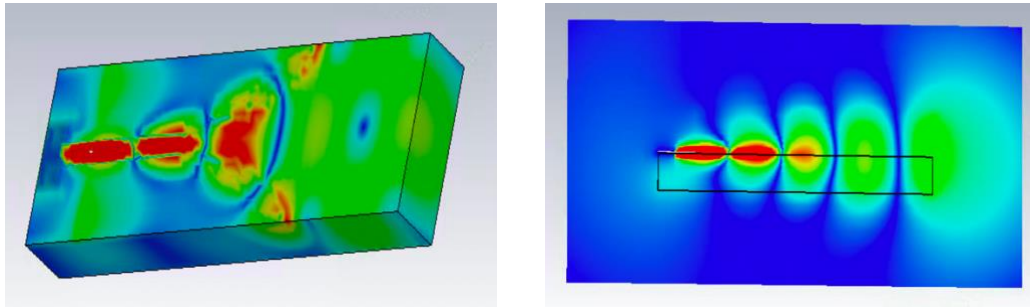


Figure 4. 20 RTD field distribution at $f=331.35$ GHz, (left) 3D view, (right) cross section side view

From the field distribution, it can be clearly seen that the field is properly converted and guided in the dielectric substrate. The S_{11} plot shows that the RTD achieve a bandwidth of 7.1 GHz and operate in our desired operating frequency region.

4.3.3 Integration of RTD with TPC

The RTD design has been optimized for TPC design. The following figure shows the structure drawn in CST and the simulation results. The transmission achieves a bandwidth of 5.61 GHz. There is discrepancy obtained due to the slight impedance mismatch between the RTD substrate and VPC structure.

The RTD can also be designed as a detector by changing the RTD discrete source port to be a discrete detector port in CST. In practical application, the RTD chip can be operated as a detector according to the bias voltage applied across it.

Similarly, the RTD source or detector can also be designed for PC by optimizing it using the thickness of the PC and the width of the defect channel.

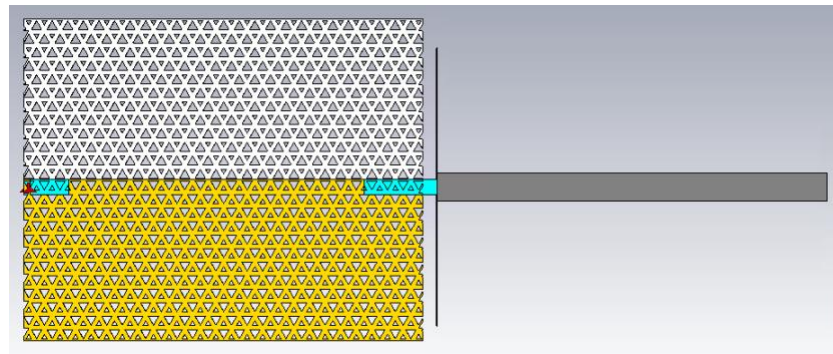


Figure 4. 21 RTD VPC Structure

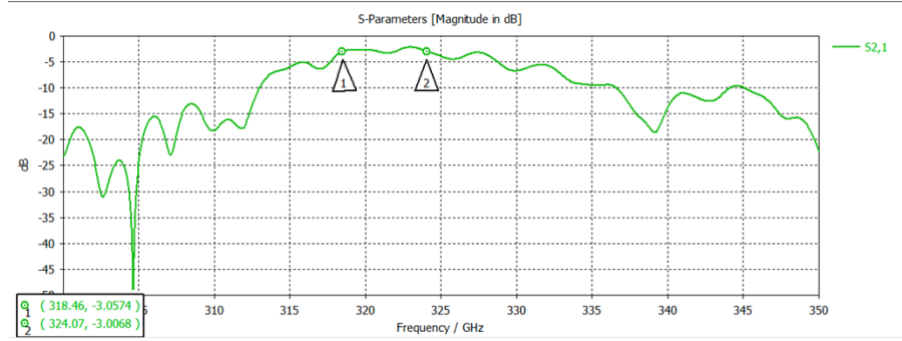


Figure 4. 22 RTD VPC S₁₁ parameter

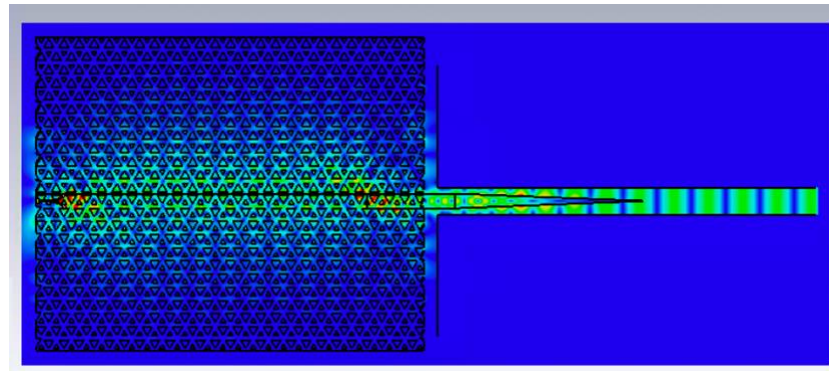


Figure 4. 23 RTD VPC E-field distribution

4.4 Demonstration of TPC Robustness Against Defect

As mentioned earlier, one of the biggest advantage of TPC is that it has a suppressed inter-valley scattering that will result in uni-directional transfer of light. This can be demonstrated by simulating the transmission field of VPC with sharp bending. This sharp bending can emulate the presence of defect or impurity that will deflect the light to certain direction.

12 bends with 60° orientation has been made. Figure below displays the E-field distribution of the bended structure. It can be observed that there is a smooth transition of E-field, as opposed to the bended structure in photonic crystal.

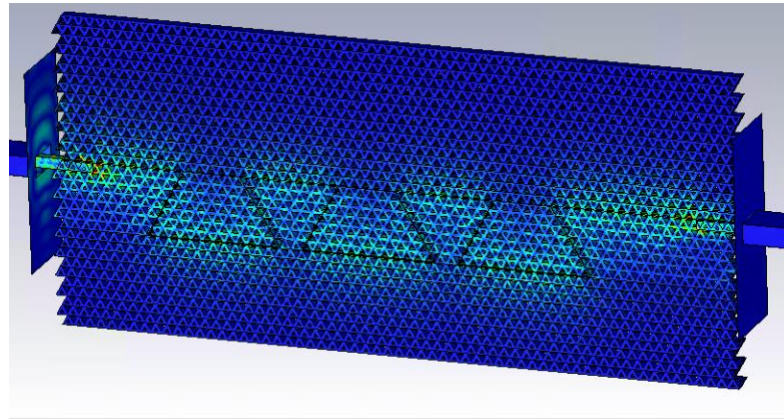


Figure 4. 24 VPC Bended Waveguide E-field

The graph below plots the S_{21} parameter of the VPC with the same length, one without bending and the other with bending. It can be seen that the S_{21} graph almost overlaps with each other, indicating a low bending loss. The difference between these curves will give us the bending loss. The loss per bending can then be calculated by dividing the difference between these curves with the number of bend, which gives us a value of 0.015dB/bend.

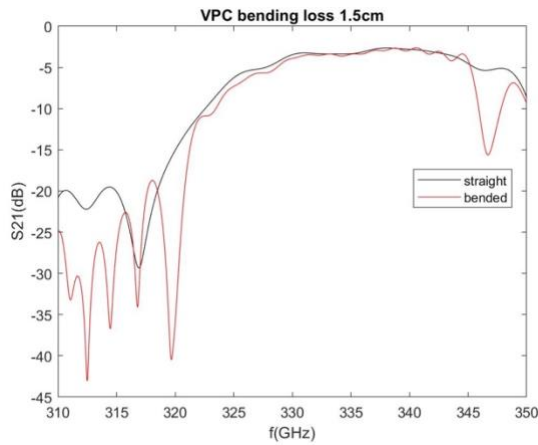


Figure 4. 25 VPC bending loss at 1.5 cm

The robustness against defect will make the device to be immune against any performance degradation induced by imperfection in fabrication or by environmental changes. This will create a defect-insensitive device that will increase the reliability of the device.

Chapter 5 Terahertz Communication Experiment

5.1 Experimental Setup

The goal of this experiment is to demonstrate the potential of photonic crystal as a Terahertz integrated platform that can support high data rate communication system. Terahertz link shall be developed and demonstrated to transmit uncompressed high-definition (HD) video over a photonic crystal waveguide channel. The setup of the experiment is shown in the following figure.

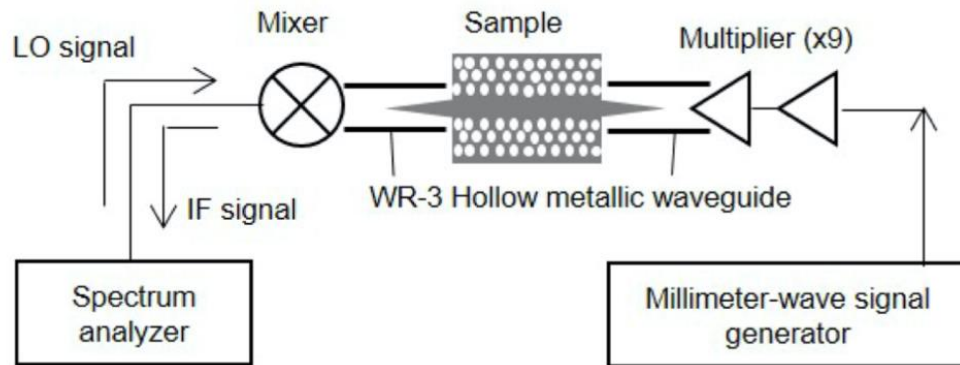


Figure 5. 1 Experimental setup

The experimental setup displayed above is the Terahertz spectroscopic system that is used to measure the transmittance of photonic crystal waveguide (S_{21}). The system employs a continuous wave electronic source comprising of the millimeter-wave (mm-wave) signal generator and multiplier.

The mm-wave signal generator is used to produce a continuous mm-wave in the frequency of tens of GHz. The frequency multiplier is then used to up-convert the frequency produced by mm-wave signal generator to our desired operating frequency range (~300 GHz). After that, WR-3 hollow metallic waveguide is used to couple the

wave from frequency multiplier output to the tapered feed. The position of photonic crystal waveguide and the hollow metallic waveguide shall be adjusted carefully by a micromechanical positioner to ensure optimal coupling.

The output from the photonic crystal waveguide will then be channeled to mixer through another tapered feed and hollow metallic waveguide. The mixer will down-convert the signal into an intermediate frequency (IF) range so that it may be processed by the baseband detector, in our case will be the receiver of the HD video data. The spectrum analyzer is used to generate local oscillator signal that will be mixed with the received output from the photonic crystal waveguide to down-convert the output signal. Before doing the measurement of transmittance, the equipment must be calibrated by measuring transmission between two WR-3 waveguides and without the photonic crystal waveguide.

The actual experimental setup shall look similar to the following photograph taken from [45].

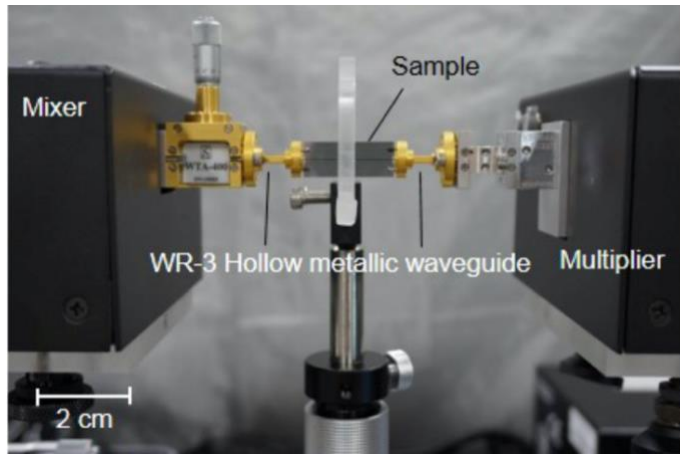


Figure 5. 2 Photograph of the real experimental setup taken from [45]

5.2 Detail of the Experimental Equipment

A more detailed block diagram displaying the experimental setup is shown in the following figure. Most of the equipment were purchased from Virginia Diodes (VDi), a company specializing in manufacturing Terahertz device. Other equipment is purchased from Keysight Technologies.

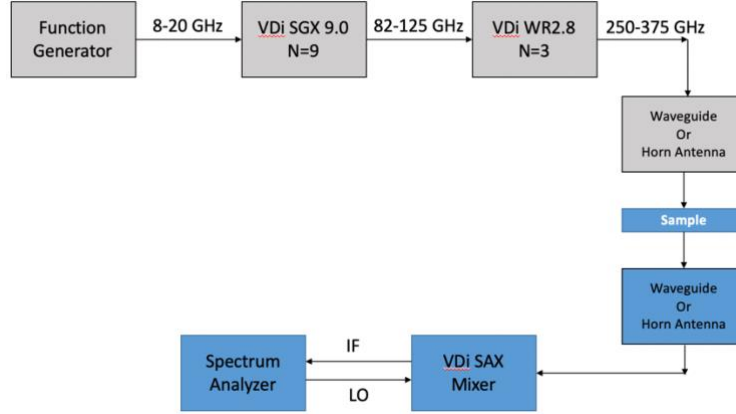


Figure 5. 3 Detailed block diagram

Each of the equipment that has been purchased or is available in the lab will be discussed in the following discussion.

5.2.1 Function Generator

8-20 GHz VDi Synthesizer[70] is shown in the following figure. The device is able to produce signal with frequency in the range of 8-20 GHz. The frequency can be controlled by computer through USB connection with the provided software.



Figure 5. 4 8-20 GHz VDi Synthesizer

5.2.2 Multiplier

The multiplier[71] is composed of two blocks: the nine-fold VDi SGX (signal generator extension) 9.0 multiplier and the three-fold VDi WR2.8 multiplier.

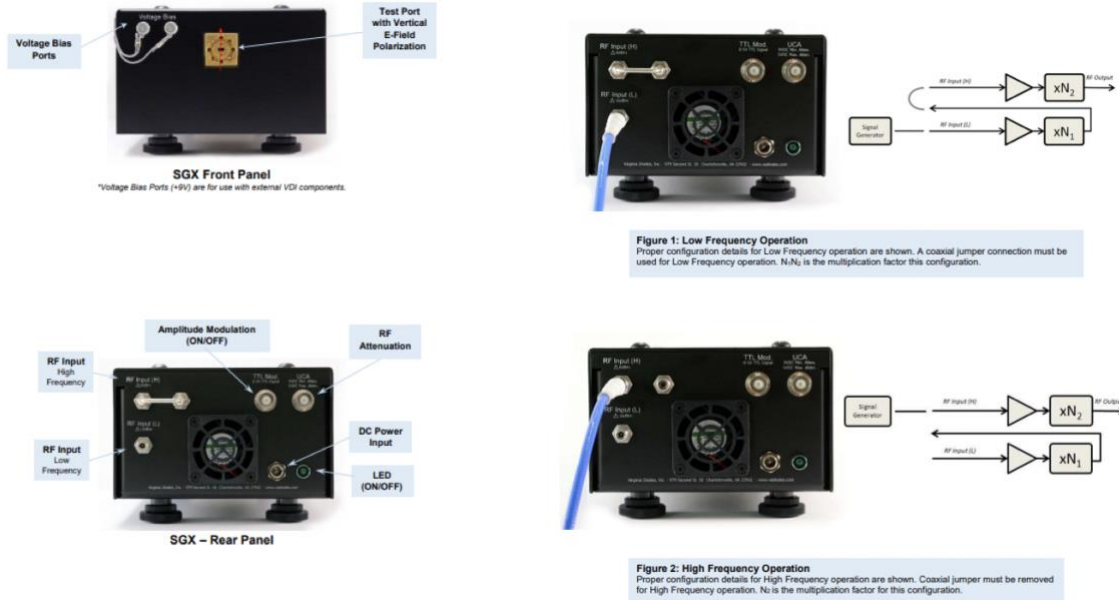


Figure 5.5 Typical configuration of WR9.0SGX



Figure 5.6 WR2.8 Frequency multiplier

The WR9.0SGX is capable of producing wave with frequency in the range of 170-1,100 GHz by tailoring it with the appropriate multiplier as shown in the following figure. The WR9.0AMC device alone is capable of producing frequency in range of 82.5-125 GHz. WR2.8 multiplier that is capable of providing frequency multiplier by threefold will convert this frequency to the range of 250-375 GHz, which is in our desired operating frequency region.

To give a multiplier factor of nine, the WR9.0SGX must be operated with low-frequency input mode. The low-frequency input of WR9.0SGX ranges from 9-14 GHz, which is in the range of 8-20 GHz VDi frequency synthesizer's output frequency.

Moreover, the impedance and power level of these blocks are compatible to each other. By multiplying with a factor of nine, the output will be in the range of 81-126 GHz and it tallies with the specification stated in the datasheet.

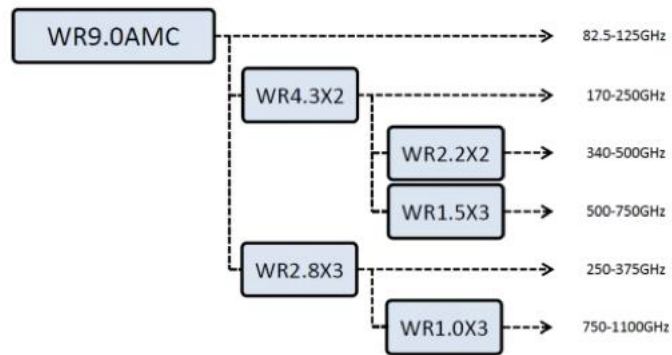


Figure 5. 7 Frequency multiplier of WR9.0SGX

5.2.3 Hollow Rectangular Waveguide

WR-3 waveguide has been purchased as the hollow rectangular waveguide that will couple the signal from the electronic source or receiver to the photonic crystal sample. The waveguide has a dimension of around 864 μm x 432 μm . The lower cut-off frequency that can be supported inside the waveguide is 173.5 GHz, with the recommended operating frequency in range of 220-330 GHz.



Figure 5. 8 WR-3 Waveguide

5.2.4 Mixer and Spectrum Analyzer

VDi SAX (spectrum analyzer extension)[72] Mixer is used to down-convert the signal. It will receive an input from the spectrum analyzer that will produce the local oscillator frequency. This frequency will be mixed with the output of photonic crystal waveguide to down-convert the signal.



Figure 5. 9 VDi SAX

Chapter 6 Conclusions and Future Work

6.1 Conclusions

The integrated photonic devices based on photonic crystal structure has been designed. This new platform of integrated Terahertz system will eventually pave the way to the novel 6G communication system by enabling fast, huge and reliable data transfer.

All the important building blocks needed to develop the complete integrated Terahertz system has been designed. First, photonic crystal waveguide has been designed and has achieved an excellent propagation loss of 0.29 dB/cm with a bandwidth of 23 GHz. The propagation loss is two orders lower than the typical metallic waveguide that is working in Terahertz spectrum (\sim 10 dB/cm). The photonic crystal waveguide will be able to transmit information from one point to the other, taking a role similar to wire in the ordinary integrated circuit.

Second, photonic crystal transmitter has been designed by integrating a Dielectric Resonator Antenna (DRA) at the end of the photonic crystal waveguide. The photonic crystal transmitter is able to operate with a wide bandwidth of 18 GHz and excellent near-field directivity as can be seen in the near-field plot on fig. 3.22. The photonic crystal transmitter will enable inter-chip communication that will improve the modularity and scalability of the design, thus leveraging the usefulness of the device.

Third, photonic crystal narrow-band filter has been designed by creating a neighboring point defects as a resonant cavity. The photonic crystal narrow-band filter has achieved a high Q-factor of 96.62 that will improve the stability of the filter. This narrow-band filter will enable more application, such as to do frequency multiplexing in order to transmit or receive signal. This is very important especially in processing the data transmitted or received. The high Q-factor will allow the device to pick a small range of frequency and thus eliminate possible noise caused by other unintended

frequencies picked.

Fourth, photonic crystal bending has been designed by creating a 60° bended defect with capsule-shaped defect to improve the bandwidth. The photonic crystal bending is able to operate in wide bandwidth of 12 GHz. The design of bending will enable routing of signal that will improve the compactness of the design. However, we have observed that the photonic crystal design is sensitive to bending shape and might be degraded due to the manufacturing defect. This issue will be resolved with the design of topological photonic crystal.

Fifth, the diplexer that is built on the basic building block of waveguide, filter and bending is designed to showcase the powerful application of these basic building block designed earlier. The diplexer is able to operate as a broadband device with fractional bandwidth of 1.8%, higher than the typical coupler in Terahertz regime that can only achieve 0.25% fractional bandwidth. The diplexer has a high cross port isolation of -40 dB.

Furthermore, it has been verified that the photonic crystal devices have a negligible absorption loss when the resistivity is above $20 \text{ } k\Omega \cdot \text{cm}$. This is easily obtained with the current fabrication technologies and can be acquired with low cost. Thus, the photonic crystal based Terahertz system has a big advantage as compared with the metal counterpart that suffers high absorption loss in Terahertz regime. Furthermore, the compact structure and relatively simpler design makes photonic crystal based Terahertz system to be preferred as compared with the bulky and complex optical platform. Therefore, this justifies the approach in designing the novel integrated Terahertz system based on photonic crystal structure that will enable a compact, low-cost, and high-speed device design.

Topological counterpart of photonic crystal waveguide has also been designed based on the valley-hall photonic crystal structure. The topological photonic crystal waveguide has achieved a significantly lower propagation loss of 0.05 dB/cm and bending loss of 0.05 dB/bend, proving it to be robust against reflection loss. This will make the system to be insensitive against defect. Furthermore, the robustness against defect will increase the reliability of signal transfer that is very crucial in the advanced

technological application, such as the autonomous vehicle that needs to work with a very high precision to ensure safe and proper operation.

Miniaturized active sources and detector has also been designed to complete the integrated Terahertz system design. The resonant tunneling diode (RTD) is designed as a source or detector that can be integrated directly inside the device with compatible structure. The RTD can work with a bandwidth of 5.61 GHz for the integration with topological photonic crystal waveguide.

Lastly, the possible experimental scheme has been presented to show the practical way in performing the communication experiment.

The designed devices will become the building block of the novel and robust integrated Terahertz system. The devices are designed in lower Terahertz regime and is able to provide bandwidth of a few up to tens of GHz, which will enable data transfer rate in the order of Gbit/s.

The device is deliberately designed in the lower Terahertz regime as the application is meant to be developed for on-chip communication and to use the atmospheric transmission window present in the lower Terahertz spectrum. However, the designed device can be easily scalable to a higher operating frequency due to the scale invariant properties of Maxwell equations. A different operating frequency can be achieved by scaling the original operating frequency linearly. To scale the operating frequency, we just need to scale the dimension linearly to achieve the desired operating frequency. In other words, the solution of the problem at a particular scale of length determines the solution at all other scales. This gives a powerful application to our design as it can be scaled up to higher Terahertz operating frequency to enable Tbit/s data transfer rate that is required for the future 6G communication system.

Eventually, the integrated Terahertz system based on photonic crystal structure will enable a new wireless communication platform that can support ultra-fast data transfer rate, reliable data transfer, compact design and low development cost. This will open up a plethora of application in the future technological advancement, such as for the development of Artificial Intelligence (AI), Virtual Reality (VR), Autonomous Vehicle, Smart City, Medical and Security application, and many other more.

6.2 Recommendation in Future Work

There are some few recommendations of future work that may be done in continuation with this project. First, the experimental measurement can be performed on the fabricated device to verify that it can practically function well. The experimental measurement can first be demonstrated on a High-Definition (HD) video transmission to verify a proper operating device. Thereafter, a device characterization shall be done on the fabricated device. Some important FOM that can be characterized would be the propagation loss, bending loss and bandwidth.

Furthermore, the Terahertz modulation scheme may also be developed in future work. Having a wide bandwidth is a necessary condition but not sufficient to ensure a high data rate. A proper and efficient modulation scheme must be developed in order to complement the broadband device that has been designed. Some possible modulation scheme may be found in [73]. For instance, electrical or optical modulator based on quantum well was proposed to modulate signal in Terahertz frequency spectrum. Another potential Terahertz modulator would be the uni-travelling-carrier photodiode[74] (UTC-PD) that will modulate the light shone on its surface and convert the modulated light into electrical signal. The UTC-PD has the advantage of being compact and has a low-cost development for commercial application.

Another possible future work would be to design a more compact and interconnected device like the diplexer designed earlier. An interesting future work would be to design an all-optical gate based on photonic crystal structure. To design this, we would need to design the universal NAND and NOR gate based on photonic crystal structure, such as the one presented in [75]. By designing these two universal gates, we can build all the logical operation that we want and we can have an all-optical gate based on photonic crystal structure. The NAND and NOR gate can be built entirely using the design of cavity, waveguide and bending. Thus, the systematic work laid in this project would provide a solid foundation on designing the more compact NAND and NOR gate.

A more specific future work would be to design the topological counterpart of the

photonic crystal device, such as the topological photonic crystal transmitter[36] and filter[76]. The design of the topological photonic crystal device may utilize the robust uni-directional transmission property to harness interesting structure. For example, directionality in TPC transmitter may be designed by slashing the end of the TPC waveguide at particular angle such as the one presented in [36]. The free-space transmission may be achieved without the design of antenna and it will consequently reduce the complexity and improve the compactness of the device.

Furthermore, an improved signal feed may be designed to improve the coupling between the feed and the topological photonic crystal device for better signal transmission. From the result that we obtain earlier, we can see that there is still a relatively high coupling loss of 5.5 dB in TPC as compared with the PC coupling loss that is of value 1.4 dB. A suitable adiabatic tapered feed may be designed for TPC to improve on the impedance matching. The location of tapered feed with respect to the waveguide channel should also be optimized to make an efficient coupling for better signal transmission.

Summary of Accomplishment and Contribution

The main accomplishment and the contribution that the author has done can be summarized as following:

- Design, optimize and fabricate the photonic crystal waveguide based on 2D triangular photonic crystal slab, photonic crystal transmitter using dielectric resonator antenna and topological photonic crystal waveguide based on valley-hall topological photonic crystal structure. The devices are fabricated by A*STAR IME and will be used to experimentally verify the functionalities of the proposed device.
- Design and optimize the miniaturized source and detector based on resonant tunneling diode for topological photonic crystal application. The design is to be fabricated and passed to the future team that will be handling the experimental part.
- Provide a comprehensive systematic study and design on the basic building block of the integrated Terahertz system based on photonic crystal structure.
- Collaborate with the experimental team in order to sync the theoretical and simulation study and the experimental scheme developed.

Reflection on Learning Outcome Attainment

This final year project has become a truly cherished learning opportunities that I had. During my learning journey in FYP, I have achieved several learning outcomes:

Engineering Knowledge

I have acquired a lot of engineering knowledge, particularly on how to bring the theoretical understanding into a real-life and practical application. This FYP is a good reflection on how we study the nature and how we can harness powerful application by understanding the way nature behaves. I have learnt to comprehend the theoretical framework on how the system work and how to apply it in engineering context where things are not as perfect as the ideal condition considered in developing the theoretical framework.

Problem Analysis, Investigation and Development of Solution

I have also learnt to sharpen my problem-solving skill by analyzing and finding out the main issue/problem, investigating it, and developing the optimal solution. I have used this problem-solving skill to understand the new material and concept in my FYP that I have not encountered before.

Modern Tool Usage

I have also learnt to utilize the commercial software to aid me in designing the device. I particularly have learnt to use the software CST Microwave Studio and COMSOL Multiphysics in order to design the device. Furthermore, I have also put my knowledge in MATLAB into real practice where I visualize and analyze my data using MATLAB. This helps me to learn how to present data effectively to convey the result.

Individual, Team Work and Communication

I have also obtained competency in learning to work independently as individual and also to work collaboratively in team. As an individual, I learnt to deliver my assigned task on a timely manner where I need to gather information from many resources and integrate them to come out with something that can be used to solve the problem. At the same time, I also need to work in team to integrate the work and share with each other on the new findings. In working as a team, I also learn to communicate properly.

Lifelong learning

My experience in FYP has ignited a spirit of lifelong pursuit of knowledge. As the material used is not taught in our courses, I have learnt to do self-study on the field that I am interested of. The self-initiated study has brought personal fulfillment and development that lead to more interest, curiosity and motivation for me in learning even more new things.

References

- [1] Y. Zhao, "A Survey of 6G Wireless Communications: Emerging Technologies," 2020.
- [2] S. Borkar, "Design challenges of technology scaling," *IEEE Micro*, vol. 19, no. 4, pp. 23-29, 1999, doi: 10.1109/40.782564.
- [3] M. F. O. H. a. N. F. F. A. Salah Obayya, *Computational Liquid Crystal Photonics: Fundamentals, Modelling and Applications*. John Wiley & Sons, Ltd, 2016.
- [4] E. Yablonovitch, "Inhibited spontaneous emission in solid-state physics and electronics," *Physical review letters*, vol. 58, no. 20, p. 2059, 1987.
- [5] S. John, "Strong localization of photons in certain disordered dielectric superlattices," *Physical review letters*, vol. 58, no. 2486, 1987.
- [6] J. W. Strutt, "On the reflection of light from a regularly stratified medium," *Royal Society*, vol. 93, no. 655, 9 October 1917 1917.
- [7] M. 6.635, "Study of EM waves in Periodic Structures ". [Online]. Available: https://ocw.mit.edu/courses/electrical-engineering-and-computer-science/6-635-advanced-electromagnetism-spring-2003/lecture-notes/Mar19_1.pdf
- [8] C. C. Shouyuan Shi, and Dennis W. Prather, "Plane-wave expansion method for calculating band structure of photonic crystal slabs with perfectly matched layers," *Optical Society America*, vol. 21, no. 9, pp. 1769-1775, 2004, doi: <https://doi.org/10.1364/JOSAA.21.001769>.
- [9] A. J. Danner. "An introduction to the plane wave expansion method for calculating photonic crystal band diagrams." <https://www.ece.nus.edu.sg/stfpage/eleadj/planewave.htm> (accessed).
- [10] S. G. J. John D. Joannopoulos, Joshua N. Winn, Robert D. Meade, *Photonic Crystals: Molding the Flow of Light*, second ed. Princeton University Press, 2007.
- [11] Wikipedia. "Fermat's principle." https://en.wikipedia.org/wiki/Fermat%27s_principle (accessed).
- [12] Wikipedia. "Taylor series." https://en.wikipedia.org/wiki/Taylor_series (accessed).
- [13] Wikipedia. "Snell's law." https://en.wikipedia.org/wiki/Snell%27s_law (accessed).
- [14] M. M. V. Savona, "Automated optimization of photonic crystal slab cavities," *Nature*, 2014, doi: 10.1038/srep05124.
- [15] S. F. Steven G. Johnson, Pierre R. Villeneuve, and J. D. Joannopoulos, "Guide modes in photonic crystal slabs," *Physical review. B, Condensed matter*, vol. 60, no. 8, pp. 5751-5758, 1999, doi: 10.1103/PhysRevB.60.5751.
- [16] M. S. Exchange. "How can a mug and a torus be equivalent if the mug is chiral?" <https://math.stackexchange.com/questions/2258389/how-can-a-mug-and-a-torus-be-equivalent-if-the-mug-is-chiral> (accessed).
- [17] Wikipedia. "Euler Characteristics." https://en.wikipedia.org/wiki/Euler_characteristic (accessed).
- [18] Wikipedia. "Topology." <https://en.wikipedia.org/wiki/Topology> (accessed).

- [19] J. A. D. O. R. Seiler, "A Topological Look at the Quantum Hall Effect," *Physics Today*, vol. 56, no. 8, p. 38doi: 10.1063/1.1611351.
- [20] D. S. Simon, *Tying Light in Knots: Applying topology to optics*. 1210 Fifth Avenue, Suite 250, San Rafael, CA, 94901, USA: Morgan & Claypool, 2018.
- [21] H. v. B. Jens von Bergmann, "Foucault pendulum through basic geometry," *American Journal of Physics*, vol. 75, no. 10, 888, 2007, doi: <https://doi.org/10.1119/1.2757623>.
- [22] H. M. P. Tomoki Ozawa, Alberto Amo, Nathan Goldman, Mohammad Hafezi, Ling Lu, Mikael C. Rechtsman, David Schuster, Jonathan Simon, Oded Zilberberg, and Iacopo Carusotto, "Topological Photonics," *Reviews of Modern Physics*, vol. 91, no. 015006, 2019, doi: <https://doi.org/10.1103/RevModPhys.91.015006>.
- [23] S.-C. Z. Xiao-Liang Qi, "The quantum spin Hall effect and topological insulators," *Physics Today*, vol. 63, no. 33, 2010, doi: <https://doi.org/10.1063/1.3293411>.
- [24] "Hall Effect." <http://hyperphysics.phy-astr.gsu.edu/hbase/magnetic/Hall.html> (accessed).
- [25] D. Tong, *The Quantum Hall Effect*, 2016.
- [26] Wikipedia. "Graphene." <https://en.wikipedia.org/wiki/Graphene> (accessed).
- [27] Wikipedia. "Lenz's law." https://en.wikipedia.org/wiki/Lenz%27s_law (accessed).
- [28] T. Delft. "Where do the pumped electrons come from and go to?" https://topocondmat.org/w3_pump_QHE/QHEedgestates.html (accessed).
- [29] Y. Hatsugai, "Chern number and edge states in the integer quantum Hall effect," *Physical review letters*, vol. 71, pp. 3697-3700, 1993.
- [30] S. R. a. F. D. M. Haldane, "Analogs of quantum-Hall-effect edge states in photonic crystals," *Physical review letters A*, vol. 78, no. 033834, 2008, doi: <https://doi.org/10.1103/PhysRevA.78.033834>.
- [31] Y. C. Zheng Wang, J. D. Joannopoulos & Marin Soljačić "Observation of unidirectional backscattering-immune topological electromagnetic states," *Nature*, vol. 461, pp. 772-775, 2009, doi: 10.1038/nature08293.
- [32] R. Y. Hongming Weng, Xiao Hu, Xi Dai, Zhong Fang, "Quantum Anomalous Hall Effect and Related Topological Electronic States," *Advances in Physics*, 2015, doi: 10.1080/00018732.2015.1068524.
- [33] Y. H. Takahiro Fukui, Hiroshi Suzuki, "Chern numbers in discretized Brillouin zone: Efficient method of computing (spin) Hall conductances," *Physical society japan*, vol. 74, pp. 1674-1677, 2005, doi: 10.1143/JPSJ.74.1674.
- [34] J. D. J. Ling Lu, Marin Soljačić, "Topological photonics," *Nature Photonics*, vol. 8, 2014, doi: 10.1038/NPHOTON.2014.248.
- [35] S. R. Andreas P. Schnyder, Akira Furusaki, Andreas W. W. Ludwig, "Classification of topological insulators and superconductors in three spatial dimensions.,," *physical review letters B*, vol. 78, no. 195125, 2008, doi: 10.1103/PhysRevB.78.195125.
- [36] T. M. a. G. Shvets, "All-Si valley-Hall photonic topological insulator," *New Journal of Physics*, vol. 18, no. 025012, 2016, doi: 10.1088/1367-2630/18/2/025012.

- [37] X. X. Jingwen Ma, and Xiankai Sun, "Supporting Information for "Topological photonic integrated circuits based on valley kink states"," *Laser and Photonics Review*, 2019, doi: <https://doi.org/10.1002/lpor.201900087>.
- [38] C. Hoffman, "What Is 5G, and How Fast Will It Be?," 2020. [Online]. Available: <https://www.howtogeek.com/340002/what-is-5g-and-how-fast-will-it-be/>.
- [39] Wikipedia. "Radio frequency." https://en.wikipedia.org/wiki/Radio_frequency (accessed).
- [40] N. B. Saim Ghafoor, Mubashir Husain Rehmani, Alan Davy, "MAC Protocols for Terahertz Communication: A Comprehensive Survey," *IEEE Communication Surveys and Tutorials*, 2019.
- [41] M. F. DANIEL HEADLAND, AND TADAO NAGATSUMA, "Half-Maxwell fisheye lens with photonic crystal waveguide for the integration of terahertz optics," *Optics Express*, vol. 28, no. 2, 2020, doi: 10.1364/OE.381809.
- [42] B. O. C.-Y. Kao, "EXTREMAL SPECTRAL GAPS FOR PERIODIC SCHROEDINGER OPERATORS," *ESAIM Control Optimisation and Calculus of Variations*, 2018, doi: 10.1051/cocv/2018029.
- [43] STMicroelectronics. "Waveguide Sizes." <https://www.everythingrf.com/tech-resources/waveguides-sizes> (accessed).
- [44] P. M. R. P. A. P. M. Jasminea, "Coupling Enhancement of Waveguide fed Dielectric Resonator Antenna using Tapered Section of Waveguide," presented at the International Conference on Information and Communication Technologie, 2015.
- [45] M. F. Kazuisao Tsuruda, and Tadao Nagatsuma, "Extremely low-loss terahertz waveguide based on silicon photonic-crystal slab," *Optical Society America*, vol. 23, no. 25, 2015, doi: 10.1364/OE.23.031977.
- [46] R. Y. WITHAWAT WITHAYACHUMNANKUL, CHRISTOPHE FUMEUX, MASAYUKI FUJITA, AND TADAO NAGATSUMA2, "All-dielectric integration of dielectric resonator antenna and photonic crystal waveguide," *Optics Express*, vol. 25, no. 13, 2017.
- [47] R. Y. Withawat Withayachumnankul , Masayuki Fujita, and Tadao Nagatsuma, "All-dielectric rod antenna array for terahertz communications," *APL PHOTONICS*, 2018, doi: <https://doi.org/10.1063/1.5023787>.
- [48] G. A. T. Warren L. Stutzman, *Antenna Theory and Design*. John Wiley & Sons, Inc.
- [49] K. W. L. K. M. Luk, *Dielectric Resonator Antennas*. RESEARCH STUDIES PRESS LTD., 2003.
- [50] T. A. D. Alexandre Perron, and Abdel-Razik Sebak, "High-Gain Hybrid Dielectric Resonator Antenna for Millimeter-Wave Applications: Design and Implementation," *IEEE TRANSACTIONS ON ANTENNAS AND PROPAGATION*, vol. 57, no. 10, pp. 2882-2892, 2009.
- [51] M. F. a. M. A. Hadjira Badaoui, "Photonic-Crystal Band-pass Resonant Filters Design Using the Two-dimensional FDTD Method," *International Journal of Computer Science Issues*, vol. 8, no. 3, pp. 127-132, 2011.
- [52] Wikipedia. "Local Oscillator." https://en.wikipedia.org/wiki/Local_oscillator (accessed).

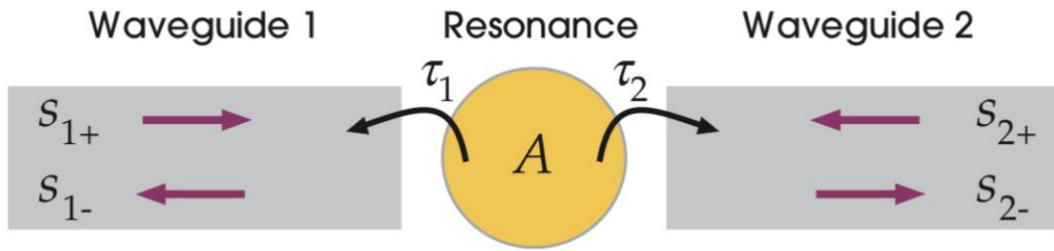
- [53] E. L. Mario Agio, and Costas M. Soukoulis, "Impurity modes in a two-dimensional photonic crystal: coupling efficiency and Q factor," *Optical Society America B*, vol. 17, no. 12, pp. 2037-2042, 2000.
- [54] M. F. Masahiro Yata, * and Tadao Nagatsuma, "Photonic-crystal diplexers for terahertz-wave applications," *Optical Society of America*, vol. 24, no. 7, pp. 7835-7849, 2017, doi: <https://doi.org/10.1364/OE.24.007835>.
- [55] N. R. Erickson, "High performance dual directional couplers for near-mm wavelengths," *IEEE Microwave Wireless Component Letter*; vol. 11, no. 5, pp. 205-207, 2011.
- [56] N. Y. J. Sugisaka, M. Okano, K. Komori, and M. Itoh, "Short photonic-crystal directional coupling optical switch of extended optical bandwidth using flat dispersion," *Japan Journal of Applied Physics*, vol. 50, 2011.
- [57] F. D. M. H. a. S. Raghu, "Possible Realization of Directional Optical Waveguides in Photonic Crystals with Broken Time-Reversal Symmetry," *Physical review letters*, vol. 100, no. 013904, 2008, doi: <https://doi.org/10.1103/PhysRevLett.100.013904>.
- [58] W. W. Mikhail I. Shalaev, Alexander Tsukernik, Yun Xu, and Natalia M. Litchinitser, "Robust topologically protected transport in photonic crystals at telecommunication wavelengths," *Nature Nanotechnolog*, vol. 14, 2019, doi: 10.1038/s41565-018-0297-6.
- [59] H. X. Fei Gao, Zhaoju Yang, Kueifu Lai, Yang Yu, Xiao Lin, Yidong Chong, Gennady Shvets & Baile Zhang "Topologically protected refraction of robust kink states in valley photonic crystals," *Nature*, vol. 14, pp. 140-144, 2017, doi: 10.1038/nphys4304.
- [60] Y. Y. Yihao Yang, Xiongbin Yu, Prakash Pitchappa, Baile Zhang, Masayuki Fujita, Tadao Nagatsuma, and Ranjan Singh, "Terahertz topological photonics for on-chip communication," *Applied Physics*, 2019. [Online]. Available: <https://arxiv.org/abs/1904.04213>.
- [61] K. S. T. Fukui, T. Fujiwara, S. Fujimoto, "Bulk-edge correspondence for Chern topological phases: A viewpoint from a generalized index theorem," *Journal of Physics Society Japan*, vol. 81, no. 114602, 2012, doi: 10.1143/JPSJ.81.114602.
- [62] O. L. notes, "Some general points about bandstructure." [Online]. Available: https://www2.physics.ox.ac.uk/sites/default/files/BandMT_05.pdf
- [63] F. O. C. Networks. "The Advantages and Disadvantages of Multimode Fiber and Single Mode Fiber Cable." <http://www.fiber-optic-components.com/the-advantages-and-disadvantages-of-multimode-and-single-mode-fiber.html> (accessed).
- [64] C. Q. Jiuyang Lu, Liping Ye, Xiying Fan, Manzhu Ke, Fan Zhang, Zhengyou Liu, "Observation of topological valley transport of sound in sonic crystals," *Nature Physics*, vol. 13, no. 369, 2017, doi: 10.1038/nphys3999.
- [65] H.-Y. T. Trisha L. Andrew, Rajesh Menon, "Confining Light to Deep Subwavelength Dimensions to Enable Optical Nanopatterning," 2009, vol. 324.
- [66] K. H. M. Takeru, S. Safumi, and A. Masahiro, "Oscillation up to 1.92 THz in resonant tunneling diode by reduced conduction loss," *Applied Physics Express*, vol. 9, no. 2, 2016.
- [67] M. F. Tadao Nagatsuma, Ai Kaku, Daiki Tsuji, Shunsuke Nakai,Kazuisao

- Tsuruda, Toshikazu Mukai, "Terahertz Wireless Communications Using Resonant Tunneling Diodes as Transmitters and Receivers," presented at the Third International Conference on Telecommunications and Remote Sensing, 2014.
- [68] S. B. a. J. L. V. Caiyu Wang, "Resonant Tunneling Diodes for Feeding Antenna-Structures for Terahertz Source Applications," in *IEEE International Symposium on Antennas and Propagation & USNC/URSI National Radio Science Meeting*, 2017, doi: 10.1109/APUSNCURSINRSM.2017.8072915.
- [69] R. M.-A. M. Riaziat, and I. J. Feng, "Propagation modes and dispersion characteristics of coplanar waveguides," *IEEE Transactions on microwave theory*, vol. 38, no. 3, pp. 242-251, 1990.
- [70] VDi, "8-20GHz VDi Synthesizer." [Online]. Available: <https://www.vadiodes.com/en/products/frequency-synthesizer-and-frequency-counter>.
- [71] VDi, "Mini Signal Generator Extension Module (SGX) - VDI Model: WR9.0SGX-M." [Online]. Available: <https://vadiodes.com/index.php/en/products/signal-generator?id=929>.
- [72] VDi. "Spectrum Analyzer Extension Modules." <https://www.vadiodes.com/en/products/spectrum-analyzer> (accessed).
- [73] Z. X. G. Z. T. Ma, Z. Y. Fan, J. Liu, and H. D. Chen, "Modulators for Terahertz Communication: The Current State of the Art," *Science Partner Journal*, no. 6482975, 2019, doi: 10.34133/2019/6482975.
- [74] H. S. Ahmad Wasfi Mohammad, Chin-Pang Liu, Chris Graham, Michele Natrella, Alwyn J. Seeds, and Cyril C. Renaud, "60-GHz Transmission Link Using Uni-Traveling Carrier Photodiodes at the Transmitter and the Receiver," *JOURNAL OF LIGHTWAVE TECHNOLOGY*, vol. 36, no. 19, pp. 4507-4513, 2018, doi: 10.1109/JLT.2018.2849938.
- [75] V. J. U. F. K. Esakki Muthu, S. Sorna Deepa, A. Sivanantha Raja and S. Robinson, "Design and Analysis of 3-Input NAND/NOR/XNOR Gate Based on 2D Photonic Crystals," *Journal of Optical Communications* 2019, doi: <https://doi.org/10.1515/joc-2018-0210>
- [76] J. M. X. X. X. Sun, "Topological Photonics: Topological Photonic Integrated Circuits Based on Valley Kink State," *Laser and Photonics Review*, 2019, doi: <https://doi.org/10.1002/lpor.201970049>.
- [77] R. G. Littlejohn, "Time Reversal," Berkeley, 2019.
- [78] L. M. Lee, *PH3101 Quantum Mechanics II lecture notes part 1 appendix C*, 2019.

Appendix A: Derivation of Temporal Coupled Mode Theory

Formalism

This theory is in analogy to time-dependent perturbation theory widely used in quantum mechanics. Consider a system composed of waveguides and resonant cavity as shown in the figure below. The waveguide will carry the propagating modes whereas the resonant cavity will confine the localized modes. The system is general enough to cater certain class of devices, which include all the devices designed in this project (filter, diplexer, and bending).



Temporal coupled mode theory framework

Suppose that the field amplitude inside the cavity is proportional to some variable A such that the energy can be expressed as $|A|^2$. The field resonates at particular frequency ω_0 . S_{l+} are fields incoming to resonant cavity from waveguide l and S_{l-} are fields outgoing from resonant cavity to waveguide l , where $l = 1, 2$ correspond to waveguide 1 and 2. The incoming and outgoing power can then be expressed as $|S_{l+}|^2$ and $|S_{l-}|^2$.

The mode inside the cavity will decay exponentially with some lifetime τ . The exponential decay may be justified by the fact that the Poynting vector that indicates the energy transfer per unit area per unit time is proportional to the energy.

$$S = \frac{1}{area} \frac{d|A|^2}{dt} = \frac{Re(\mathbf{E}^* \times \mathbf{H})}{2} \sim |A|^2$$

The exponential relation is obtained by assuming weak coupling. In other words,

the time it took for the energy to decay is much larger than one period such that $|A|^2$ can be considered as constant over a period. Mathematically, the condition is expressed as below:

$$\tau \gg \frac{2\pi}{\omega_0} \Rightarrow Q = \frac{\omega_0 \tau}{2} \gg \pi$$

The decay lifetime must take into account all possible loss mechanisms.

$$\frac{1}{\tau} = \frac{1}{\tau_1} + \frac{1}{\tau_2}$$

It is found that the dynamic equation of the energy satisfies the following differential equation:

$$\frac{dA}{dt} = -i\omega_0 A - \frac{A}{\tau}$$

By which the solution is expressed as below:

$$A = A(0) e^{-i\omega_0 t - \frac{t}{\tau}}$$

Now, we should consider the energy transfer from or to the waveguide. The input energy S_{l+} may be coupled to the waveguide or be reflected as S_{l-} . The energy decaying out from resonant cavity will also add up to S_{l-} . This can be expressed quantitatively as follow:

$$\begin{aligned} \frac{dA}{dt} &= -i\omega_0 A - \frac{A}{\tau_1} - \frac{A}{\tau_2} + \alpha_1 S_{l+} + \alpha_2 S_{l-} \\ S_{l-} &= \beta_l S_{l+} + \gamma_l A \end{aligned}$$

where α_l, β_l and γ_l are proportionality constants. Both α_l and γ_l represent the coupling strength between the cavity and waveguide and β_l is the reflection coefficient. We will express the constants in terms of ω_0 and τ .

The constant γ_l can be determined from the conservation of energy. To determine γ_1 of waveguide 1, consider the case when $\tau_2 \rightarrow \infty$, implying that the resonant cavity is decoupled from waveguide 2. Assume there is no input energy from the waveguide to cavity $S_{l+} = S_{l-} = 0$. The cavity energy can only decay to waveguide 1, or mathematically is expressed as:

$$-\frac{d|A|^2}{dt} = |S_{l-}|^2 \Rightarrow \frac{2}{\tau_1} |A|^2 = |S_{l-}|^2$$

The imaginary part of the derivative has been ignored because the imaginary part signifies the energy stored inside the resonant cavity. We are interested in computing the energy decaying out from the cavity. Denoting that $|S_{1-}|^2 = |\gamma_1|^2 |A|^2$, we can find the expression for γ_l in general (because we make no special reference to which particular waveguide):

$$\gamma_l = \sqrt{\frac{2}{\tau_l}}$$

Note that we can consider the decay to waveguide 1 and waveguide 2 separately because the coupling is weak. When both τ_1 and τ_2 are finite, τ_2 will affect γ_1 by a higher-order effect that can be neglected.

Meanwhile, α_l and β_l can be derived from the condition of time-reversal symmetry. Time-reversal symmetry implies that[77]:

$$\psi_r(\mathbf{x}, t) = \psi^*(\mathbf{x}, t)$$

where $\psi(\mathbf{x}, t)$ is a time-dependent function. In this case, the function is $A(t)$. That implies,

$$A_r(t) = A(0)e^{-i\omega_0 t + \frac{t}{\tau}}$$

is also a solution that indicates an exponentially growing field. This makes sense because in reversing the time, the energy now flows from the waveguide to the cavity. By reversing the time and adhering to the definition mentioned earlier, we find that

$S_{l+} = \sqrt{\frac{2}{\tau_l}} A$ and $S_{l-} = 0$ give result to $A_r(t)$. Plugging all these value into the equation of S_{l-} , we find that:

$$\beta_l = -1$$

The minus sign indicates a reflection that is in opposite direction to the cavity's inward coupling constant γ_l .

To determine α_1 , we set $\tau_2 \rightarrow \infty$ and plug in all the above values to the differential equation of A . We will obtain:

$$\alpha_l = \sqrt{\frac{2}{\tau_l}} = \gamma_l$$

We can now integrate all the solutions that we derived to obtain the temporal coupled-mode equations for the system specified:

$$\frac{dA}{dt} = -i\omega_0 A - \sum_{l=1}^2 \frac{A}{\tau_l} + \sum_{l=1}^2 \sqrt{\frac{2}{\tau_l}} S_{l+}$$

$$S_{l-} = -S_{l+} + \sqrt{\frac{2}{\tau_l}} A$$

Application to lossless filter

We can apply the temporal-coupled mode formalism to a 2D lossless filter (assumed to have infinite thickness). Waveguide 1 will be the input port, waveguide 2 will be the output port whereas the resonant cavity is used to build the resonant filter. Assume that the input to the filter oscillates at a fixed frequency ω . Because the system is linear, the field at any point must also oscillate at frequency ω . Thus, the field has the following form:

$$A = A(0)e^{-i\omega t}$$

As there is only input from one port, we can set $S_{2+} = 0$. Substituting it to the temporal coupled mode equation and using the definition of transmittance as the ratio between output power to the input power, we will obtain:

$$T(\omega) = \frac{|S_{2-}|^2}{|S_{1+}|^2} = \frac{\frac{4}{\tau_1 \tau_2}}{(\omega - \omega_0)^2 + (\frac{1}{\tau_1} + \frac{1}{\tau_2})^2}$$

By inspection, we can observe that maximum transmission $T(\omega) = 1$ happens when $\tau_1 = \tau_2$ at $\omega = \omega_0$. This implies that the wave from cavity must decay at equal rate to both port. This equality can be ensured by designing symmetric structure.

Using the definition of Q-factor as:

$$Q = \frac{\omega_0 \tau}{2}$$

and assuming symmetric structure, the transmission spectrum can be expressed in a more useful form using Q-factor.

$$T(\omega) = \frac{\frac{1}{4Q^2}}{(\omega - \omega_0)^2 + \frac{1}{4Q^2}}$$

Application to silicon slabs with finite thickness

A 2D PC structure with finite thickness will add a new decay mechanism through radiation to surrounding air. The radiation decay can be treated simply as another output port that is coupled to the cavity. Assuming that weak coupling still hold implies that the loss rate is small enough ($Q_r \gg 1$). This will modify the equation to be:

$$\frac{dA}{dt} = -i\omega_0 A - \frac{A}{\tau_r} - \sum_{l=1}^2 \frac{A}{\tau_l} + \sum_{l=1}^2 \sqrt{\frac{2}{\tau_l}} S_{l+}$$

Solving it in a similar manner, we will obtain the following transmission spectrum:

$$T(\omega) = \frac{\frac{1}{4Q_w^2}}{(\omega - \omega_0)^2 + \frac{1}{4Q^2}}$$

$$\frac{1}{Q} = \frac{1}{Q_w} + \frac{1}{Q_r}$$

where Q_w is Q-factor for the in-plane decay and Q_r is the Q-factor for radiation. The maximum peak happens at:

$$T(\omega_0) = \left(\frac{Q}{Q_w}\right)^2 \approx 1 - \frac{2Q}{Q_r}$$

It can be seen that as $Q_r \gg Q_w$, the transmission coefficient will approach one. This is expected as the wave decays faster to the in-plane PC as compared to the surrounding air. The energy that is not transmitted is partly radiated away to the surrounding and partly reflected due to the presence of radiation loss that breaks the zero-reflection condition of symmetric system. However, this is a second order effect as compared to radiation loss.

The reflection loss can be reduced by designing structure with high Q_r , for example by increasing the thickness of the design. Alternatively, we can also design an adiabatic transition for better impedance matching to reduce reflection loss.

Appendix B: Berry Phase

The derivation presented here has been reproduced from [78] with permission. An understanding of Dirac notation is required.

Consider a general quantum state denoted by $|\psi(t)\rangle$. This quantum state may represent any wave function of a system, such as the Bloch wave in our case. This quantum state has a phase term that eventually contains a very useful information about the system evolution with time, despite being overlooked on general study.

We denote the state modulo the phase (mod 2π) as:

$$|\psi(t)\rangle_{modulo\ phase} \equiv |\phi(t)\rangle$$

$$|\phi(t)\rangle = |\phi(0)\rangle e^{if(t)}$$

where $if(t)$ is the phase acquired by $|\phi(t)\rangle$ after a time t .

We also make the following ansatz:

$$|\psi(t)\rangle = |\phi(t)\rangle e^{if(t)}$$

If Φ is the phase acquired by $|\psi(t)\rangle$ after a full revolution at time $t = T$, we have:

$$|\psi(T)\rangle = |\psi(0)\rangle e^{i\Phi}$$

Due to the cyclic condition, we have:

$$|\phi(T)\rangle = |\phi(0)\rangle$$

We evaluate the state at time $t = T$. From the ansatz that we assume, we obtain:

$$\begin{aligned} |\psi(T)\rangle &= |\phi(T)\rangle e^{if(T)} \\ |\psi(0)\rangle e^{i\Phi} &= |\phi(0)\rangle e^{if(T)} \\ |\phi(0)\rangle e^{if(0)} e^{i\Phi} &= |\phi(0)\rangle e^{if(T)} \\ e^{if(0)} e^{i\Phi} &= e^{if(T)} \\ \therefore \Phi &= f(T) - f(0) \end{aligned}$$

The state $|\psi(t)\rangle$ obeys the Schrödinger equation.

$$H|\psi(t)\rangle = i\hbar \frac{d|\psi(t)\rangle}{dt}$$

where H is the translation in time operator. We substitute the ansatz to the Schrödinger equation and use derivative chain rule to obtain:

$$H|\psi(t)\rangle = i\hbar \left(\frac{d|\phi(t)\rangle}{dt} e^{if(t)} + |\phi(t)\rangle ie^{if(t)} \frac{df(t)}{dt} \right)$$

Multiply the above equation with the bra $\langle\phi(t)|$ and using the orthonormal condition that $\langle\phi(t)|\phi(t)\rangle = 1$, we obtain the following relation:

$$\langle\phi(t)|H|\psi(t)\rangle = i\hbar e^{if(t)} \langle\phi(t)| \frac{d}{dt} |\phi(t)\rangle - \hbar e^{if(t)} \frac{df(t)}{dt}$$

Re-arranging the term, we have:

$$-\frac{df(t)}{dt} = \frac{1}{\hbar} e^{-if(t)} \langle\phi(t)|H|\psi(t)\rangle - i \langle\phi(t)| \frac{d}{dt} |\phi(t)\rangle$$

We know that the complex conjugate of $|\psi(t)\rangle$ is:

$$\langle\psi(t)| = e^{-if(t)} \langle\phi(t)|$$

Simplifying the above equation results in:

$$-\frac{df(t)}{dt} = \frac{1}{\hbar} \langle\psi(t)|H|\psi(t)\rangle - i \langle\phi(t)| \frac{d}{dt} |\phi(t)\rangle$$

We integrate the above equation from 0 to T.

$$-(f(T) - f(0)) = \frac{1}{\hbar} \int_0^T dt \langle\psi(t)|H|\psi(t)\rangle - i \int_0^T dt \langle\phi(t)| \frac{d}{dt} |\phi(t)\rangle$$

Recalling that $\Phi = f(T) - f(0)$, we will obtain:

$$\Phi = -\frac{1}{\hbar} \int_0^T dt \langle\psi(t)|H|\psi(t)\rangle + i \int_0^T dt \langle\phi(t)| \frac{d}{dt} |\phi(t)\rangle$$

Finally, we refer back to $|\psi(T)\rangle$.

$$|\psi(T)\rangle = |\psi(0)\rangle e^{-\frac{i}{\hbar} \int_0^T dt \langle\psi(t)|H|\psi(t)\rangle} e^{i \int_0^T dt i \langle\phi(t)| \frac{d}{dt} |\phi(t)\rangle}$$

The first phase refers to dynamical phase γ_D whereas the second phase refers to the geometrical phase γ_G .

$$\gamma_D = \frac{1}{\hbar} \int_0^T dt \langle\psi(t)|H|\psi(t)\rangle$$

$$\gamma_G = \int_0^T dt i \langle\phi(t)| \frac{d}{dt} |\phi(t)\rangle$$

$$|\psi(T)\rangle = |\psi(0)\rangle e^{-i\gamma_D} e^{i\gamma_G}$$

We would like to express the geometrical phase in terms of the original wave function $|\psi(t)\rangle$. We consider the case when we shift the Hamiltonian operator, we will have an equivalent Hamiltonian as:

$$H'(t) = H - \langle\psi(t)|H|\psi(t)\rangle$$

The Schrödinger equation becomes:

$$H'|\psi_s(t)\rangle = i\hbar \frac{d|\psi_s(t)\rangle}{dt}$$

where $|\psi_s(t)\rangle$ is the new state for the shifted Hamiltonian. The solution of the above Schrödinger equation is:

$$|\psi_s(t)\rangle = |\psi_s(0)\rangle e^{-\frac{i}{\hbar} \int_0^t dt' H'(t')}$$

We insert the expression of $H'(t)$ and choose the initial condition such that $|\psi(0)\rangle = |\psi_s(0)\rangle$.

$$|\psi_s(t)\rangle = |\psi(0)\rangle e^{-\frac{i}{\hbar} H t} e^{\frac{i}{\hbar} \int_0^t dt' \langle\psi(t')|H|\psi(t')\rangle}$$

The solution of the original Schrödinger equation can be expressed as:

$$|\psi(t)\rangle = |\psi(0)\rangle e^{-\frac{i}{\hbar} H t}$$

Substituting it to $|\psi_s(t)\rangle$:

$$|\psi_s(t)\rangle = |\psi(t)\rangle e^{\frac{i}{\hbar} \int_0^t dt' \langle\psi(t')|H|\psi(t')\rangle}$$

Evaluating at $t = T$ and reverting the dummy variable from t' to t , we have:

$$|\psi_s(T)\rangle = |\psi(T)\rangle e^{\frac{i}{\hbar} \int_0^T dt \langle\psi(t)|H|\psi(t)\rangle} = |\psi(T)\rangle e^{i\gamma_D}$$

Substituting the equation for $|\psi(T)\rangle$, we obtain:

$$|\psi_s(T)\rangle = |\psi(0)\rangle e^{i\gamma_G}$$

We take an inner product with the bra $\langle\psi(0)|$ to obtain:

$$\langle\psi(0)|\psi_s(T)\rangle = e^{i\gamma_G}$$

$$\therefore \gamma_G = -i \ln (\langle\psi(0)|\psi_s(T)\rangle)$$

We substitute back $\langle\psi(0)| = \langle\psi_s(0)|$ and $|\psi_s(T)\rangle = |\psi(T)\rangle e^{i\gamma_D}$ and substitute the original Schrödinger equation.

$$\gamma_G = -i \ln (\langle\psi_s(0)|\psi(T)\rangle) + i \int_0^T dt \langle\psi(t)| \frac{d}{dt} |\psi(t)\rangle$$

The γ_G is the geometrical phase and it indeed has a geometrical meaning. There are two geometrical meaning that is important here. First, consider a stationary state that only evolves with time and does not depend on position.

$$|\psi(t)\rangle = |E\rangle e^{-\frac{i}{\hbar}Et}$$

If we substitute it to the equation for γ_G and recalling that we have set $|\psi_s(0)\rangle = |\psi(0)\rangle$, we will obtain:

$$\gamma_G = -i \ln \left(e^{\frac{i}{\hbar}E_0} \langle E|E\rangle e^{-\frac{i}{\hbar}ET} \right) + i \int_0^T dt e^{\frac{i}{\hbar}Et} \langle E|E\rangle \frac{de^{-\frac{i}{\hbar}Et}}{dt} = 0$$

We see that the geometric phase did not change for evolutionary state as there is no path traced and consequently no closed path traced. Instead, the state will just gain a dynamical phase.

Second, assume that the state is shifted by a phase:

$$|\psi'(t)\rangle = |\psi(t)\rangle e^{ik(t)}$$

Substituting it to the above geometrical phase equation, we will obtain:

$$\begin{aligned} \gamma'_G &= -i \ln(\langle \psi_s'(0) | \psi'(T) \rangle) + i \int_0^T dt \langle \psi'(t) | \frac{d}{dt} | \psi'(t) \rangle \\ \gamma'_G &= -i \ln(e^{-ik(0)} \langle \psi(0) | \psi(T) \rangle e^{ik(T)}) + i \int_0^T dt e^{-ik(t)} \langle \psi(t) | \frac{d}{dt} | \psi(t) e^{ik(t)} \rangle \\ \gamma'_G &= -i \ln(\langle \psi(0) | \psi(T) \rangle) + k(T) - k(0) + i \int_0^T dt \langle \psi(t) | \frac{d}{dt} | \psi(t) \rangle - \int_0^T dt \frac{dk(t)}{dt} \\ \gamma'_G &= -i \ln(\langle \psi(0) | \psi(T) \rangle) + i \int_0^T dt \langle \psi(t) | \frac{d}{dt} | \psi(t) \rangle + k(T) - k(0) - (k(T) - k(0)) \\ \gamma'_G &= \gamma_G \end{aligned}$$

It has been proven that the geometric phase is indeed gauge invariance. This is expected as the geometrical phase contains an information about the evolution of the state. It should stay the same when we change our reference phase.

Note that the expression of Berry phase in topological photonic system is similar to the general Berry phase derived earlier, where the derivation and integration is done with respect to \vec{k} instead of t . We have set the first term in the expression of γ_G to be zero as well.

Appendix C: Final Optimized Sizing

Table 1 Final Optimized Sizing of PC Design

Design	Dimension	Value(μm)	Details
PC unit cell	R	72	Radius of air hole
	a	240	Periodicity constant
	h	200	Thickness
PC waveguide	W	3,800	Substrate width
	L	40,000	Substrate length
	w	271	Defect width
Tapered feed	W	272	Tapered feed width
	L	3600	Tapered feed length
	H	200	Tapered feed thickness
Hollow rectangular waveguide	W	440	Rectangular waveguide width
	L	4,000	Rectangular waveguide length
	H	870	Rectangular waveguide thickness
PC DRA	d _r	672	DRA inner radius
	d _a	1,016	DRA outer radius
	d _m	100	Matching air hole radius
	S _r	50	Matching air hole-reference hole distance
	S _m	420	Matching air hole- DRA center distance
PC Filter	W	576	Width of cavity (along line defect)
	H	687	Height of cavity
PC diplexer	n _y	2	Number of air-holes between the directional coupler
	n _x	4	Number of modified air-holes in along the defect axis
	r	55.2	Radius of coupler air-holes

	w	246.6	New defect width
PC bending	θ	$\pm 60^\circ$	Bending angle
	n	2	Number of air-holes in capsule-shaped defect

Table 2 Final Optimized Sizing of TPC Design

Design	Dimension	Value(μm)	Details
TPC Unit Cell	a	242.5	Periodicity constant
	d_1	157.6	Side length of bottom triangle
	d_2	84.9	Side length of top triangle
	h	190	Thickness
TPC Waveguide	W	500	Substrate width
	L		
RTD for TPC	X_{bs}	700	Bottom substrate length
	X_{ts}	605	Top substrate length
	d	92.5	Substrate thickness
	a	233	Substrate width
	X_m	40	MiM length
	Y_m	90	MiM width
	Z_m	2.2	MiM metal thickness
	Z_{ms}	0.6	MiM insulator thickness
	TL ₁	55	RTD chip to exponential strip distance
	TL ₂	0	RTD chip to MiM distance
	l	390	Inner exponential strip length
	ρ	0.9	Ratio between outer and inner exponential strip length
	s	5	Coplanar strip width

	g	8	Gap width
--	---	---	-----------

Table 3 Table of material property

Material	Property	Value	Details
Silicon	ϵ_r (dielectric constant)	11.9	Substrate of PC
InP	ϵ_r	12.9	RTD substrate
SiO ₂	ϵ_r	3.4	RTD MiM insulator